# Three-dimensional nonlinear vortex-induced vibrations of power transmission cables for a bottom-mounted offshore wind turbine

阮, 李



出版情報：Kyushu University, 2024, 博士（工学），課程博士
バージョン：
権利関係：

# Three-dimensional nonlinear vortex-induced vibrations of power transmission cables for a bottom-mounted offshore wind turbine


阮　　李

RUAN Li



Supervised by Prof. Changhong Hu

Interdisciplinary Graduate School of Engineering Sciences,

Kyushu University



May, 2024

# ABSTRACT

The growing need for energy consumption emphasizes the search for secure, environmentally friendly, and sustainable energy sources. Over the past decades, many countries have implemented comprehensive national policies focused on harnessing ocean renewable energies as part of their decarbonization objectives. Given Japan's extensive exclusive economic zone, unlocking its energy potential becomes crucial for ensuring energy security.

The present thesis concentrates on the vortex-induced vibration (VIV) of submarine cables, an essential research topic relating to ocean renewable energy development. Since submarine cables, such as power transmission cables for bottom-mounted offshore wind turbines, are generally used in the ocean environment with tidal currents, it is very important to understand the VIV behavior and internal stresses of those cables for structural and fatigue design of power transmission cables.

In this research, a numerical model based on Euler-Bernoulli beam theory and a single van der Pol wake oscillator model is proposed to study the vortex-induced vibration of a long flexible catenary cable with a low mass ratio in the perpendicular configuration. The wake model uses only one oscillator to describe the in-line and cross-flow vibration with consideration of their nonlinear coupling. An experiment on a flexible cable model in perpendicular flow is carried out to validate the proposed numerical model. Numerical results and experimental measurements are compared on the vortex-induced vibration responses, including the initial static profile and local inclination angle, maximum vibration amplitudes, maximum RMS vibration amplitudes, spatial-temporal varying responses, vibration frequencies, motion trajectories of the cable, time-history and amplitude**s**, average, maximum vibration amplitudes and the frequencies of tensions of the cable.

A sensitivity analysis of the parameters used in the numerical model has been carried out. Numerical simulations by the proposed numerical model with properly selected parameters have demonstrated that the vibration frequency and the axial tension can be well predicted, and the variation of the vibration amplitudes can also be properly captured. The lock-in phenomena and the axial tension variation of the long flexible catenary cable

in perpendicular flow have been carefully studied both numerically and experimentally. In addition, the VIV suppression effectiveness of cable with vibration dampers is studied.

The thesis is organized as follows.

Chapter 2 describes the numerical model. A novel nonlinear single wake oscillator model based on the van der Pol oscillator equation is implemented, which can simulate the coupled lift and drag force and consider the cable catenary profile. In contrast to many other studies that adopt two separate wake oscillators, the proposed model uses a single wake oscillator coupled to both cross-flow and in-line motions. This study focuses on the VIV in the perpendicular flow, which is considered the most important VIV phenomenon for such a kind of cable.

Chapter 3 reports the experiment on a flexible cable. The cable model is suspended in a circulating water tank. Two non-intrusive high-speed underwater cameras are used to record the cable motion during the experiment. The main purpose of the experiment is to validate the numerical model proposed in Chapter 2.

Chapter 4 analyses the sensitivity of the parameters used in the numerical model. To identify the optimal parameter values, an empirical parameters error equation is introduced, which quantifies the deviation between numerical predictions and experimental data. The numerical model is validated using the experimental data in the literature.

Chapter 5 presents a comparison of the numerical and experimental results. Discussions are provided on the initial static profile and local inclination angle, maximum vibration amplitudes, maximum RMS vibration amplitudes, spatial-temporal varying responses, vibration frequencies, motion trajectories of the cable, time-history and amplitudes, average, maximum vibration amplitudes and the frequencies of tensions of the cable.

Chapter 6 describes the VIV suppression effectiveness of the vibration dampers. To investigate the VIV suppression of such flexible cable, an experiment is also carried out on a cable with vibration dampers. Due to the vibration dampers, the maximum vibration amplitudes can be reduced by up to 75%, 60%, and 87% in the X, Y, and Z directions, respectively. The maximum RMS vibration amplitudes can be reduced by up to 64.4%, 46.4%, and 68% in the X, Y, and Z directions, respectively. The average tension of the cable with vibration dampers can be reduced by up to 34%, and the tension maximum vibration amplitude can be reduced by up to 61.5%.

Chapter 7 summarizes the present research and draws the main conclusions. A single wake oscillator model has been successfully applied to the numerical simulation of long flexible cable dynamics in perpendicular flow. The proposed numerical model has been validated by a newly conducted experiment. The vibration dampers proposed in this study can effectively reduce the response of displacement and tension of the cable. Prospects for future research are also given at the end of this chapter.

# Table of contents

# Figure and Table

## CHAPTER 1 Introduction



## CHAPTER 2 Mathematical model for dynamic response of cable



## CHAPTER 3 Tank experiment for cable model

**CHAPTER 5 Study and discussion for numerical and experimental results**

# CHAPTER 1 Introduction

## 1.1 Research background

While oil and gas remain predominant energy sources globally, there has been a continuous surge in the development of renewable energy. In 2023, approximately 473 gigawatts (GW) of renewable energy electricity generation capacity, representing a growth rate of 13.9% compared to 2022, were added worldwide, constituting 86% of new energy capacity, as reported by the International Renewable Energy Agency (IRENA) as shown in Fig 1-1 [1]. Renewable energy harnessed from the ocean represents a substantial portion of this trend [2-8]. Among the renewable energy, offshore wind power, characterized by advantages such as minimal land use and noise, has witnessed rapid growth in recent years. The offshore wind capacity shows a rapid increase in the last 10 years as reported by the World Forum Offshore Wind (WFO) as shown in Fig 1-2 [9]. IRENA projects a nearly 500 GW capacity by 2030 and an impressive 2465 GW by 2050, as depicted in Fig 1-3 [10]. Concurrently, advancements in turbine size, capacity factors, and the optimization of wind farm installation and operation have contributed to a 67% decrease in the worldwide weighted-average levelised cost of electricity (LCOE) for offshore wind from 2010 to 2021. Forecasts by the European Technology & Innovation Platform on Wind Energy (ETIPWind) suggest a further substantial decrease in LCOE over the next 30 years, as illustrated in Fig 1-4 [11].

The growing need for energy consumption emphasizes the search for secure, environmentally friendly, and sustainable energy sources. Over the past decades, many countries have implemented comprehensive national policies focused on harnessing ocean renewable energies as part of their decarbonization objectives. For instance, China has outlined a national development roadmap, setting ambitious targets for the total installed offshore wind energy capacity to reach 65 GW by 2030 and an impressive 200 GW by 2050 [12, 13]. Similarly, the European Union has embarked on a comprehensive Green Deal plan designed to achieve carbon neutrality by 2050. As part of this initiative, the EU aims to achieve a minimum offshore wind energy capacity of 111 GW by 2030 and an even more substantial 317 GW by 2050 [14, 15]. The United States federal government also has committed to a goal of achieving 30 GW of offshore wind power capacity by 2030 [16]. Recognizing the advancements in offshore wind power technology, the World Bank Group (WBG) has instituted an offshore wind development program, dedicated to expediting the deployment of offshore wind projects in emerging markets [17].

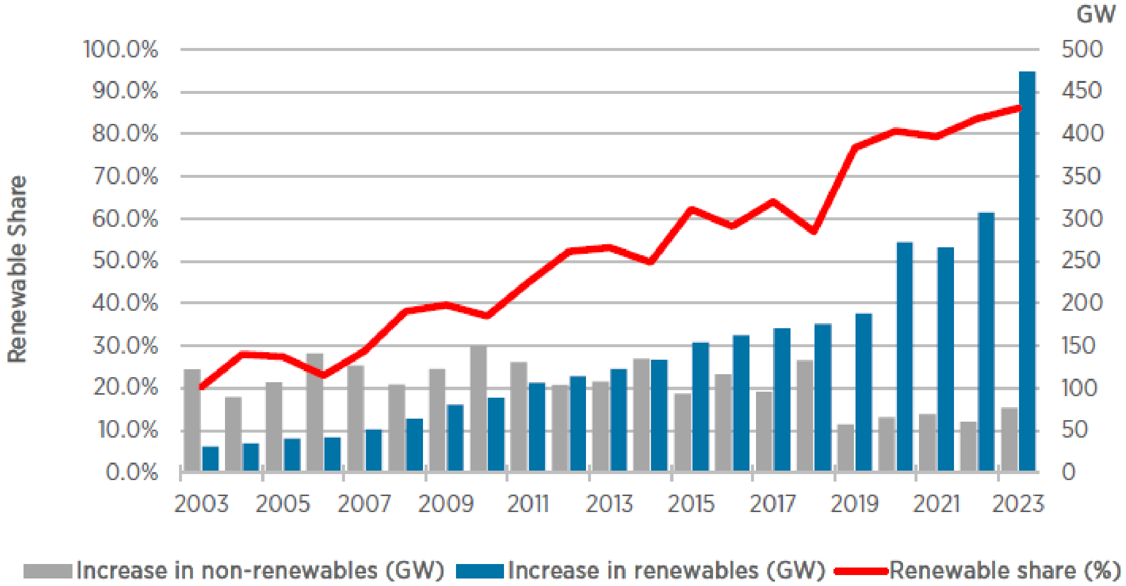


Fig.1-1 Renewable share of annual power capacity expansion [1].

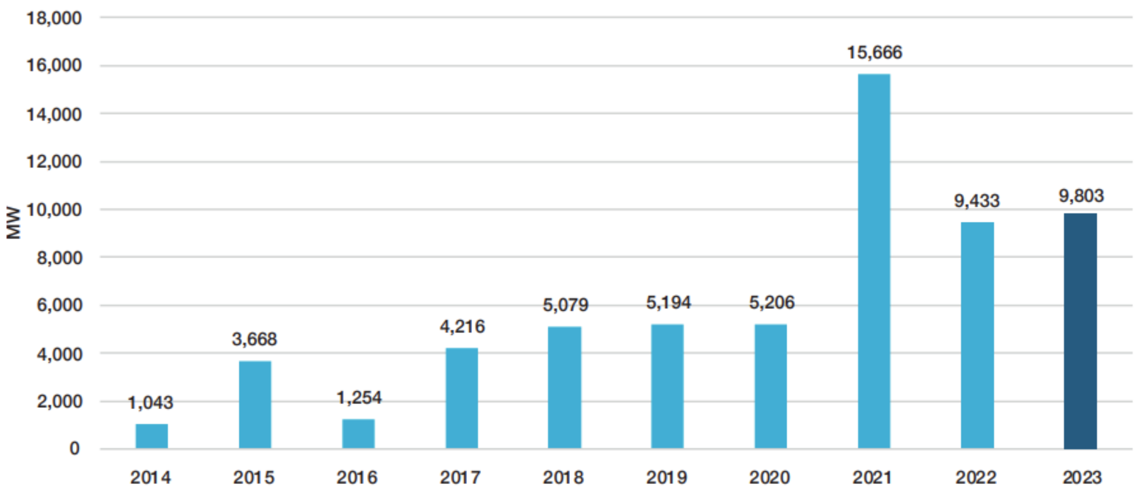


Fig.1-2 Annually added offshore wind capacity [9].

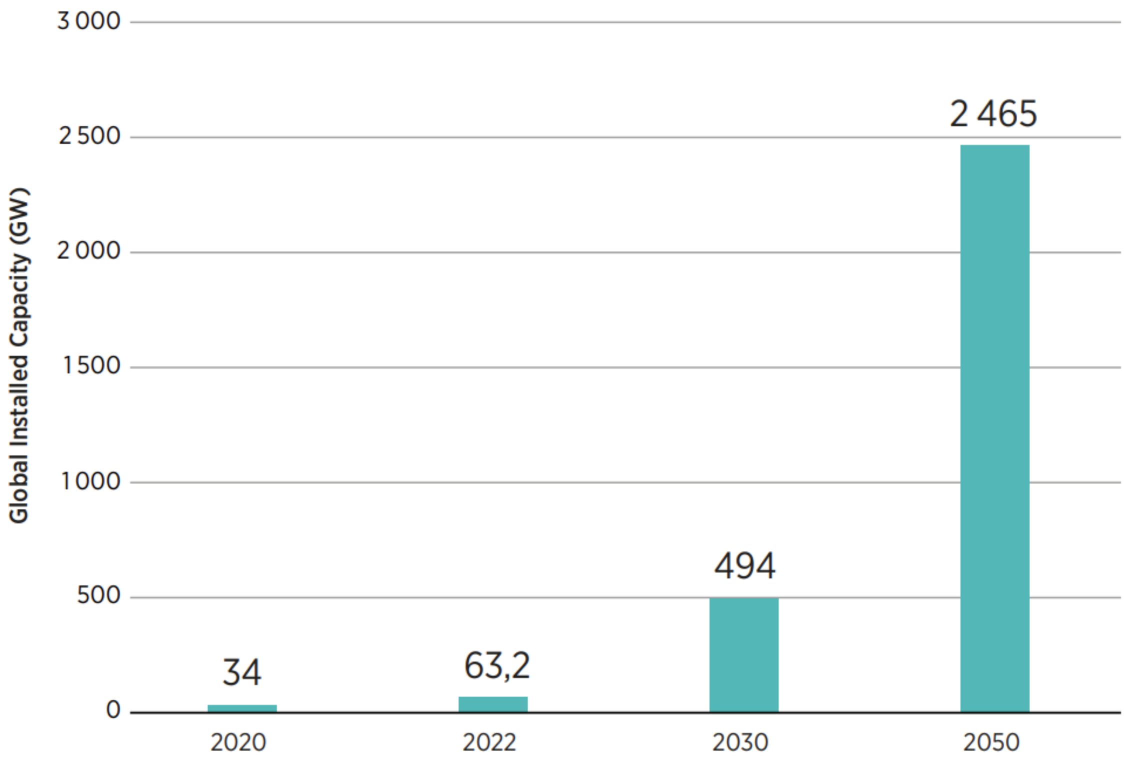


Fig.1-3 Projections of worldwide installed capacity of offshore wind power [10].

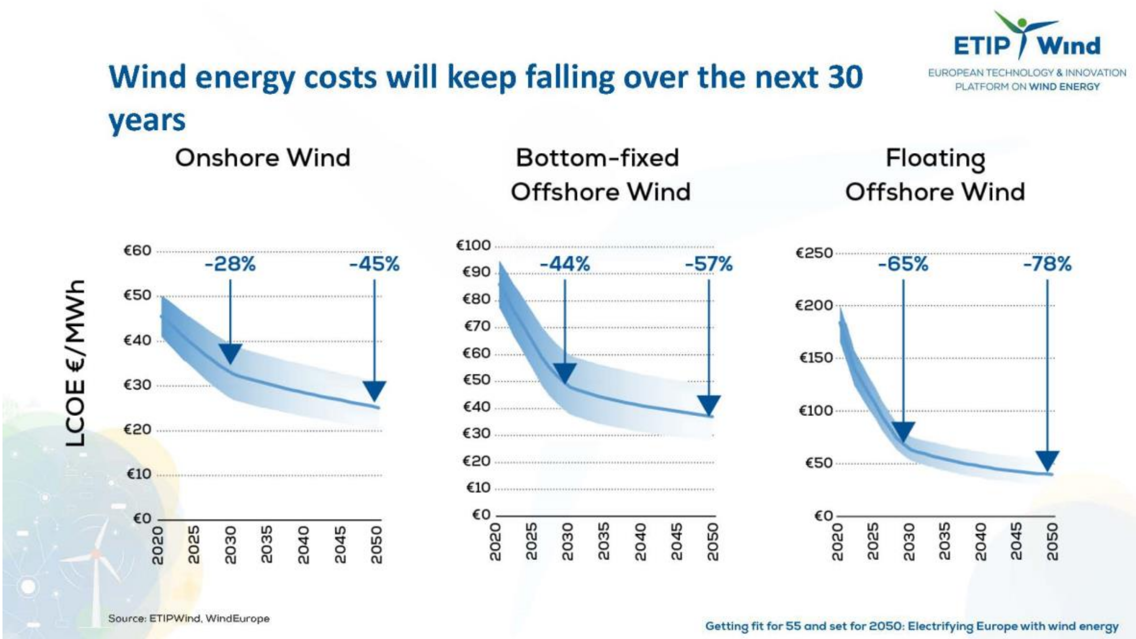


Fig.1-4 Projections of wind power generation costs from 2020 to 2050 [11].

Japan boasts a vast Exclusive Economic Zone (EEZ) spanning over 4,400,000 $km^2$, as depicted in Fig 1-5, harboring the potential for a remarkable 1000 GW in offshore wind power. Despite this potential, progress in offshore power development has been relatively slow. Given Japan's extensive EEZ, unlocking its energy potential becomes crucial for ensuring energy security. In response, the Japanese government has implemented policies aimed at expediting the development of offshore wind power [18-20]. Considering Japan's unique natural conditions, including typhoons, earthquakes, thunderstorms, and complex geological features, the New Energy and Industrial Technology Development Organization (NEDO) formulated an offshore wind development program in 2021 [21]. The envisioned target for Japan's future offshore wind energy capacity is illustrated in Fig 1-6.

As shown in Fig 1-7, a typical support structure option for offshore wind turbines. The bottom-mounted foundations such as monopiles, tripods, and lattice towers are employed in water depths of up to 50m. Floating foundations are employed when the water depth exceeds 50m.

The submarine cable plays a pivotal role in transmitting electric energy in the offshore wind turbines [24, 25]. Notably, submarine cable failures have been responsible for up to 80% of total financial losses and insurance claims over the past decade [26-28]. Surprisingly, the submarine cable cost constitutes less than 10% of the total capital costs of a wind farm [29, 30]. Considering the substantial investment in an offshore wind farm, even a modest improvement in submarine cable reliability could lead to substantial cost savings.


Fig.1-5 Economic zone (EEZ) of Japan.

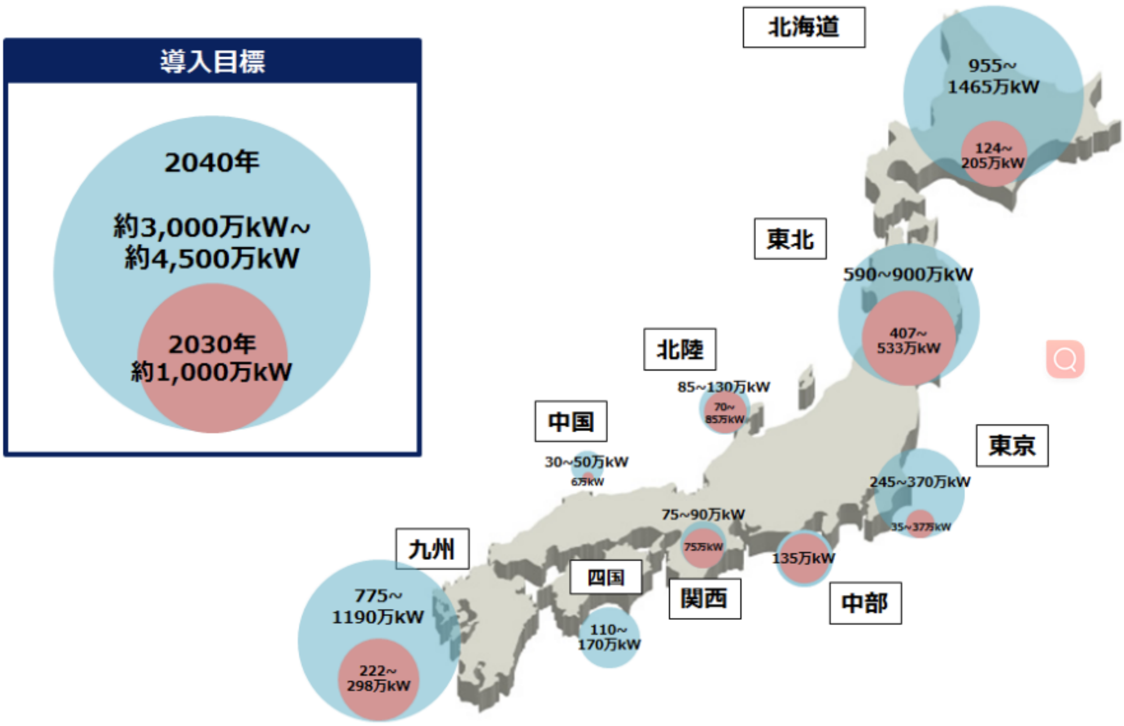


Fig.1-6 Offshore wind energy capacity of Japan [22].

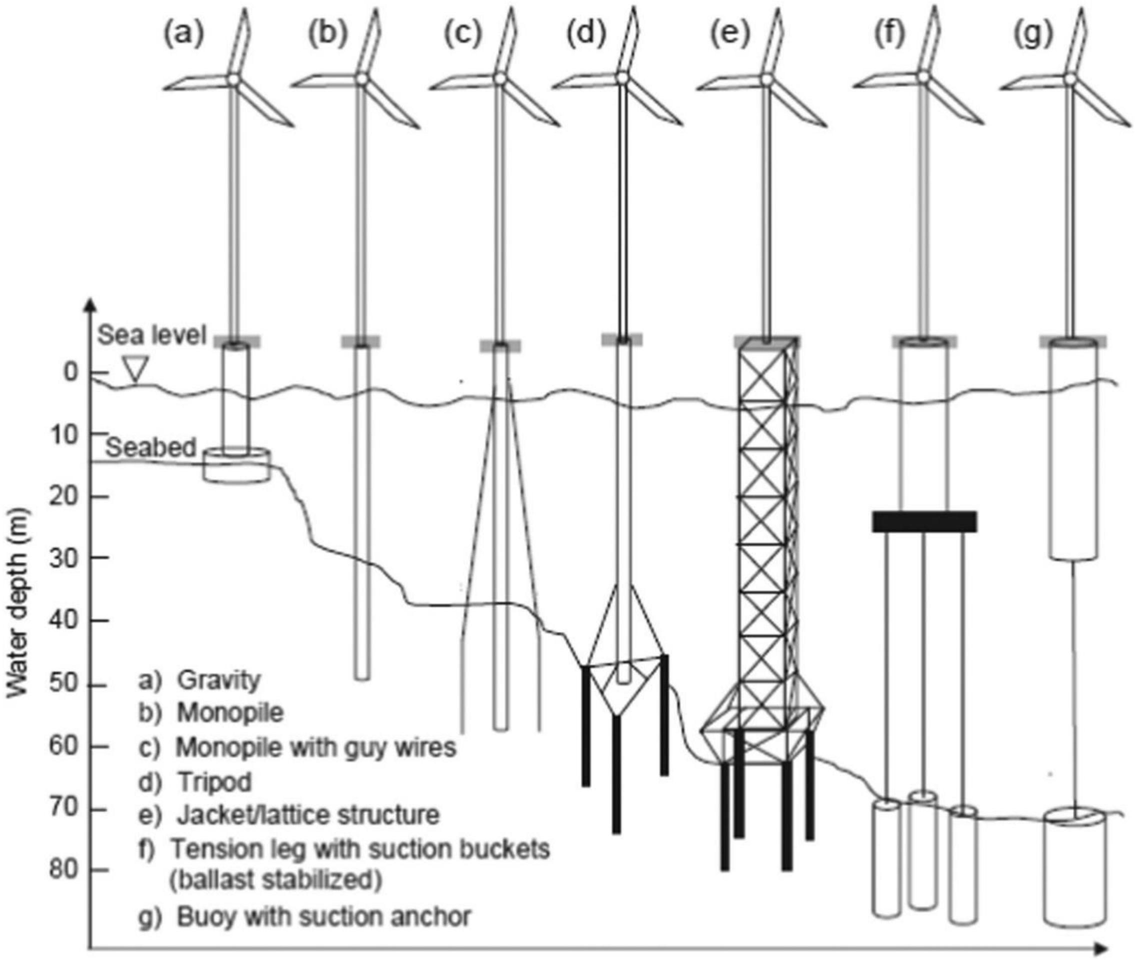


Fig.1-7 Typical support structure options applicable at different water depths [23].

Submarine cables, subjected to ocean currents, may undergo vortex-induced vibrations (VIV) due to their slender subsea structure, potentially leading to reduced structural fatigue life and increased risk of failure over time [31]. It is very important to understand the VIV behavior and internal stresses of those cables for structural and fatigue design of power transmission cables. For the floating foundation, the submarine cable is attached to a floating platform at its top end and to the seabed at its bottom. The motion of the floating platform complicates the VIV of the submarine cable. For the bottom-mounted foundation, the submarine cable is attached to a fixed pile at its top end and to the seabed at its bottom, as illustrated in Fig 1-8. In this thesis, the three-dimensional nonlinear vortex-induced vibrations of power transmission cables for a bottom-mounted offshore wind turbine is studied and analyzed.

On the other hand, developing effective VIV suppression techniques for submarine cables is crucial to mitigate structural fatigue. Fig 1-9 depicts a commercially available cable protection system where cables are wrapped, significantly enhancing both strain and stiffness and thereby extending fatigue life. Considering factors such as cost and installation time, exploring alternative VIV suppression techniques for submarine cables becomes a meaningful avenue of research.

Fig.1-8 Submarine cable of the offshore wind farm [32].

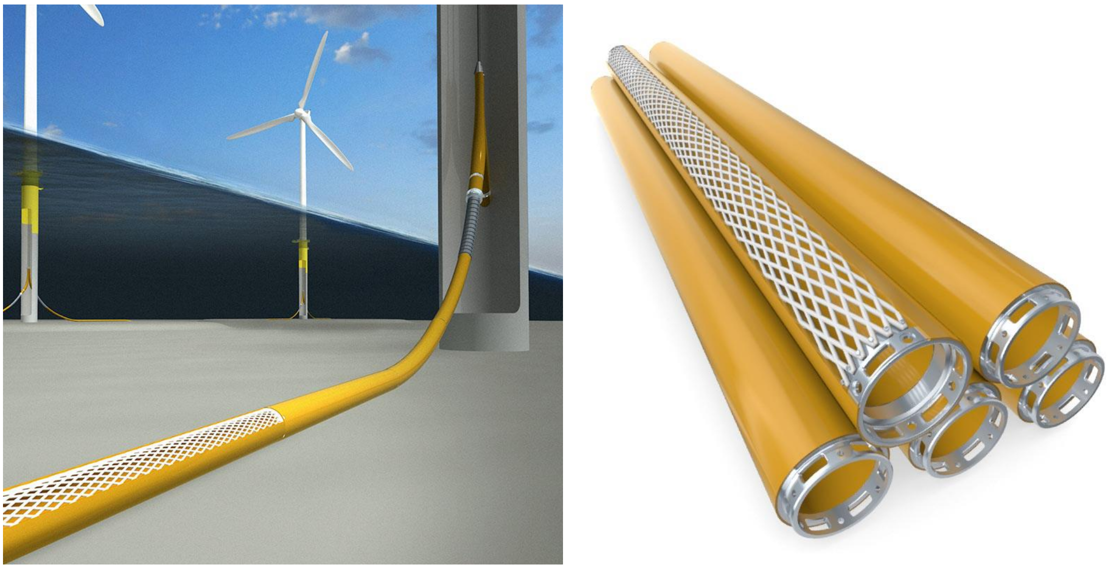

Fig.1-9 Cable protection system [32].

## 1.2 Research status

### 1.2.1 VIV of the cable

Vortex-induced vibration (VIV) is a common fluid-structure coupling phenomenon observed in slender subsea structures such as marine risers, power cables, free-spanning pipelines, and mooring lines. This phenomenon is pertinent to various offshore and ocean engineering applications, encompassing hydrocarbon transportation, renewable energy, and subsea infrastructure. When a slender subsea structure is subjected to the current, the vortex shedding around the slender subsea structure may be induced, which in turn affects the flow field around the structure and leads to oscillatory hydrodynamic forces. When the vortex shedding frequency becomes close to a natural fundamental frequency of the structure, the phenomenon of lock-in occurs [33]. The resulting oscillatory hydrodynamic forces can diminish structural fatigue life or even lead to collapse [34, 35]. Consequently, extensive studies have been conducted in the literature to comprehend the VIV phenomenon in slender subsea structures [36, 37].

Recently, there has been significant attention directed towards the VIV of submarine cables used for the power transmission of offshore wind energy. Unlike vertical risers and free-spanning pipelines, submarine cables positioned between the seabed and foundation resemble a catenary riser, primarily influenced by their wetted weight. The deployment of a catenary introduces geometric nonlinearity, resulting in intricate dynamics in the flow field. Numerous experiments and numerical studies have been conducted and documented in the literature to investigate the dynamic response characteristics of such structures. It is noteworthy that configurations are categorized based on the relative position of the incoming flow and the catenary profile. The convex configuration is designated when the extrados of the catenary-shaped slender subsea structure faces the incoming flow, the concave configuration occurs when the intrados faces the incoming flow, and the perpendicular configuration is present when the curvature plane is perpendicular to the incoming flow. These three configurations are illustrated in Fig 1-10.

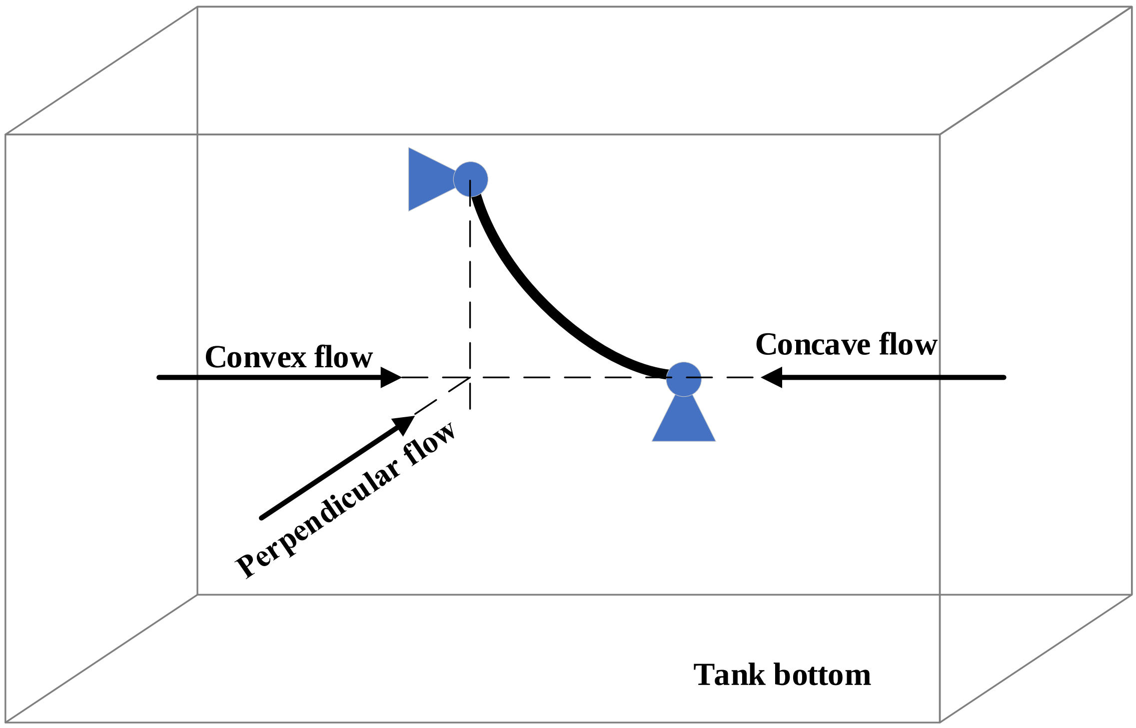


Fig.1-10 Three configurations in parallel (concave/convex) and perpendicular incoming flow orientations.

For the rigid curved structure, Assi et al. and Seyed-Aghazadeh et al. reported that vibration amplitudes of catenary riser in both the convex and concave configurations are smaller than straight riser (with the same mass ratio) at the lock-in range [38, 39]. Seyed-Aghazadeh et al. also reported that the vortex shedding is parallel to the curved cylinder by flow visualization in both configurations. Additionally, higher harmonic components, with frequencies twice and three times the vibration frequency, are observed due to the asymmetric wake vortex and the relative velocity of the vibration structure with respect to the incoming flow [39]. Srinil et al. have studied the in-plane/out-of-plane VIV of a rigid curved cylinder and found that cross-flow and in-line VIV amplitudes in perpendicular configuration are larger than those of convex and concave configuration, with the amplified mean displacements and hydrodynamic forces as well as the appearance of a multiple 2:1:1 resonance [40].

For the flexible curved structure, Chaplin and King studied the frequencies of cross-flow vibrations of a catenary model riser for both the convex and concave configurations, and discovered that response spectra have a higher bandwidth than those of risers perpendicular to the incoming flow [41]. Seyed-Aghazadeh et al. and Morooka and Tsukada investigated and discussed the switching and competition of the vortex shedding mode along the curved span via experiment [42, 43]. Zhu et al., investigated and discussed the multi-frequency response and phase jump of the flexible curved riser for both the convex and concave configurations, and further experimentally found the mode transition was not synchronized with the incoming flow in both the in-plane and out-of-plane directions [44-48]. Moe et al. studied the time domain variability of motion response under different incoming flow directions, and found that the cable dynamic responses are affected by the incoming flow direction [49].

Besides the experimental investigations, the number of researches using the computational fluid dynamics (CFD) method has been increasing recently [50, 51]. Dalheim studied the VIV of a steel catenary riser using SHEAR7 and found that higher flow velocities induce more significant multi-modal riser responses with larger amplitudes compared to lower flow velocities, with comparisons to experimental data from Halse et al. [52, 53]. Huang et al. utilized a CFD approach to simulate VIV in a catenary riser subjected to concave flow and observed that the in-line vibration in a catenary riser is greater than that in a top-tensioned riser [54].

Since CFD simulations require significantly large computational resources, it is difficult to apply CFD to practical VIV analysis which requires simulation of numerous cases. Therefore, several semi-empirical methods using partial differential equations to describe the wake oscillation phenomenon have been proposed due to their high computational efficiency. Facchinetti et al. proposed an improved wake oscillator model to calculate cross-flow vibration for a rigid circular cylinder [55]. This wake oscillator model was further modified by introducing a second wake oscillator equation to describe the fluctuating drag force and the fluctuating lift force respectively to calculate in-line vibration and cross-flow vibration for both rigid and flexible structures [56-63]. However, in most cases the two wake oscillators are uncoupled. The oscillator describing the lift force is only dependent on the cross-flow motion of the cylinder, while another oscillator describing the drag force is only dependent on the in-line motion of the cylinder. This goes against the physical principles of the VIV phenomenon because the fluid is a continuous medium flowing in both the in-line and cross-flow directions. Therefore, a more reasonable approach to modeling flow dynamics is to use a single equation for the wake oscillator [64, 65]. Qu and Metrikine proposed a single van der Pol wake oscillator that can take account of the coupling effects between the in-line and cross-flow vibration to predict the VIV of the cylinder [66].

Most of the above-mentioned VIV studies are carried out on a rigid cylinder, while investigations of catenary flexible cables are very few. In prior study, a numerical model similar to that employed in this study has been proposed to study the VIV of an overhead transmission cable, in which the cable is treated as a linear structure [67]. In this study, the VIV phenomenon of a high aspect ratio flexible cable, of which the nonlinear feature is important, is studied. Prediction of axial tension of the cable is an important target of this research, which has not been well studied so far both experimentally and numerically. A numerical model is proposed in this paper to predict the dynamic response of a flexible submarine cable in which the single van der Pol wake oscillator model is applied. To validate the proposed numerical method an experiment on a cable model is also carried out. The maximum amplitudes and the vibration frequencies of the cable are investigated. The axial tension and the associated vibration frequencies are carefully studied.

### 1.2.2 VIV suppression of the cable

The VIV suppression of slender offshore structures primarily involves active and passive methods. Passive suppression techniques, such as helical strakes, buoyancy modules, and splitter plates, do not require additional power and are widely utilized in engineering applications due to their ease of manufacturing and implementation [68-74]. These suppression devices achieve the goal of reducing VIV by interfering with vortex shedding [75-79]. Ma et al. found that the axial excitation could reduce the VIV suppression efficiency of helical strakes for a flexible horizontal cylinder via experiment [80]. Guo et al. experimentally studied the VIV suppression effectiveness of buoyancy for a flexible inclined cylinder and found that the cases with the sleeve coverage of 30% and 50% have higher suppression efficiency than that with 80% coverage [74]. Xu et al. investigated and discussed the optimal deployment of helical strakes for a flexible inclined cylinder through a series of experiments, in which the VIV suppression effectiveness of the helical strakes gradually decrease as the yaw angle increases [81, 82].

Research on VIV suppression in offshore structures with passive suppression techniques typically employs experimental observation, semi-empirical models, and computational fluid dynamics (CFD) simulations [83-85]. At present, research on passive suppression devices for a flexible submarine cable is limited, and further investigation is needed to understand their efficiency and mechanisms. However, the semi-empirical model is no longer suitable for studying the curve cable with suppression devices since the empirical parameters utilized in this model are derived from the forced vibration test of a smooth cylinder [86]. On the other hand, the VIV prediction softwares (such as VIVANA, SHEAR7 and VIVA) are not explicitly designed to consider the interaction between the bare cylinder structures and the suppression devices. As a result, noticeable discrepancies exist between the simulation and experimental results [87, 88]. Hence, the model testing remains the most essential and effective method to examine the suppression efficiency and mechanism of the suppression device on the slender offshore structures.

Therefore, conducting experimental investigations to study the effects of suppression devices on cables is essential.

The stock-bridge damper, consisting of two rigid mass blocks, a messenger wire, and a clamp, has been developed and extensively utilized for controlling VIV on transmission lines and some cables on suspension bridges in the air [89, 90]. The primary role of the dampers is to absorb vibrational energy and prevent oscillations [91-96]. In recent years, the stock-bridge damper has been developed and widely utilized to mitigate wind-induced vibration (WIV) on transmission lines and certain cables on suspension bridges. To my knowledge, research on VIV suppression in a flexible submarine cable with stock-bridge dampers hasn't been studied. In this study, the VIV suppression effect of a high aspect ratio flexible cable with stock-bridge dampers is experimentally studied. The variation of axial tension of the cable is an important target of this research, which has not been extensively studied experimentally thus far. To study the VIV suppression effect of stock-bridge dampers, an experiment on a cable model is carried out. The maximum amplitudes and the vibration frequencies of the cable are investigated. The axial tension and the associated vibration frequencies are carefully studied.

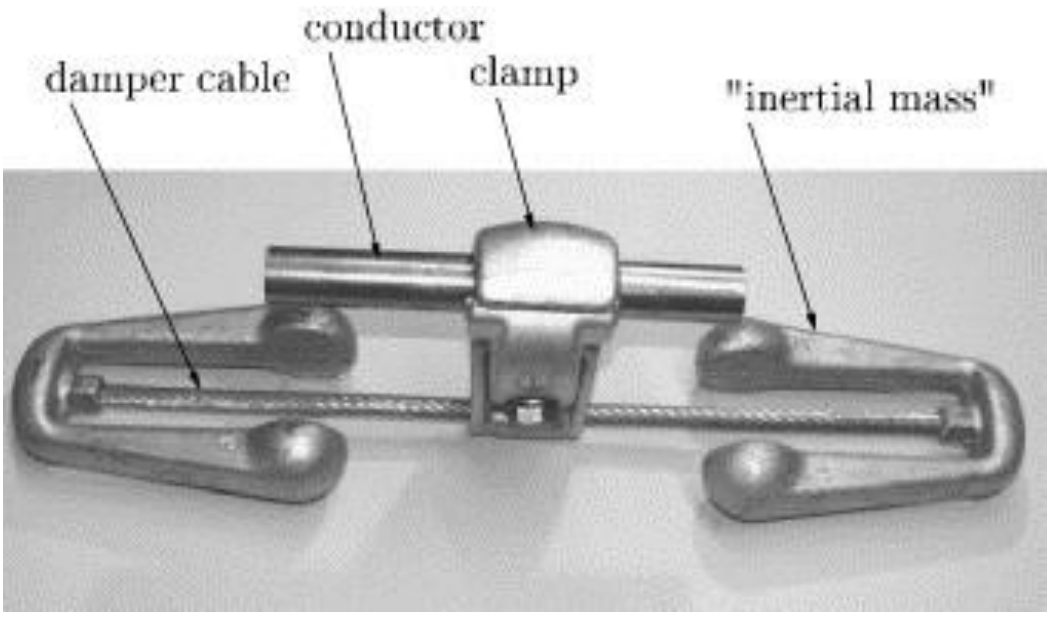


Fig.1-11 Stockbridge damper [94].

## 1.3 Research contents

As stated in section 1.2, the experiments on flexible curved cables are somewhat limited, especially in the case of the perpendicular configuration, it is possible that has greater difficulties. Compared with concave and convex configuration, the greater dynamic responses of flexible curved cables are found in the perpendicular configuration. In addition, the tensions in the structure with high aspect ratio is important in studying VIV phenomena, the axially varying tension and the associated vibration frequencies should be studied [97-99].

In this thesis, a numerical model based on Euler-Bernoulli beam theory and a single van der Pol wake oscillator model is proposed to study the vortex-induced vibration of a long flexible catenary cable with a low mass ratio. The wake model uses only one oscillator to describe the in-line and cross-flow vibration with consideration of their nonlinear coupling. An experiment on a flexible cable model in perpendicular flow is carried out to validate the proposed numerical model. Numerical results and experimental measurements are compared on the vortex-induced vibration responses including the maximum amplitude, axial tension, and vibration frequency. A sensitivity analysis of the parameters used in the numerical model has been carried out. The lock-in phenomena and the axial tension variation of the long flexible catenary cable in perpendicular flow have been carefully studied both numerically and experimentally. In addition, the VIV suppression effectiveness of cable with vibration dampers is studied.

Chapter 2 describes a numerical model based on Euler-Bernoulli beam theory and a single van der Pol wake oscillator model is proposed to study the vortex-induced vibration of a long flexible catenary cable with a low mass ratio. The wake model uses only one oscillator to describe the in-line and cross-flow vibration with consideration of their nonlinear coupling.

In Chapter 3, an experiment on a flexible cable model in perpendicular flow is carried out to validate the proposed numerical model.

In Chapter 4 the appropriate time step and spatial discretization segment are determined and a sensitivity analysis of the empirical parameters is conducted to assess their impact on the model's performance. To identify the optimal parameter values, an empirical parameters error equation is introduced, which quantifies the deviation between numerical predictions and experimental data. Finally, the numerical model is validated using the experimental data in the literature.

In Chapter 5, the numerical results and experimental measurements are compared in perpendicular flow, including the initial static profile and local inclination angle, the maximum vibration amplitudes, the maximum RMS vibration amplitudes, the spatial-temporal varying responses, the vibration frequencies and the motion trajectories of the cable, the time-history and amplitudes, the average, the maximum vibration amplitudes and the frequencies of tensions of the cable.

Chapter 6 describes the VIV suppression effectiveness of the vibration dampers. To investigate the VIV suppression of such flexible cable, an experiment is carried out on a cable with vibration dampers. The vortex-induced vibration responses are compared in both experimental results, including the maximum vibration amplitudes, the maximum RMS vibration amplitudes, the time-averaged in-line displacements, the vibration frequencies; the time-history and amplitudes, the average, the maximum vibration amplitudes and the frequencies of tensions.

Chapter 7 summarizes the present research and draws the main conclusions. Prospects for future research are also given at the end of this chapter.

# CHAPTER 2 Mathematical model for dynamic response of cable

## 2.1 Introduction

This study introduces a novel nonlinear wake oscillator model to better account for the impact of the spanwise inclination of the curved cable relative to the incoming flow on hydrodynamic force components in cross-flow and in-line directions. In contrast to many other studies that adopt two separate wake oscillators, this model uses a single wake oscillator coupled to both cross-flow and in-line motions. The proposed model is based on the van der Pol oscillator equation, with classic acceleration coupling between the wake and cross-flow vibration. Meanwhile, the in-line vibration is nonlinearly coupled with the wake oscillator. It is worth mentioning that, while in practical scenarios, the flow direction is omnidirectional, this study focuses on the perpendicular flow direction as shown in Fig 1-10.

Section 2.2 and 2.3 describes the numerical model of the curved cable with catenary configuration in which the fluctuating drag force and lift force are coupled. Section 2.4 describes a single wake oscillator equation coupled to both lift force and drag force. The numerical solutions of the above equations are described in section 2.5.

## 2.2 Catenary configuration of the curved cable

A flexible cable with two ends hung at different heights is studied, as shown in Figure 2-1. The Global reference frame is defined at the lower end of the cable with its Z-axis aligned with the flow direction and Y-axis pointing upwards. The X-axis is determined by the right-hand rule. In the initial state, the cable sags in the X-Y plane, and the cable profile is approximated by a classical hyperbolic function. Suppose that the cable is properly aligned so that the axial tension at (0, 0) is in horizontal direction, according to the catenary theory, a point $(x, y)$ on the cable can be expressed by

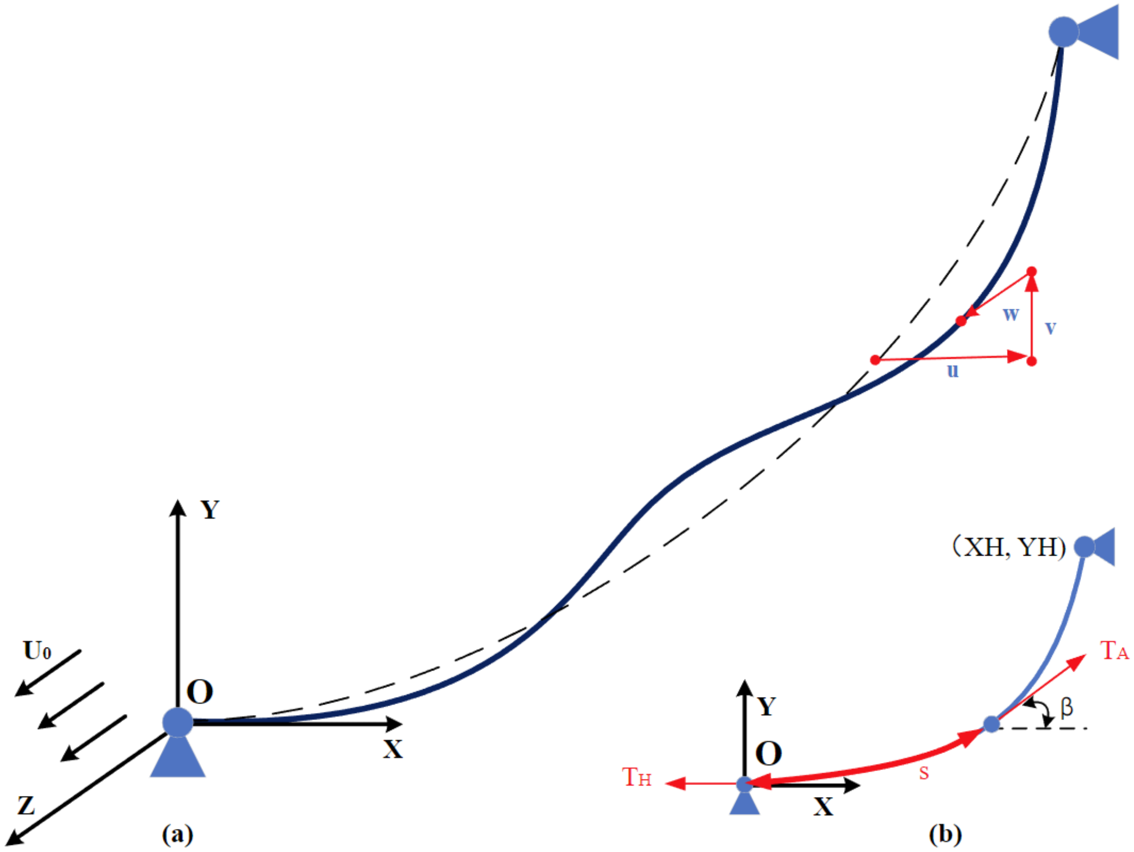


Fig.2-1 (a) Sketch of a catenary cable experiencing VIV in perpendicular flow; (b) the catenary-shaped profile at the initial static state of cable.

$$y = a \cosh\left(\frac{x}{a}\right) - a\,, \tag{1}$$

where $a = T_H/W_e$, $T_H$ is the horizontal tension at the origin and $W_e$ is the effective weight of the cable per unit length in the fluid. The inclination angle $\beta$ at arbitrary position on the cable can be expressed as a function of arc length $s$ $(0 \leq s \leq L,\ L$ is the cable length) by

$$\beta = \tan^{-1}\left(\frac{s}{a}\right), \qquad 0 \leq \beta < \frac{\pi}{2}. \tag{2}$$

Additionally, the initial spatially varying axial tension $T_A$ could be expressed as

$$T_A(s) = \frac{T_H}{\cos\beta} = W_e(a^2 + s^2)^{\frac{1}{2}}. \tag{3}$$

By segmental discretization for the curved cable, the arc length $ds$ could be obtained with a geometric constraint $ds \approx \sqrt{dx^2 + dy^2}$, then the coordinates of the point $(x, y)$ can also be expressed as a function of arc length $s$ by

$$x(s) = \mathrm{a}\sinh^{-1}\left(\frac{s}{a}\right), \tag{4}$$

$$y(s) = (a^2 + s^2)^{\frac{1}{2}} - a, \tag{5}$$

## 2.3 Cable motion equations and hydrodynamic forces

In this study, the cable is assumed to be the Euler–Bernoulli beam, and the materials are assumed to be spatially uniform [100-111]. The cable properties, such as the Young's modulus (*E*), outer diameter (*D*), cross-sectional area ($A_r$), second moment of area (*I*), structural mass per unit length (*m*), structural damping coefficient (*c*), axial stiffness ($EA_r$) and bending stiffness (*EI*) are constant along the cable. The cable with pinned–pinned boundary conditions could be described by the following partial differential equations [112-125]:

$$(m + m_a)\frac{\partial^2 u}{\partial t^2} + c\frac{\partial u}{\partial t} + EI\frac{\partial^4 u}{\partial s^4} - T_A\frac{\partial^2 u}{\partial s^2} - EA_r\frac{\partial}{\partial s}\left(\left(\frac{\partial x}{\partial s}\right)^2\frac{\partial u}{\partial s} + \frac{\partial x}{\partial s}\frac{\partial y}{\partial s}\frac{\partial v}{\partial s}\right) = F_x, \tag{6}$$

$$(m + m_a)\frac{\partial^2 v}{\partial t^2} + c\frac{\partial v}{\partial t} + EI\frac{\partial^4 v}{\partial s^4} - T_A\frac{\partial^2 v}{\partial s^2} - EA_r\frac{\partial}{\partial s}\left(\left(\frac{\partial y}{\partial s}\right)^2\frac{\partial v}{\partial s} + \frac{\partial x}{\partial s}\frac{\partial y}{\partial s}\frac{\partial u}{\partial s}\right) = F_y, \tag{7}$$

$$(m + m_a)\frac{\partial^2 w}{\partial t^2} + c\frac{\partial w}{\partial t} + EI\frac{\partial^4 w}{\partial s^4} - T_A\frac{\partial^2 w}{\partial s^2} = F_z, \tag{8}$$

where *u(t, s)*, *v(t, s)* and *w(t, s)* denote respectively the dynamic displacements measured from the initial static catenary configuration in Global coordinate frame; added mass per unit length in still water $m_a = C_a\rho\pi D^2/4$, $C_a = 1$ for the cylinder; viscous damping coefficient $c = 2(m + m_a)\xi\omega_n$, $\omega_n = 2\pi f_n$, $f_n$ is the natural frequency of cable, $\xi$

is the damping ratio of cable in the water; $F_x$, $F_y$ and $F_z$ represent the hydrodynamic force components per unit length in the associated directions; $T_A(s,t)$ represents the spatial-temporal varying axial tension that can be expressed by

$$T_A(t,s) = T_A(s) + \Delta T(t,s). \tag{9}$$

Here, $\Delta T(t,s)$ is the additional tension induced by the cable elongation. Suppose that $ds$ is the initial length of a micro element and $ds'$ is the instantaneous length, $\Delta T(t,s)$ can then be described by

$$\Delta T(t,s) = EA_r \frac{ds' - ds}{L}. \tag{10}$$

The instantaneous length $ds'$ can be written by

$$ds' = \sqrt{1 + \left(\frac{\partial u(t,s)}{\partial s}\right)^2 + \left(\frac{\partial v(t,s)}{\partial s}\right)^2 + \left(\frac{\partial w(t,s)}{\partial s}\right)^2}\, ds. \tag{11}$$

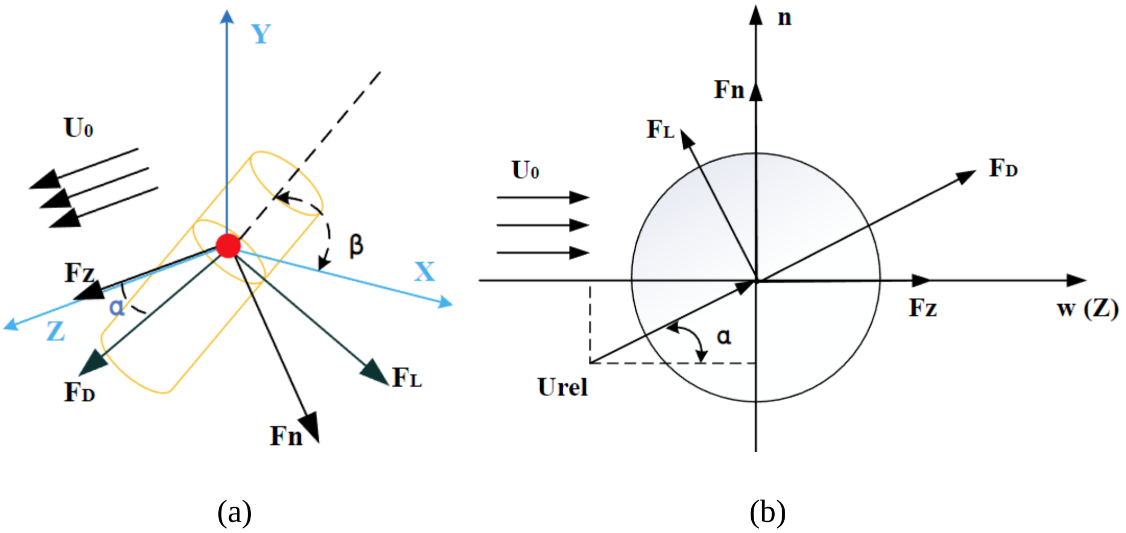


Fig.2-2 (a) Schematic view of hydrodynamic force components (b) drag force and lift force at cross-flow and in-line directions.

In Equations (6) and (7), the forces $F_x$ and $F_y$ could be expressed as functions of the inclination angle $\beta$ and the cross-flow hydrodynamic load $F_n$:

$$F_x = F_n \sin\beta\,, \qquad F_y = -F_n \cos\beta\,. \tag{12}$$

The schematic view is depicted in Fig 2-2. In the figure, $U_{rel}$ is the relative flow velocity, $F_L$ and $F_D$ are the lift and drag force, respectively. For an oscillating cable element, $F_L$ and $F_D$ are dependent upon $U_{rel}$. Since the flow separation point changes along the circumferential direction of the element, an oscillating force $F_{osc}$ needs to be considered in the in-line direction according to the study in [126-130]. Therefore, the cross-flow force $F_n$ and in-line force $F_z$ could be expressed as

$$F_n = F_D \sin\alpha + F_L \cos\alpha\,, \tag{13}$$

$$F_z = F_D \cos\alpha - F_L \sin\alpha + F_{osc}, \tag{14}$$

where $\alpha$ is the angle between $U_{rel}$ and $U_0$. The drag force and lift force are calculated by [131]

$$F_D = \frac{1}{2}\rho D U_{rel}^2 C_{DM}, \tag{15}$$

$$F_L = \frac{1}{2}\rho D U_{rel}^2 C_L, \tag{16}$$

where $\rho$ represents the fluid density, $C_L$ is the lift coefficients, $C_{DM}$ is the steady component of drag force coefficient. The detailed expressions of $C_{DM}$ and $F_{osc}$ are given later.

In Equations (13-14), the angle $\alpha$ between the relative flow velocity $U_{rel}$ and the incoming flow velocity $U_0$ could be obtained by

$$\sin\alpha = \frac{-\dfrac{\partial n}{\partial t}}{U_{rel}}, \qquad \cos\alpha = \frac{U_0 - \dfrac{\partial w}{\partial t}}{U_{rel}}, \qquad U_{rel} = \sqrt{\left(\frac{\partial n}{\partial t}\right)^2 + \left(U_0 - \frac{\partial w}{\partial t}\right)^2} \tag{17}$$

Here, *n* is the normal dynamic displacement of the cable element projected in X-Y plane as shown in Fig 2-2. (b). The displacements $u$ and $v$ can be written as:

$$u = n \sin \beta , \qquad v = -n \cos \beta , \tag{18}$$

It is worth noting that $\beta$ is assumed to be constant for each element in the model. While $\beta$ can be a time-varying variable and iteratively solved, this method is highly time-consuming and prone to divergence [124, 125]. In the following Fig 2-3, the time history of $\beta$ at the location of maximum vibration amplitude of the cable is shown, for the case of $U_0 = 0.56\, m/s$ in which the largest cable vibration was found. The range of $\beta$ variation is $-11.4° \leq \beta \leq 6.6°$, with the average of $-4.2°$. Therefore, $\beta$ is set as a constant for each element in this study and obtained according to Equation (2).

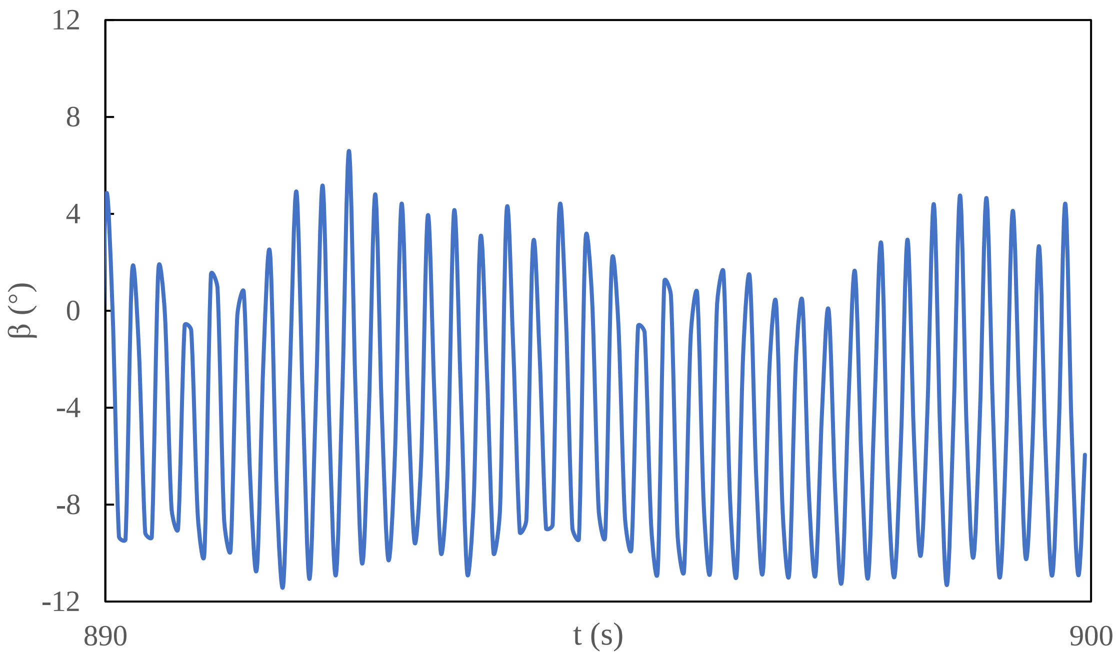


Fig.2-3 Time-variation of $\beta$ measured at maximum vibration point of the cable in the experiment for the case of $U_0 = 0.56\, m/s$.

The drag and lift forces are interdependent in physics since they are both the projection of the total fluid force in an orthogonal frame. Based on this perspective, Qin proposed a method to express the relationship between the instantaneous drag coefficient and the lift coefficient [132]. The instantaneous drag coefficient is quadratically coupled with the lift coefficient:

$$C_D = C_{DM} + \varphi C_L^2, \tag{19}$$

where $\varphi$ is constant, and $C_D$ is the in-line drag force coefficient. Assuming the lift coefficient is described as $C_L = C_{L0}\sin(\omega t)$, where $C_{L0}$ is the amplitude of lift coefficient, $C_D$ could be written as the combination of an offset and an oscillating component:

$$C_D = (C_{DM} + \frac{1}{2}\varphi C_{L0}^2) - \frac{1}{2}\varphi C_{L0}^2\cos(2\omega t) = \overline{C_D} - C_{D0}\cos(2\omega t)\,. \tag{20}$$

The term $\overline{C_D} = C_{DM} + \frac{1}{2}\varphi C_{L0}^2$ is the mean drag coefficient and $C_{D0} = \frac{1}{2}\varphi C_{L0}^2$ is the oscillating amplitude. $C_{L0}$, $C_{D0}$, and $\overline{C_D}$ could be obtained by experiment or CFD method. $C_{DM}$ and $\varphi$ could be calculated by

$$C_{DM} = \overline{C_D} - \frac{1}{2}\varphi C_{L0}^2, \qquad \varphi = 2\frac{C_{D0}}{C_{L0}^2}. \tag{21}$$

The Equation (19) describes the relationship between coupled drag force coefficient and lift force coefficient, and in the same manner as lift force in equation (16), the in-line additional oscillating force $F_{osc}$, which is coupled with the lift force is written as:

$$F_{osc} = \frac{1}{2}\varphi C_L^2\rho D\left(U_0 - \frac{\partial w}{\partial t}\right)\left|U_0 - \frac{\partial w}{\partial t}\right|. \tag{22}$$

By calculation, the cross-flow force $F_n$ and in-line force $F_z$ are obtained as:

$$F_n = \frac{1}{2}C_L\rho D U_{rel}^2\cos\alpha + \frac{1}{2}C_{DM}\rho D U_{rel}^2\sin\alpha\,, \tag{23}$$

$$F_z = -\frac{1}{2}\rho D U_{rel}^2 C_L\sin\alpha + \frac{1}{2}C_{DM}\rho D U_{rel}^2\cos\alpha + \frac{1}{2}\varphi C_L^2\rho D\left(U_0 - \frac{\partial w}{\partial t}\right)\left|U_0 - \frac{\partial w}{\partial t}\right|. \tag{24}$$

It can be found that when the cylinder is fixed ($\alpha = 0°$, $\partial w/\partial t = 0$, and $\partial n/\partial t = 0$), Equation (24) could be reduced to

$$F_z = \frac{1}{2}(C_{DM} + \varphi C_L^2)\rho D U_0^2, \tag{25}$$

which is the same with the one proposed by Qin for the coupled lift force and drag force at a fixed cylinder [132].

## 2.4 Wake oscillators model

In traditional two-wake oscillators model, two uncoupled wake oscillator equations are commonly introduced to describe the fluctuating drag force and the fluctuating lift force, respectively. The oscillator describing the lift force is only dependent on the cross-flow motion, while another oscillator describing the drag force is only dependent on the in-line motion [133].

However, the drag and lift forces are interdependent in physics since they are both the projection of the total fluid force in an orthogonal frame. On the other hand, the VIV normally occurs simultaneously in both cross-flow and in-line directions in a coupled manner. Based on this perspective, it is more reasonable to employ only one oscillator to describe the wake dynamics, with this oscillator appropriately coupled to both cross-flow and in-line vibrations of the cylindrical structure. Meanwhile, it has the following advantages:

- ✧ It simplifies the two-wake oscillators model by reducing the number of parameters and equations.
- ✧ Based on previous research, for a rigid cylinder, the model can reproduce major features of the coupled cross-flow and in-line VIV, especially the lock-in phenomenon at low velocity.
- ✧ The model properly considers the phase relation between lift and drag force variations on a fixed cylinder, which cannot be considered by the uncoupled two-wake oscillator model.

Based on these, the van der Pol wake oscillator model considering the coupling effects between in-line and cross-flow oscillations is applied [66]:

$$\frac{\partial^2 q}{\partial t^2} + \varepsilon\omega_s(q^2 - 1)\frac{\partial q}{\partial t} + \omega_s^2 q - \kappa\frac{\omega_s^4 D\frac{\partial^2 w}{\partial t^2}}{\omega_s^4 D^2 + \left(\frac{\partial^2 w}{\partial t^2}\right)^2} q = \frac{A}{D}\frac{\partial^2 n}{\partial t^2}, \tag{26}$$

where $q(t,s) = 2C_L(t,s)/C_{L0}$ is the wake variable, $A$, $\kappa$ and $\varepsilon$ are the tuning parameters, $\omega_s = 2\pi S_t U_0/D$ is the Strouhal frequency, and $S_t$ is the Strouhal number. In the equation, a parametric excitation term about in-line vibration is contained in the left-hand side while the cross-flow vibration is contained in the right-hand side. According to Equation (18), Equation (26) could be decomposed to express the relation between the in-line vibration *w* and the cross-flow vibration *u* and *v*:

$$\frac{\partial^2 q}{\partial t^2} + \varepsilon\omega_s(q^2 - 1)\frac{\partial q}{\partial t} + \omega_s^2 q - \kappa\frac{\omega_s^4 D\frac{\partial^2 w}{\partial t^2}}{\omega_s^4 D^2 + \left(\frac{\partial^2 w}{\partial t^2}\right)^2} q = \frac{A}{D}\frac{1}{\sin\beta}\frac{\partial^2 u}{\partial t^2}, \tag{27}$$

$$\frac{\partial^2 q}{\partial t^2} + \varepsilon\omega_s(q^2 - 1)\frac{\partial q}{\partial t} + \omega_s^2 q - \kappa\frac{\omega_s^4 D\frac{\partial^2 w}{\partial t^2}}{\omega_s^4 D^2 + \left(\frac{\partial^2 w}{\partial t^2}\right)^2} q = \frac{A}{D}\frac{1}{\cos\beta}\frac{\partial^2 v}{\partial t^2}. \tag{28}$$

To further simplify Equation (27) (28), simultaneously align corresponding parameters, parameters $q_x$ and $q_y$ are introduced, and $q^2 = q_x^2 + q_y^2$. Considering $u = n\sin\beta$ and $v = -n\cos\beta$, making $q_x = q\sin\beta$ and $q_y = -q\cos\beta$. Then, the Equation (27) (28) could be transformed into:

$$\frac{\partial^2 q_x}{\partial t^2} + \varepsilon\omega_s\left(\frac{q_x^2}{\sin^2\beta} - 1\right)\frac{\partial q_x}{\partial t} + \omega_s^2 q_x - \kappa\frac{\omega_s^4 D\frac{\partial^2 w}{\partial t^2}}{\omega_s^4 D^2 + \left(\frac{\partial^2 w}{\partial t^2}\right)^2} q_x = \frac{A}{D}\frac{\partial^2 u}{\partial t^2}, \tag{29}$$

$$\frac{\partial^2 q_y}{\partial t^2} + \varepsilon\omega_s\left(\frac{q_y^2}{\cos^2\beta} - 1\right)\frac{\partial q_y}{\partial t} + \omega_s^2 q_y - \kappa\frac{\omega_s^4 D\frac{\partial^2 w}{\partial t^2}}{\omega_s^4 D^2 + \left(\frac{\partial^2 w}{\partial t^2}\right)^2} q_y = \frac{A}{D}\frac{\partial^2 v}{\partial t^2}. \tag{30}$$

Finally, the above equations are further simplified and transformed, the improved nonlinear single wake oscillator model is proposed:

$$\left\{\begin{array}{l}
\ddot{u}+\frac{2c+\rho D C_{DM}U_{rel}}{2(m+m_a)}\dot{u}+\frac{EI}{m+m_a}u''''-\frac{T_A+EA_r x'^2}{m+m_a}u'' \\
-\frac{EA_r}{m+m_a}(2x'x''u'+(x''y'+x'y'')v'+x'y'v'')=\frac{\rho D U_{rel}q_x C_{L0}(U_0-\dot{w})}{4(m+m_a)}, \\
\\
\ddot{v}+\frac{2c+\rho D C_{DM}U_{rel}}{2(m+m_a)}\dot{v}+\frac{EI}{m+m_a}v''''-\frac{T_A+EA_r y'^2}{m+m_a}v'' \\
-\frac{EA_r}{m+m_a}(2y'y''v'+(x''y'+x'y'')u'+x'y'u'')=\frac{\rho D U_{rel}q_y C_{L0}(U_0-\dot{w})}{4(m+m_a)}, \\
\\
\ddot{w}+\frac{2c+\rho D C_{DM}U_{rel}}{2(m+m_a)}\dot{w}+\frac{EI}{m+m_a}w''''-\frac{T_A}{m+m_a}w'' \\
=\frac{\rho D C_{L0}U_{rel}q_y\left(\dot{v}-\frac{s}{a}\dot{u}\right)}{4(m+m_a)}+\frac{\rho D C_{DM}U_0U_{rel}}{2(m+m_a)}+\frac{\rho D\varphi {C_{L0}}^2}{8(m+m_a)}{q_y}^2\left(1+\frac{s^2}{a^2}\right)(U_0-\dot{w})|U_0-\dot{w}|, \\
\\
\ddot{q_x}+\varepsilon\omega_s\left(\frac{q_x^2}{y'^2}-1\right)\dot{q_x}+\omega_s^2q_x-\kappa\frac{\omega_s^4D\ddot{w}}{\omega_s^4D^2+(\ddot{w})^2}q_x=\frac{A}{D}\ddot{u}, \\
\ddot{q_y}+\varepsilon\omega_s\left(\frac{q_y^2}{x'^2}-1\right)\dot{q_y}+\omega_s^2q_y-\kappa\frac{\omega_s^4D\ddot{w}}{\omega_s^4D^2+(\ddot{w})^2}q_y=\frac{A}{D}\ddot{v}, \\
x'(s)=a(a^2+s^2)^{-\frac{1}{2}},\qquad x''(s)=-as(a^2+s^2)^{-\frac{3}{2}}, \\
y'(s)=s(a^2+s^2)^{-\frac{1}{2}},\qquad y''(s)=(a^2+s^2)^{-\frac{1}{2}}-s^2(a^2+s^2)^{-\frac{3}{2}}, \\
T_A(s)=W_e(a^2+s^2)^{\frac{1}{2}}, \\
U_{rel}=\sqrt{\dot{u}^2+\dot{v}^2+(U_0-\dot{w})^2}.
\end{array}\right. \tag{31}$$

Here a dot denotes differentiation with respect to the time ($t$) while a prime denotes differentiation with respect to the arclength ($s$).

Strictly speaking, the cable cross-section parallel to the flow direction is an oval cross-section rather than a cylinder cross-section, and varies along the curved axis of the cable. In this paper, the incoming flow velocity $U_0$ is assumed to project onto its normal direction by the Independence Principle, and then the associated cable cross-section at each location is circular with respect to the incoming flow velocity $U_0$ [134]. Therefore, all the hydrodynamic coefficients proposed above are associated with the circular cross-section.

## 2.5 Numerical method

### 2.5.1 A central finite difference method

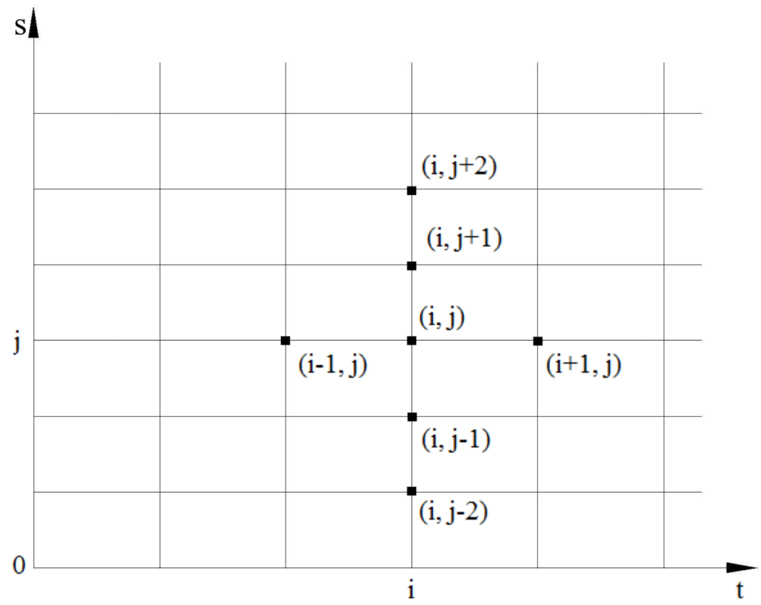


Fig.2-4 Implicit scheme mesh in the central finite difference method.

The Equation (31) have been discretized in the spatial-temporal domains using the central finite difference method of the second order as depicted in Fig 2-4. The whole axial length $s$ can be divided into N segments, and the total calculated time $t$ can be divided into n segments. Thus, the values of the space step (Δs) and the time step (Δt) are set to $\Delta s = s/N$ and $\Delta t = t/n$, respectively. The n+1 discretized time points can be expressed as: $t = t_i$ (i = 1, 2, ..., n+1), and the N+1 discretized space points can be expressed as: $s = s_j$ (j = 1, 2, …, N+1). The parameters $u$, $v$, $w$, $q_x$ and $q_y$ at the time $t_i$ with location $s_j$ are denoted as $u_j^i$, $v_j^i$, $w_j^i$, ${q_x}_j^i$ and ${q_y}_j^i$, respectively. Then the second-order accurate difference scheme for each partial derivative term in the equation is expressed as:

$$
\begin{cases}
\dfrac{\partial u}{\partial t} = \dfrac{u_j^{i+1} - u_j^{i-1}}{2\Delta t}, \qquad \dfrac{\partial^2 u}{\partial t^2} = \dfrac{u_j^{i+1} - 2u_j^{i} + u_j^{i-1}}{(\Delta t)^2}, \\
\dfrac{\partial v}{\partial t} = \dfrac{v_j^{i+1} - v_j^{i-1}}{2\Delta t}, \qquad \dfrac{\partial^2 v}{\partial t^2} = \dfrac{v_j^{i+1} - 2v_j^{i} + v_j^{i-1}}{(\Delta t)^2}, \\
\dfrac{\partial w}{\partial t} = \dfrac{w_j^{i+1} - w_j^{i-1}}{2\Delta t}, \qquad \dfrac{\partial^2 w}{\partial t^2} = \dfrac{w_j^{i+1} - 2w_j^{i} + w_j^{i-1}}{(\Delta t)^2}, \\
\dfrac{\partial q_x}{\partial t} = \dfrac{{q_x}_j^{i+1} - {q_x}_j^{i-1}}{2\Delta t}, \qquad \dfrac{\partial^2 q_x}{\partial t^2} = \dfrac{{q_x}_j^{i+1} - 2{q_x}_j^{i} + {q_x}_j^{i-1}}{(\Delta t)^2}, \\
\dfrac{\partial q_y}{\partial t} = \dfrac{{q_y}_j^{i+1} - {q_y}_j^{i-1}}{2\Delta t}, \qquad \dfrac{\partial^2 q_y}{\partial t^2} = \dfrac{{q_y}_j^{i+1} - 2{q_y}_j^{i} + {q_y}_j^{i-1}}{(\Delta t)^2}, \\
\dfrac{\partial u}{\partial s} = \dfrac{u_{j+1}^{i} - u_{j-1}^{i}}{2\Delta s}, \qquad \dfrac{\partial^2 u}{\partial s^2} = \dfrac{u_{j+1}^{i} - 2u_j^{i} + u_{j-1}^{i}}{(\Delta s)^2}, \\
\dfrac{\partial^4 u}{\partial s^4} = \dfrac{u_{j+2}^{i} - 4u_{j+1}^{i} + 6u_j^{i} - 4u_{j-1}^{i} + u_{j-2}^{i}}{(\Delta s)^4}, \\
\dfrac{\partial v}{\partial s} = \dfrac{v_{j+1}^{i} - v_{j-1}^{i}}{2\Delta s}, \qquad \dfrac{\partial^2 v}{\partial s^2} = \dfrac{v_{j+1}^{i} - 2v_j^{i} + v_{j-1}^{i}}{(\Delta s)^2}, \\
\dfrac{\partial^4 v}{\partial s^4} = \dfrac{v_{j+2}^{i} - 4v_{j+1}^{i} + 6v_j^{i} - 4v_{j-1}^{i} + v_{j-2}^{i}}{(\Delta s)^4}, \\
\dfrac{\partial w}{\partial s} = \dfrac{w_{j+1}^{i} - w_{j-1}^{i}}{2\Delta s}, \qquad \dfrac{\partial^2 w}{\partial s^2} = \dfrac{w_{j+1}^{i} - 2w_j^{i} + w_{j-1}^{i}}{(\Delta s)^2}, \\
\dfrac{\partial^4 w}{\partial s^4} = \dfrac{w_{j+2}^{i} - 4w_{j+1}^{i} + 6w_j^{i} - 4w_{j-1}^{i} + w_{j-2}^{i}}{(\Delta s)^4}, \\
\dfrac{dx}{ds} = a\left(a^2 + s_j^2\right)^{-\frac{1}{2}}, \qquad \dfrac{d^2 x}{ds^2} = -a s_j\left(a^2 + s_j^2\right)^{-\frac{3}{2}}, \\
\dfrac{dy}{ds} = s_j\left(a^2 + s_j^2\right)^{-\frac{1}{2}}, \qquad \dfrac{d^2 y}{ds^2} = \left(a^2 + s_j^2\right)^{-\frac{1}{2}} - s_j^2\left(a^2 + s_j^2\right)^{-\frac{3}{2}}, \\
T_{Aj} = W_e\left(a^2 + s_j^2\right)^{\frac{1}{2}}, \\
{U_{rel}}_j^{i} = \left(\left(\dfrac{u_j^{i} - u_j^{i-1}}{\Delta t}\right)^2 + \left(\dfrac{v_j^{i} - v_j^{i-1}}{\Delta t}\right)^2 + \left(U_0 - \dfrac{w_j^{i} - w_j^{i-1}}{\Delta t}\right)^2\right)^{\frac{1}{2}}
\end{cases}
\tag{32}
$$

$$
\left\{
\begin{aligned}
&\left(\frac{1}{(\Delta t)^2}+\frac{2c+\rho D C_{DM} {U_{rel}}_j^i}{4(m+m_a)\Delta t}\right)u_j^{i+1}=\frac{\rho D {U_{rel}}_j^i {q_x}_j^i C_{L0}\left(U_0-\dfrac{w_j^i-w_j^{i-1}}{\Delta t}\right)}{4(m+m_a)}+\frac{EA_r}{m+m_a}\left(2{x_j}'{x_j}''\frac{u_{j+1}^i-u_{j-1}^i}{2\Delta s}+\left({x_j}''{y_j}'+{x_j}'{y_j}''\right)\frac{v_{j+1}^i-v_{j-1}^i}{2\Delta s}+{x_j}'{y_j}'\frac{v_{j+1}^i-2v_j^i+v_{j-1}^i}{(\Delta s)^2}\right)\\
&\qquad+\frac{T_{Aj}+EA_r{x_j}'^2}{m+m_a}\frac{u_{j+1}^i-2u_j^i+u_{j-1}^i}{(\Delta s)^2}-\frac{EI}{m+m_a}\frac{u_{j+2}^i-4u_{j+1}^i+6u_j^i-4u_{j-1}^i+u_{j-2}^i}{(\Delta s)^4}+\frac{2u_j^i}{(\Delta t)^2}-\left(\frac{1}{(\Delta t)^2}-\frac{2c+\rho D C_{DM} {U_{rel}}_j^i}{4(m+m_a)\Delta t}\right)u_j^{i-1},\\
&\left(\frac{1}{(\Delta t)^2}+\frac{2c+\rho D C_{DM} {U_{rel}}_j^i}{4(m+m_a)\Delta t}\right)v_j^{i+1}=\frac{\rho D {U_{rel}}_j^i {q_y}_j^i C_{L0}\left(U_0-\dfrac{w_j^i-w_j^{i-1}}{\Delta t}\right)}{4(m+m_a)}+\frac{EA_r}{m+m_a}\left(2{y_j}'{y_j}''\frac{v_{j+1}^i-v_{j-1}^i}{2\Delta s}+\left({x_j}''{y_j}'+{x_j}'{y_j}''\right)\frac{u_{j+1}^i-u_{j-1}^i}{2\Delta s}+{x_j}'{y_j}'\frac{u_{j+1}^i-2u_j^i+u_{j-1}^i}{(\Delta s)^2}\right)\\
&\qquad+\frac{T_{Aj}+EA_r{y_j}'^2}{m+m_a}\frac{v_{j+1}^i-2v_j^i+v_{j-1}^i}{(\Delta s)^2}-\frac{EI}{m+m_a}\frac{v_{j+2}^i-4v_{j+1}^i+6v_j^i-4v_{j-1}^i+v_{j-2}^i}{(\Delta s)^4}+\frac{2v_j^i}{(\Delta t)^2}-\left(\frac{1}{(\Delta t)^2}-\frac{2c+\rho D C_{DM} {U_{rel}}_j^i}{4(m+m_a)\Delta t}\right)v_j^{i-1},\\
&\left(\frac{1}{(\Delta t)^2}+\frac{2c+\rho D C_{DM} {U_{rel}}_j^i}{4(m+m_a)\Delta t}\right)w_j^{i+1}=\frac{\rho D C_{L0} {U_{rel}}_j^i {q_y}_j^i\left(\dfrac{v_j^{i+1}-v_j^{i-1}}{2\Delta t}-\dfrac{s_j}{a}\dfrac{u_j^{i+1}-u_j^{i-1}}{2\Delta t}\right)}{4(m+m_a)}+\frac{\rho D C_{DM} U_0 {U_{rel}}_j^i}{2(m+m_a)}+\frac{\rho D\varphi {C_{L0}}^2}{8(m+m_a)}{{q_y}_j^i}^2\left(1+\frac{{s_j}^2}{a^2}\right)\left(U_0-\frac{w_j^i-w_j^{i-1}}{\Delta t}\right)\left|U_0-\frac{w_j^i-w_j^{i-1}}{\Delta t}\right|\\
&\qquad+\frac{T_{Aj}}{m+m_a}\frac{w_{j+1}^i-2w_j^i+w_{j-1}^i}{(\Delta s)^2}-\frac{EI}{m+m_a}\frac{w_{j+2}^i-4w_{j+1}^i+6w_j^i-4w_{j-1}^i+w_{j-2}^i}{(\Delta s)^4}+\frac{2w_j^i}{(\Delta t)^2}-\left(\frac{1}{(\Delta t)^2}-\frac{2c+\rho D C_{DM} {U_{rel}}_j^i}{4(m+m_a)\Delta t}\right)w_j^{i-1},\\
&\left(\frac{1}{(\Delta t)^2}+\frac{\varepsilon\omega_s}{2\Delta t}\left(\frac{{{q_x}_j^i}^2}{{y_j}'^2}-1\right)\right){q_x}_j^{i+1}=\frac{A}{D}\frac{u_j^{i+1}-2u_j^i+u_j^{i-1}}{(\Delta t)^2}+\kappa\frac{\omega_s^4 D\dfrac{w_j^{i+1}-2w_j^i+w_j^{i-1}}{(\Delta t)^2}}{\omega_s^4D^2+\left(\dfrac{w_j^{i+1}-2w_j^i+w_j^{i-1}}{(\Delta t)^2}\right)^2}{q_x}_j^i-\left(\frac{1}{(\Delta t)^2}-\frac{\varepsilon\omega_s}{2\Delta t}\left(\frac{{{q_x}_j^i}^2}{{y_j}'^2}-1\right)\right){q_x}_j^{i-1}-\left(\omega_s^2-\frac{2}{(\Delta t)^2}\right){q_x}_j^i,\\
&\left(\frac{1}{(\Delta t)^2}+\frac{\varepsilon\omega_s}{2\Delta t}\left(\frac{{{q_y}_j^i}^2}{{x_j}'^2}-1\right)\right){q_y}_j^{i+1}=\frac{A}{D}\frac{v_j^{i+1}-2v_j^i+v_j^{i-1}}{(\Delta t)^2}+\kappa\frac{\omega_s^4 D\dfrac{w_j^{i+1}-2w_j^i+w_j^{i-1}}{(\Delta t)^2}}{\omega_s^4D^2+\left(\dfrac{w_j^{i+1}-2w_j^i+w_j^{i-1}}{(\Delta t)^2}\right)^2}{q_x}_j^i-\left(\frac{1}{(\Delta t)^2}-\frac{\varepsilon\omega_s}{2\Delta t}\left(\frac{{{q_y}_j^i}^2}{{x_j}'^2}-1\right)\right){q_y}_j^{i-1}-\left(\omega_s^2-\frac{2}{(\Delta t)^2}\right){q_y}_j^i,
\end{aligned}
\right. \tag{33}
$$

Finally, by introducing the difference scheme in Equation (31), the discrete equation can be obtained as shown in Equation (33).

### 2.5.2 Boundary conditions

At the initial status ($t = 0$), the displacement and the velocity are all set to zero in Global coordinate frame. A one-wavenumber excitation with amplitude of order O (1) is applied to the wake oscillator $q$ and the first derivative is also set to zero. These can be expressed as:

$$u = v = w = \frac{\partial u}{\partial t} = \frac{\partial v}{\partial t} = \frac{\partial w}{\partial t} = \frac{\partial q_x}{\partial t} = \frac{\partial q_y}{\partial t} = 0. \tag{34}$$

Considering bending has the greater effect for the tension on flexible cables, in this study the hinged boundary conditions are used. Since the two ends of the cable are hinged, the displacement and the bending moment at both top end and bottom end are zero, expressed as:

$$\begin{cases} u(t,0) = u(t,L) = 0, & \dfrac{\partial^2 u(t,0)}{\partial s^2} = \dfrac{\partial^2 u(t,L)}{\partial s^2} = 0, \\ v(t,0) = \mathrm{v}(t,L) = 0, & \dfrac{\partial^2 v(t,0)}{\partial s^2} = \dfrac{\partial^2 v(t,L)}{\partial s^2} = 0, \\ w(t,0) = \mathrm{w}(t,L) = 0, & \dfrac{\partial^2 w(t,0)}{\partial s^2} = \dfrac{\partial^2 w(t,L)}{\partial s^2} = 0, \end{cases} \tag{35}$$

Substituting Equation (34) (35) into Equation (32), the following discretized boundary equation can be obtained:

$$\begin{gathered} u_j^0 = u_j^2,\ v_j^0 = v_j^2,\ w_j^0 = w_j^2,\ {q_x}_j^0 = {q_x}_j^2,\ {q_y}_j^0 = {q_y}_j^2, \\ u_0^i = -u_2^i,\ v_0^i = -v_2^i,\ w_0^i = -w_2^i, \\ u_{N+2}^i = -u_N^i,\ v_{N+2}^i = -v_N^i,\ w_{N+2}^i = -w_N^i. \end{gathered} \tag{36}$$

Substituting Equation (36) into Equation (33), the values of $u_j^i$, $v_j^i$, $w_j^i$, ${q_x}_j^i$ and ${q_y}_j^i$ ($j$=0, 1, N-1, N) near the two ends of the cable can be obtained. Accordingly, the values of $u_j^i$, $v_j^i$, $w_j^i$, ${q_x}_j^i$ and ${q_y}_j^i$ at every time steps ($i \geq 2$) can be iteratively calculated.

## 2.6 Chapter conclusion

This chapter describes a numerical model based on Euler-Bernoulli beam theory and a single van der Pol wake oscillator model is proposed to study the vortex-induced vibration of a long flexible catenary cable with a low mass ratio. The wake model uses only one oscillator to describe the in-line and cross-flow vibration with consideration of their nonlinear coupling. The numerical model is solved by the central finite difference method.

# CHAPTER 3 Tank experiment for cable model

A 1/10 experimental model, which is designed to mimic the power transmission cable for use in bottom-fixed offshore wind turbines, was developed, as illustrated in Fig 3-1. The details on the actual cable can be referred to [135-138]. The properties of the cable are given in Table 1. The bottom end of the cable is hinged to an aluminum rod which is mounted on the bottom of the water tank, and the top end of the cable is hinged to an external fixed frame, as shown in Fig 3-2. The cable model is suspended in the water tank, which is not affected by the bottom of the tank. Two non-intrusive high-speed underwater cameras (model: WTW-WA320H) are applied to record the cable inline and cross-flow motion during the experiment.

The central axis of the cable is made of a carbon rod with a diameter of 1.5 mm. The cable is assembled by aluminum lumps and plastic lumps with a diameter of 20 mm and a length of 10 mm as shown in Fig 3-3. Between the lumps, small gaskets are applied to maintain a small space so that the lumps are not in collision during the cable bending. Plastic film is used for wrapping the cable to keep the cable surface smooth. Twelve red marks with a distance of 0.1 m are added to the cable for motion tracking, and two load cells are installed at the cable ends to measure the cable axial tension as shown in Fig 3-1. The signal recorder is used to record and store the load cells data as shown in Fig 3-4. The overview of experimental setup is shown in Fig 3-5.

The experiments were carried out in the circulating water tank with a length of 5 m, a width of 1.5 m and a depth of 2 m at the Research Institute for Applied Mechanics (RIAM) of Kyushu University as shown in Fig 3-6. Firstly, free-decay experiment in still water is performed to estimate the natural frequency $f_n$ and the damping coefficient $\zeta$ of the cable [139]. Then, the flow velocities, which were measured using an acoustic doppler velocimeter (ADV) positioned 1.0 m upstream of the cable model, are set to vary from 0.2 m/s to 0.6 m/s with an interval of 0.04 m/s (the Reynolds number in terms of cable diameter is between 4,000 to 12,000). Each experiment is performed twice so that the results can be double checked. The cable motion is obtained by video processing using open source software Tracker [140]. In the following sections, the results from the second experiment are analyzed.

Table 3-1 Main parameters of experimental model

| Parameter | Value | | Unit |
|---|---|---|---|
| | Prototype | Model | |
| Cable external diameter, D | 0.2 | 0.02 | m |
| Cable mass per unit length (m) | 72 | 0.65 | kg/m |
| Mass ratio in water (m*) | 2.236 | 2.0253 | Dimensionless |
| Bending stiffness, EI | 10000 | 0.08 | $Nm^2$ |
| Axial stiffness, EA | $700*10^6$ | 500,000 | N |
| Minimum Bend Radius | 2 | 2.176 | m |
| Damping ratio, ξ | | 0.08 | Dimensionless |
| Natural frequency, fn | | 3.1 | Hz |
| length between pinned ends, L | | 1.38 | m |
| Horizontal distance between cable ends, $X_H$ | | 1.3 | m |
| Vertical distance between cable ends, $Y_H$ | | 0.4 | m |

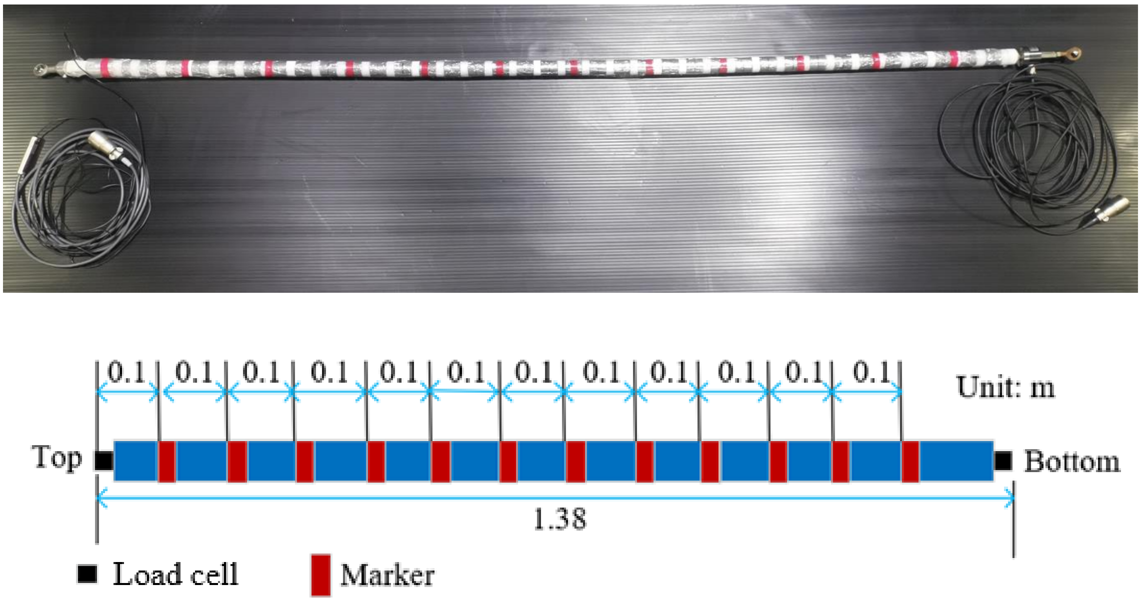


Fig.3-1 Cable model (up) and schematic drawing of the cable model with the location of the motion tracking marks (down).

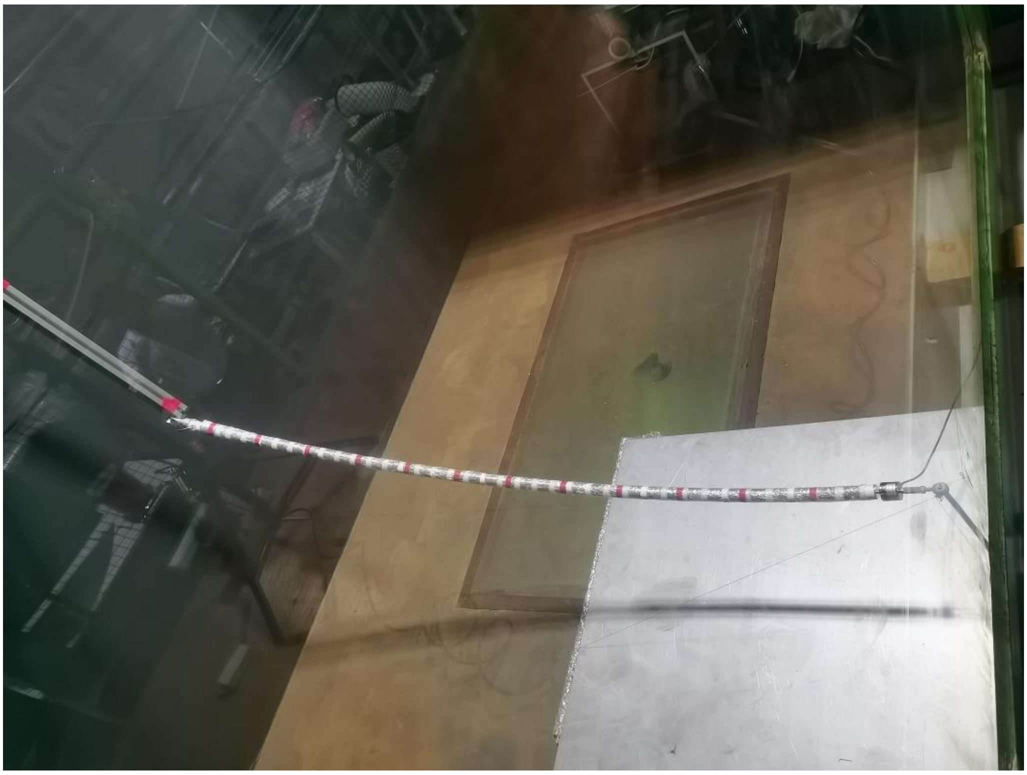

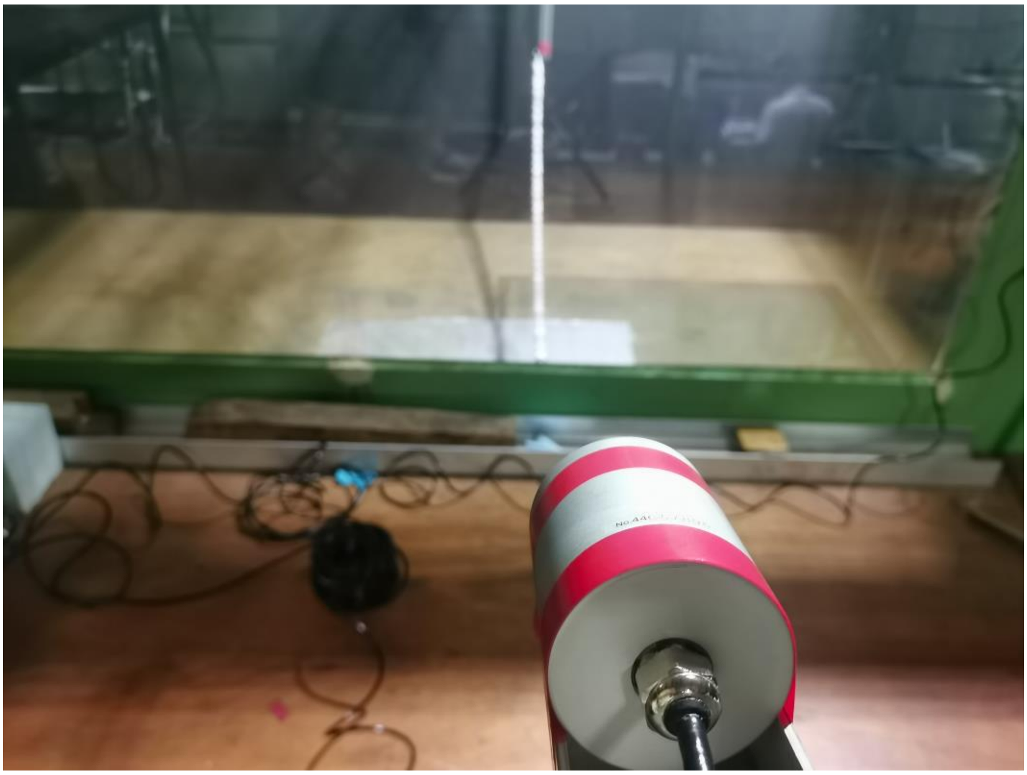

Fig.3-2 Experimental overall framework in (up) and outside (down) the water tank.

Fig.3-3 Aluminum lump (left) and plastic lump (right).


Fig.3-4 Signal recorder for the load cell

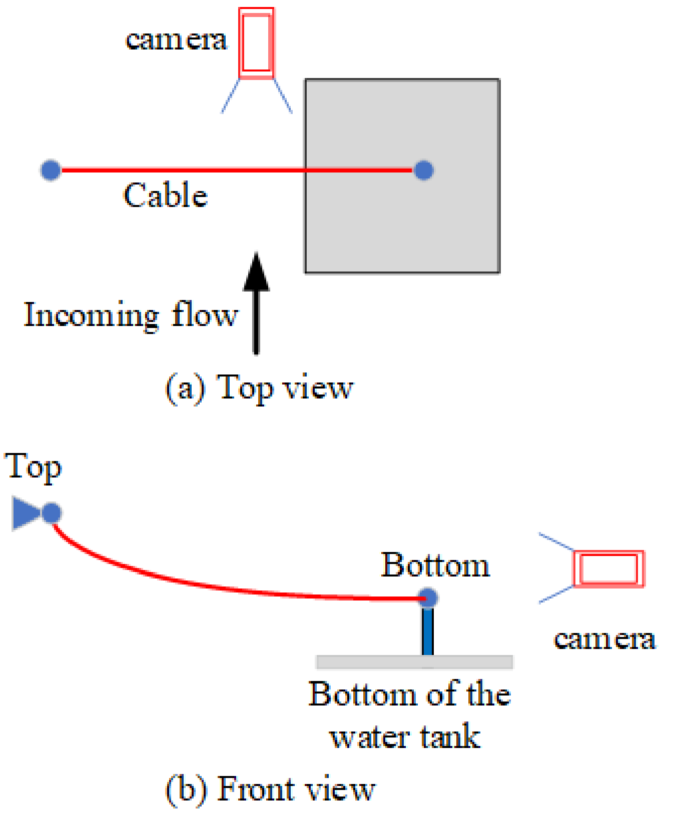


Fig.3-5 Schematic drawing of the experimental model (a) top view; (b) front view.

Fig.3-6 Circulating water tank at the Research Institute for Applied Mechanics (RIAM) of Kyushu University.

# CHAPTER 4 Empirical parameters sensitivity analysis

## 4.1 Introduction

The necessity of empirical parameters in wake oscillators arises from the inability to directly derive the nonlinearity in the damping term and coupling terms in Equation (26) [131]. Consequently, all wake oscillators must have empirical parameters to fit experimental data. To select suitable values for these empirical parameters, understanding their impact on the final simulation results is crucial. Current 2DOF VIV models typically require four empirical parameters, but for the model in this study, only three parameters need adjustment: the damping parameter (ε), the coupling term parameter associated with cross-flow motion (A), and the coupling term parameter associated with in-line motion (κ). The effects of the parameters ε, A and κ on vibration have also been explored for a rigid cylinder in [141]. But for the flexible curve cable, the effects of these parameters have not been well studied.

Although various values for the empirical parameters can be chosen, it is essential to ensure that the physical principles of the model are preserved. The empirical parameter A multiplies the motion of the structure in the cross-flow direction, while the empirical parameter κ multiplies the motion of the structure in the in-line direction, as indicated in Equation (26). If the empirical parameter κ is higher than A, it suggests that the cable is more excited in the in-line direction than in the cross-flow direction. This is not physically accurate, especially for structures with small mass ratios ($m^* < 6$), where the vibration amplitude in the cross-flow direction is significantly larger than that in the in-line direction.

Given that different sets of empirical parameters can yield very similar model responses, certain assumptions are made to maintain the physical integrity of the model:

- ✧ The damping parameter ε should not assume a negative value to avoid transferring energy to the fluid, which would result in the opposite effect of fluid damping.

✧ The value of A should consistently exceed κ, aligning with past experimental findings indicating that cross-flow vibration of the cylinder consistently surpasses in-line vibration. Therefore, setting κ higher than A would contradict this observation.

The goal of the present work is to obtain the regularity of parameters, and explore many combinations of empirical parameter values to achieve optimal agreement with the experimental data in this study. A discussion on the effects of each empirical parameter on the final results is presented herein: two empirical parameters remain unchanged while the other is altered. In the following, the effects of the parameters ε, A and κ in the single wake oscillator model Equation (26) on the cable vibration (evaluated by the maximum Root-Mean-Square (RMS) value) are studied. Many groups of simulation considering their different combinations are carried out. In each group, two of the parameters are fixed and the other one is varied, and the cable vibration amplitude is evaluated. The simulations are conducted based on the experimental data of chapter 3.

It is worth mentioning that since Reynolds number in experiment is between 4,000 to 12,000 and the flow is in the subcritical range, the parameters $C_{D0}, \overline{C_D},$ and $C_{L0}$ are assigned as $C_{D0} = 0.1$, $\overline{C_D} = 1.2$ and $C_{L0} = 0.3$. The Strouhal number is set as $St = 0.18$.

The sensitivity of the three empirical parameters is analyzed in Section 4.2. An empirical parameters error equation used to determine the optimization parameters is proposed in Section 4.3. In section 4.4, the numerical model using the above parameters is verified by experiments in the literature.

## 4.2 Empirical parameters sensitivity analysis

### 4.2.1 Damping parameter ε

This empirical parameter regulates the nonlinear damping term in the Equation (26). Consequently, selecting a value of ε close to 1 would induce strong nonlinear behavior in in the Equation (26). It is worth mentioning that while the assumption of $0 \leq \varepsilon \ll 1$ is very common in most wake oscillators, it is not strictly necessary.

The two principal effects caused by the change of the damping empirical parameter ε are the changes in the width of the lock-in range and in the maximum vibration amplitude, where $A_{rms}$ is the maximum RMS amplitude of the cable in the total direction. The results of the variation of the parameter ε on the maximum RMS of the cable vibration are shown in Fig 4-1.

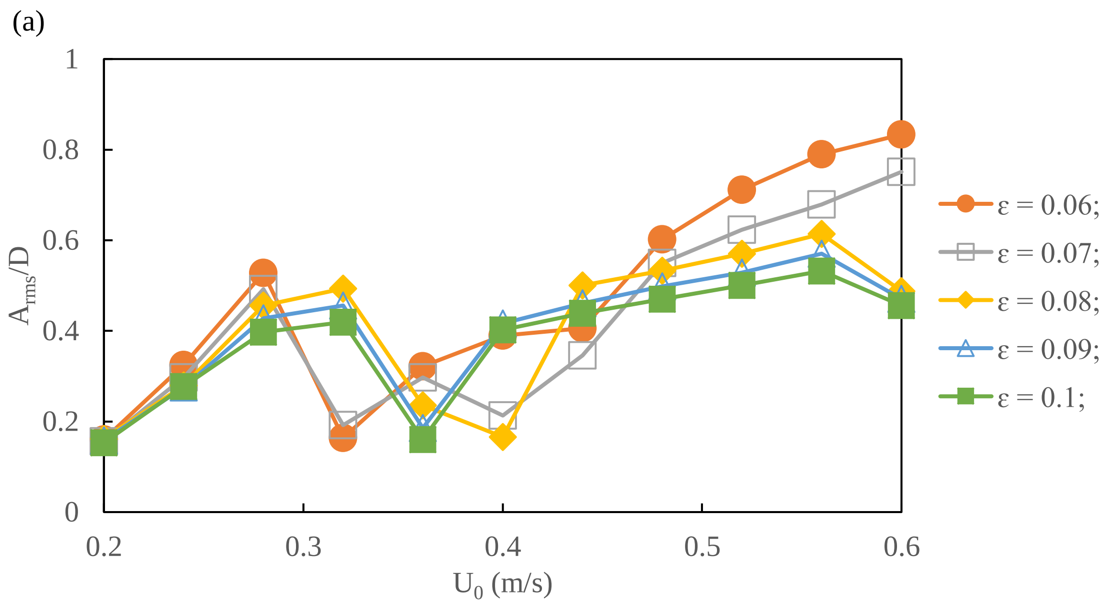


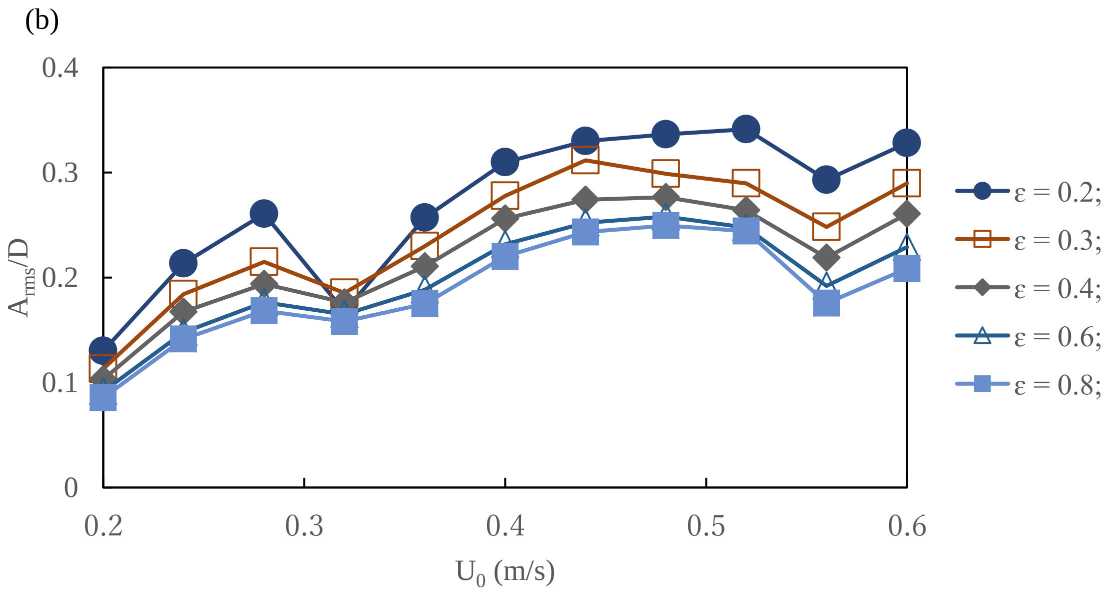

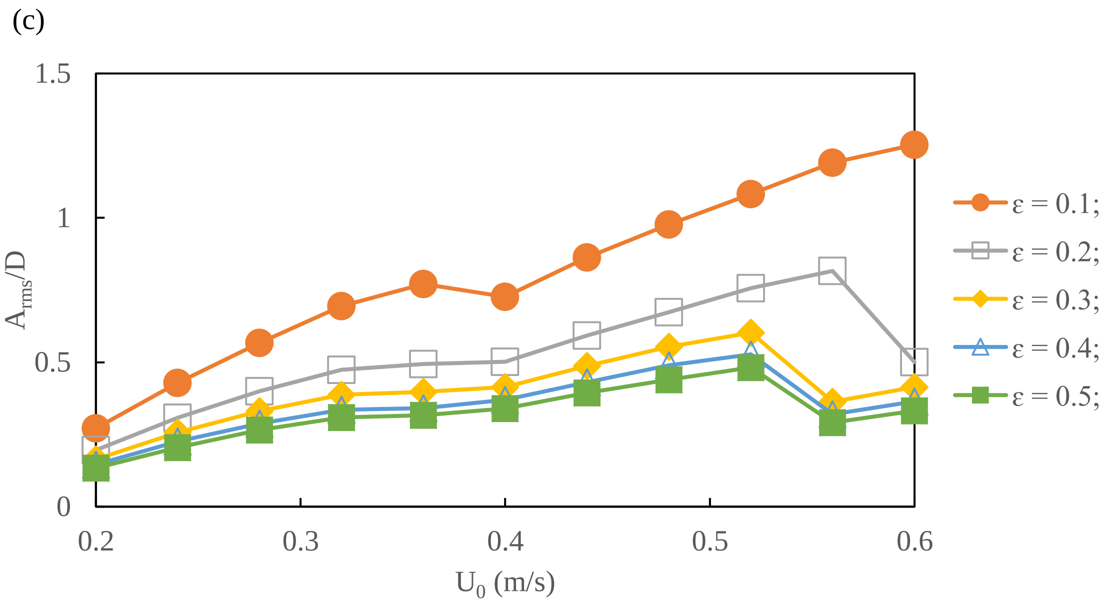


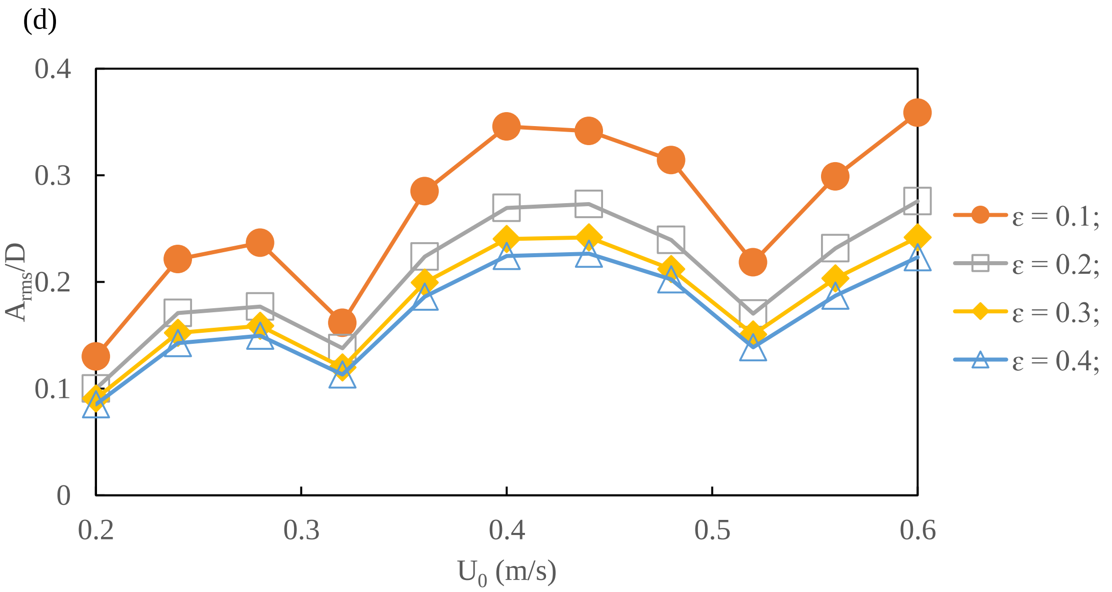


Fig.4-1 Results of the variation of the parameter ε on the maximum RMS of the cable vibration (a) A = 8, κ = 5, (b) A = 8, κ = 5, (c) A = 20, κ = 5, and (d) A = 5, κ = 2.

As shown in Fig 4-1, it is found that the vibration amplitude is reduced as ε increases. This is reasonable since ε is associated with the vibration damping. In Fig 4-1(a), it can be noticed that, for a value of ε = 0.06, the maximum RMS amplitude reaches a maximum value of $A_{rms}/D$ = 0.83. For a higher value of ε = 0.8 in Fig 4-1(b), the maximum RMS amplitude reaches a maximum value of $A_{rms}/D = 0.25$. The second effect to be considered is the change in the width of the lock-in range. As shown in Fig 4-1(c), as ε increases, the width of the lock-in range decreases. But, for ε > 0.2, the lock-in range stays the same. In Fig 4-1(d), any increase in ε will no longer generate a significant change in the lock-in range width. Moreover, the parameters A and κ also influence the width of the lock-in range, as shown in Fig 4-1(c), the first lock-in range almost disappear when ε ≥ 0.2.

### 4.2.2 Parameter A

This empirical parameter governs the coupling of the cross-flow vibration of the structure in the wake oscillator Equation (26). The results of the variation of the parameter A on the maximum RMS of the cable vibration are shown in Fig 4-2.

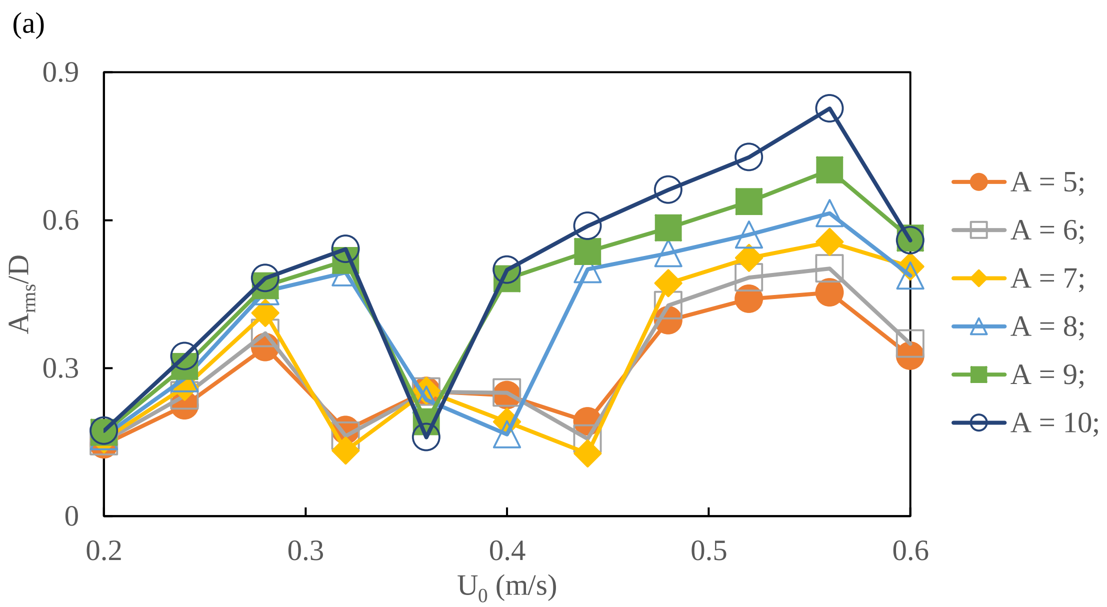

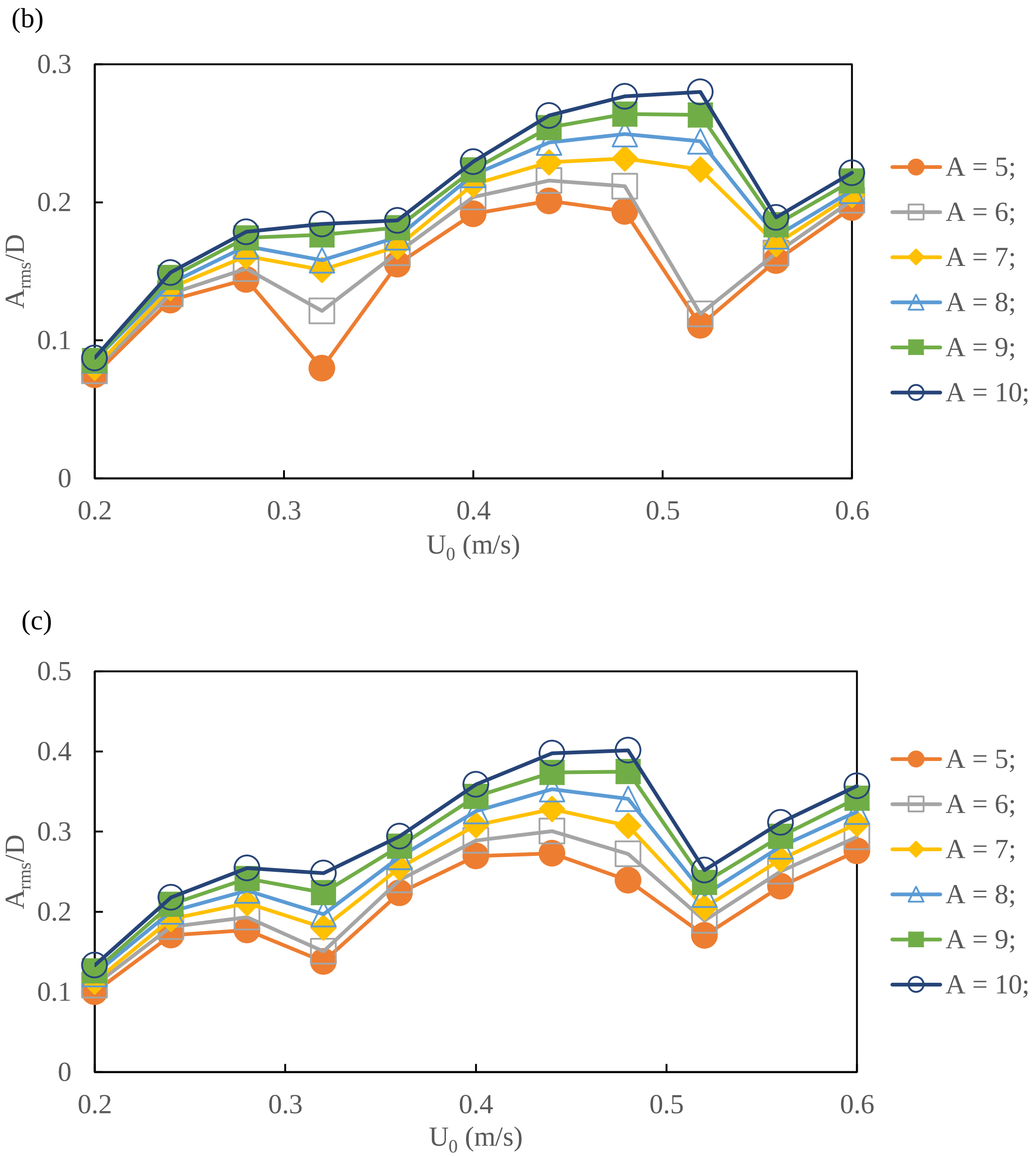


Fig.4-2 Results of the variation of the parameter A on the maximum RMS of the cable vibration (a) $\varepsilon = 0.08$ and $\kappa = 5$, (b) $\varepsilon = 0.8$ and $\kappa = 5$, and (c) $\varepsilon = 0.2$ and $\kappa = 2$.

It can be seen that as A increases, both the maximum RMS amplitude and the width of the lock-in range increase. Additionally, Meanwhile, the first lock-in regime tends to disappear. This lock-in range is absent in Fig 4-2(b) and Fig 4-2(c) for different reasons: in Fig 4-2(b), at a high damping parameter of $\varepsilon = 0.8$, there is a decrease in the in-line

RMS amplitude of vibration. in Fig 4-2(c), the parameter κ is decreased, also leading to lower values of in-line maximum RMS amplitude of vibration. Additionally, as the parameter A increases, the cross-flow vibration becomes more pronounced relative to the in-line vibration. Consequently, this leads to the tendency for the first lock-in range to disappear.

### 4.2.3 Parameter κ

This empirical parameter governs the coupling of the in-line vibration of the structure in the wake oscillator Equation (26) within the nonlinear term $\kappa \frac{\omega_s^4 D\ddot{w}}{\omega_s^4 D^2+(\ddot{w})^2} q$. It is worth mentioning that due to this nonlinearity, the response of the wake oscillator is more sensitive with the change in the parameter κ when compared with the same change in the parameter A. The results of the variation of the parameter κ on the maximum RMS of the cable vibration are shown in Fig 4-3.

(a)

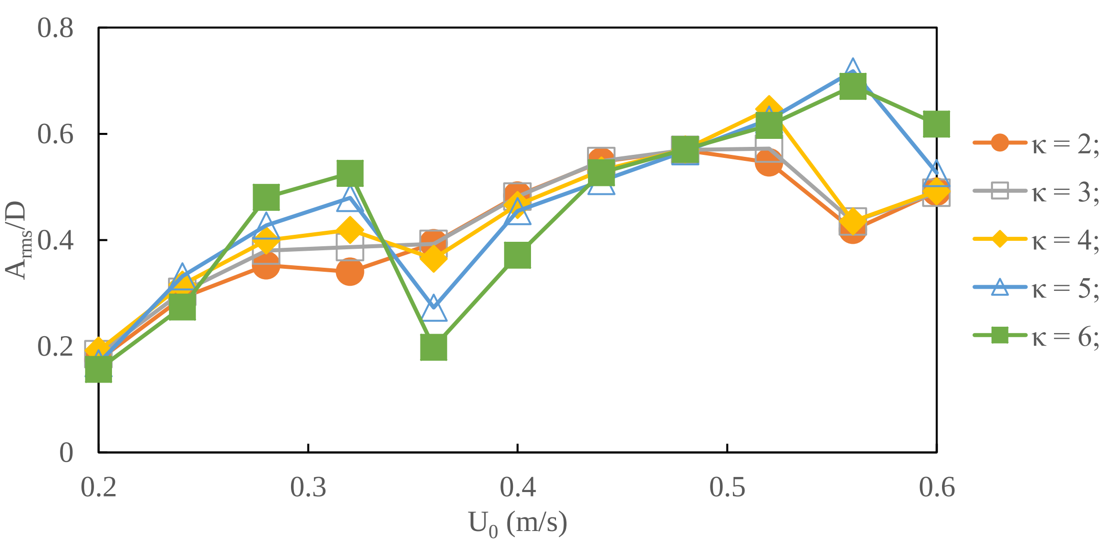

(b)

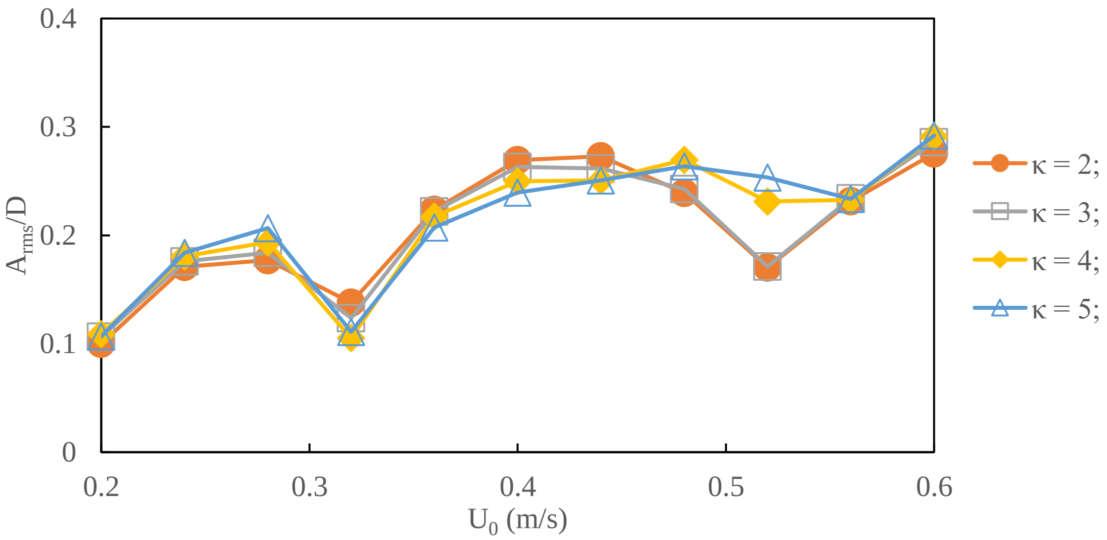


(c)

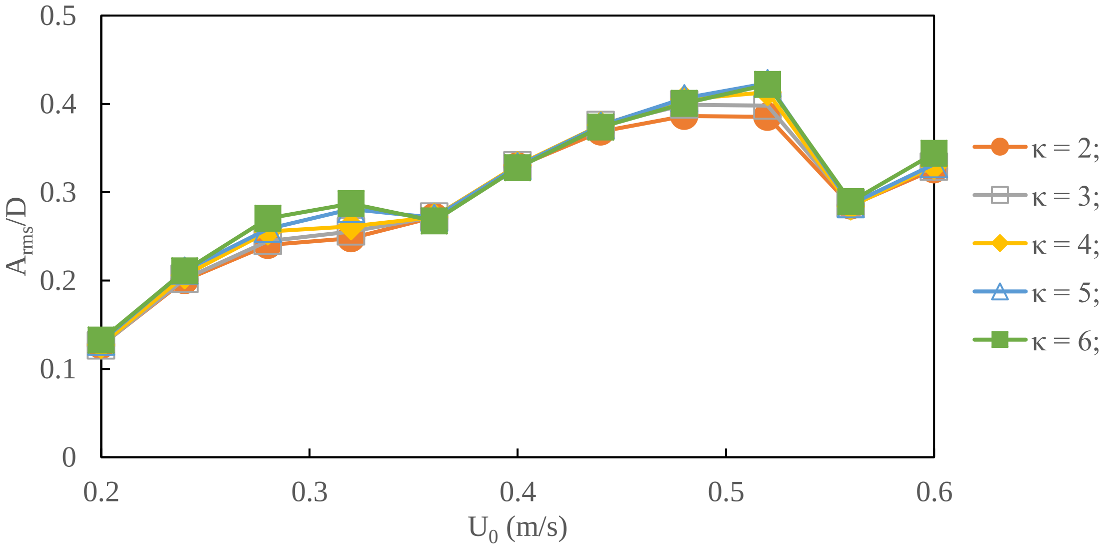


Fig.4-3 Results of the variation of the parameter κ on the maximum RMS of the cable vibration (a) A = 10 and ε = 0.1, (b) A = 5 and ε = 0.2, and (c) A = 12 and ε = 0.3.

As shown in Fig 4-3, as κ increases, the cable vibration as a function of the flow velocities becomes more sensitive, meanwhile, the first lock-in area tends to be more visible, this may occur because as κ increases, the in-line vibration increases, leading the first lock-in range to tend to be more visible. In addition, in Fig 4-3(b) and Fig 4-3(c), the damping parameter ε assumed higher values when compared to Fig 4-3(a). With this, any changes in κ will have a minor impact on the vibration amplitude of the cable, but the trend is still visible.

To sum up, the change in the parameters primarily affects two aspects: the width of the lock-in range and the maximum vibration amplitudes. Meanwhile, the first lock-in area requires appropriate parameter values to be more visible.

## 4.3 Error equation

As shown in Fig 4-4, to obtain the slope of experimental results, the RMS vibration amplitude curve as the flow velocity $U_0$ can be derived by fitting the experimental data. It is worth mentioning that in the curve fitting process, a regularization method is used to prevent overfitting. To ensure that the numerical model accurately reflects the experimental results, an empirical parameters error equation is proposed:

$$E_j = \lambda \sum_i \frac{|B_{ni} - B_{ei}|}{max|B_{ni} - B_{ei}|} + \eta \sum_i \frac{\left|\frac{dB_{ni}}{dU_0} - \frac{dB_{ei}}{dU_0}\right|}{max\left|\frac{dB_{ni}}{dU_0} - \frac{dB_{ei}}{dU_0}\right|}, \tag{37}$$

where $E$ represent the error value, j represent direction (X, Y, Z, and total direction), i represent flow velocity, $B_n$ and $B_e$ are the maximum RMS vibration amplitudes for numerical and experimental results in the corresponding direction, respectively; $\frac{dB_{ni}}{dU_0}$ and $\frac{dB_{ei}}{dU_0}$ respectively represent the slope of fitted curve for numerical and experimental results when velocity is i; Because the slope error (< 10) is much greater than the amplitude error (< 1) in numerical simulation, the normalization is used. λ and η represent the size and slope coefficient, respectively. Considering the slope change is more important, $\lambda = 1$ and $\eta = 10$ are selected.

This equation is used to compare both the magnitude and the slope of the numerical fitting curves with the experimental data, thereby identifying the optimal parameters. This ensures that the numerical model accurately reflects the experimental observations, providing reliable and robust predictions of the RMS vibration amplitude across different velocities. By calculating various combinations of parameter values, applying the error equation to measure the accuracy of each combination, and fine-tuning the parameters to best fit the experimental data, the optimal parameters that minimize the discrepancy between the numerical model and experimental results can be identified.

Finally, $A = 9$, $\varepsilon = 0.1$ and $\kappa = 5$ are selected. It is worth mentioning that all subsequent calculations will use these values in this study.

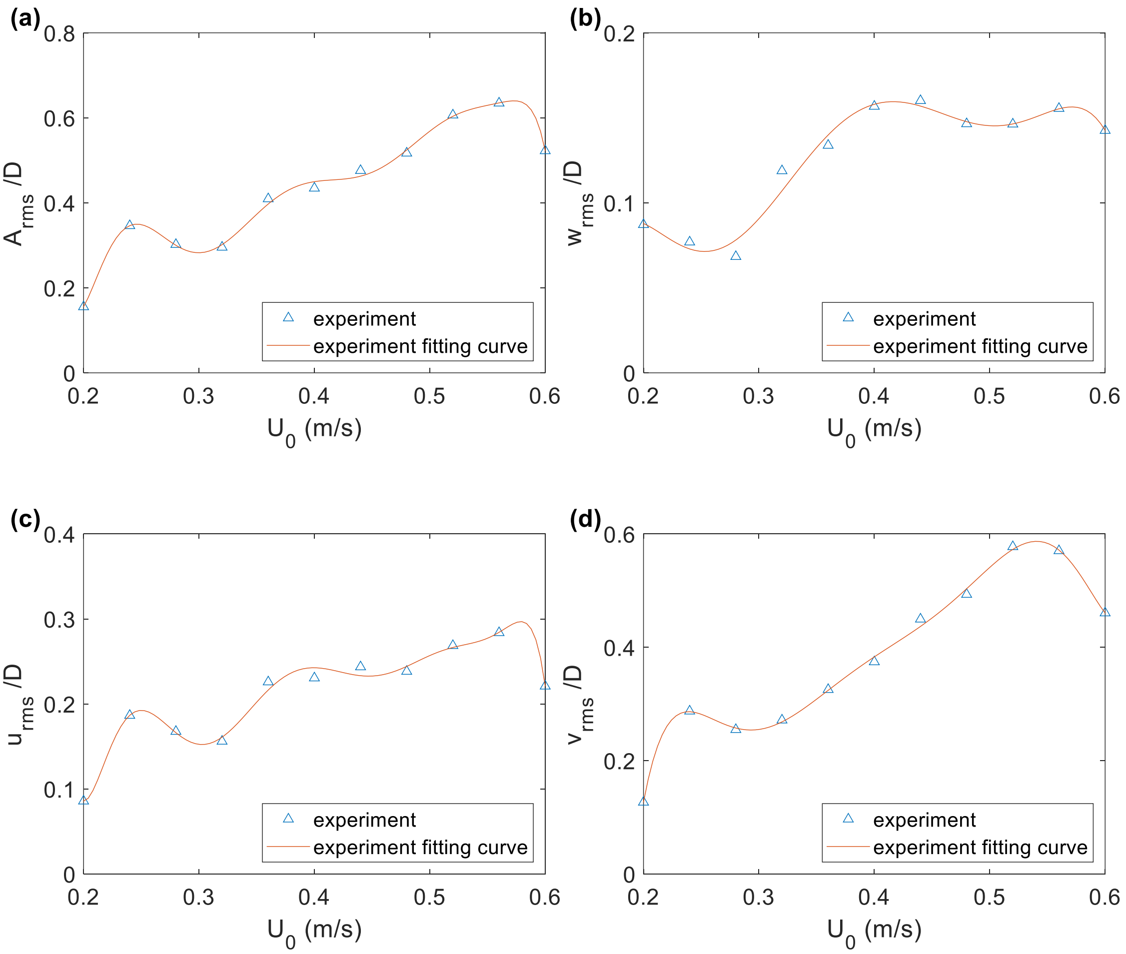


Fig.4-4 Spatially maximum RMS vibration amplitudes for experimental results and fitted curve with the flow velocity $\boldsymbol{U_0}$ (a) total RMS vibration amplitudes; (b) in-line w RMS vibration amplitudes; (c) cross-flow u RMS vibration amplitudes; (d) cross-flow v RMS vibration amplitudes.

## 4.4 Model validation

As mentioned above, all parameters have been selected:

$$A = 9, \quad \varepsilon = 0.1, \quad \kappa = 5,$$
$$C_{D0} = 0.1, \quad \overline{C_D} = 1.2, \quad C_{L0} = 0.3, \quad St = 0.18. \tag{38}$$

To validate the current numerical model employing a single wake oscillator, numerical predictions are compared with experimental results for long flexible cylinders experiencing VIV in the literature. The validation process ensures the accuracy of the numerical model by considering various riser geometries, including both straight and curved configurations. This validation is based on available experimental input-output data, allowing for a comprehensive parametric setup in the simulation. The main input parameters of the selected experimental models are summarized in Table 4-1 below. Before discussing and studying the validation, the response convergence of the time step ($\Delta$t) and spatial discretization segment (N) is studied.

Table 4-1 Main parameters of experiment used for model validation

| Input | Song et al. [142] | Moe et al. [49] |
|---|---|---|
| External diameter, $D$ (m) | 0.016 | 0.014 |
| Length, $L$ (m) | 28.04 | 12.5 |
| Mass per unit length, $m$ (kg/m) | 0.2 | 0.357 |
| Mass ratio in water, $m^*$ | 1 | 2.26 |
| Damping ratio, $\xi$ | 0.01 | 0.006 |
| Horizontal tension, $T_H$ (N) | 700 | 13.5 |
| Young's modulus, $E$ (N/m$^2$) | $2.1*10^{11}$ | $1.05*10^{11}$ |
| Bending stiffness, $EI$ (Nm$^2$) | 153.7 | 46.2 |
| Axial stiffness, $EA$ (N) | - | $2.01*10^{6}$ |
| Horizontal distance between two ends, $X_H$ (m) | - | 9.253 |
| Vertical distance between two ends, $Y_H$ (m) | - | 7.13 |

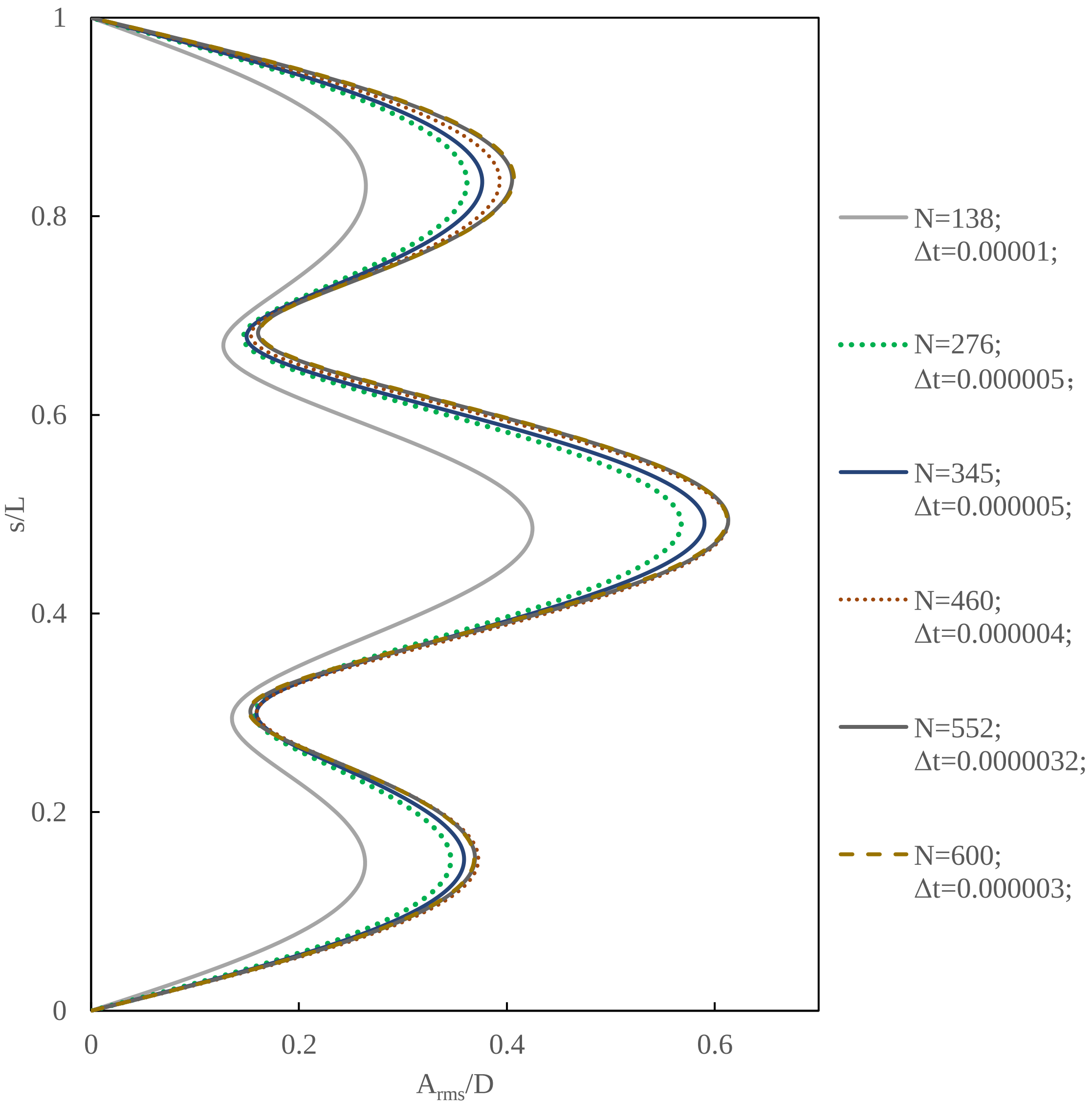


Fig.4-5 Spatial total RMS response envelopes at $U_0 = 0.56\ \mathrm{m/s}$ with varying time step (Δt) and spatial discretization segment (N).

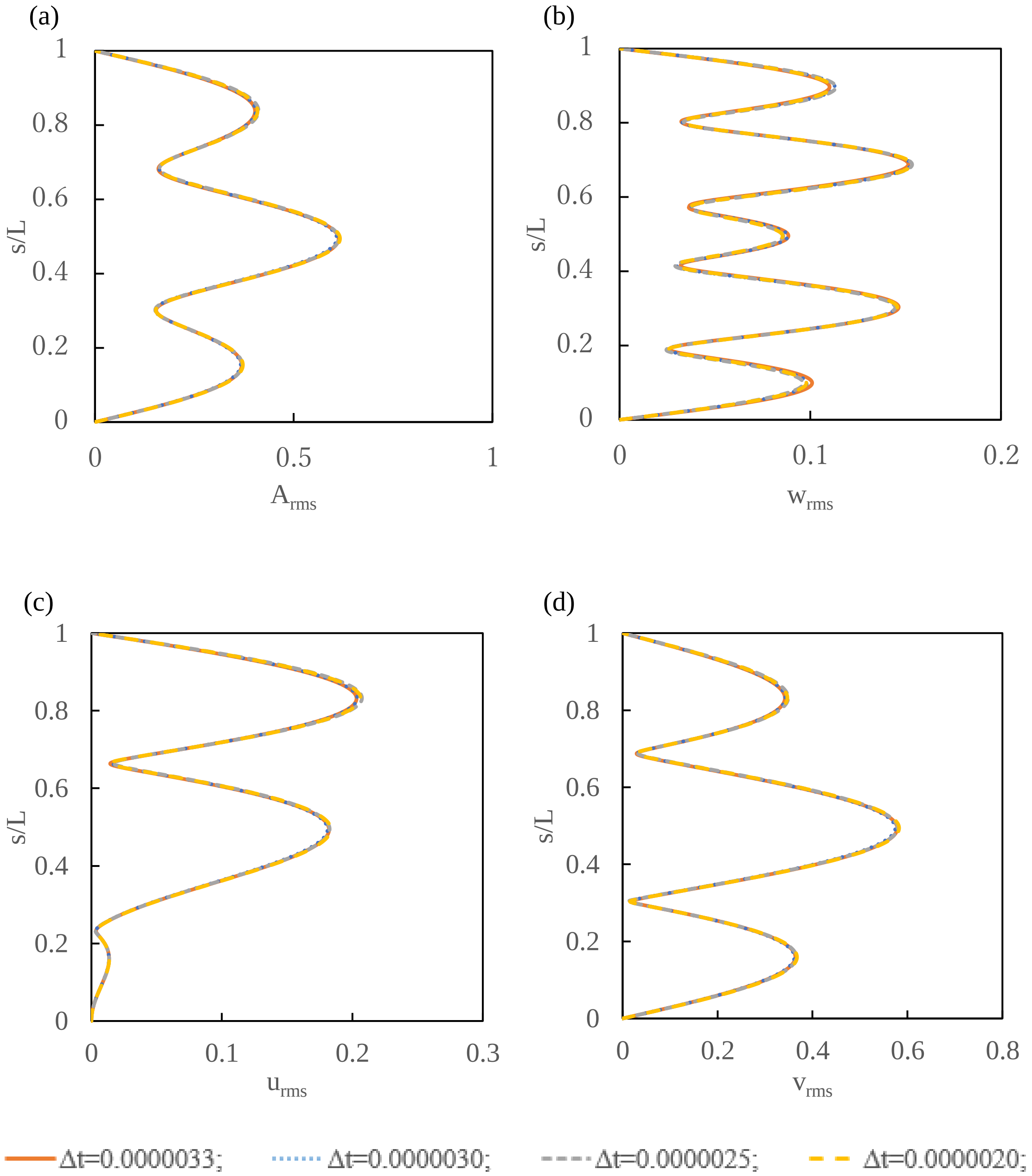


Fig.4-6 Spatial RMS response envelopes at $U_0 = 0.56\ \mathrm{m/s}$ with varying time step (Δt) at spatial discretization segment N = 552; (a) total RMS vibration amplitudes; (b) in-line w RMS vibration amplitudes; (c) cross-flow u RMS vibration amplitudes; (d) cross-flow v RMS vibration amplitudes.

### 4.4.1 Time step and spatial discretization segment

The independence study of the time step (Δt) and spatial discretization segment (N) used in the numerical simulation under $U_0 = 0.56\ \mathrm{m/s}$ is as shown in Fig 4-5 and Fig 4-6. By comparing the RMS response envelopes at different time step (Δt) and spatial discretization segment (N), the results show that the response convergence in terms of both quantitative and qualitative features. Therefore, the time step (Δt = 0.0000033) is used in the time integration, while spatial discretization segment (N =552) is used in the finite difference approximation. It is worth mentioning that all subsequent calculations will use these values.

### 4.4.2 Comparison with a straight cylinder

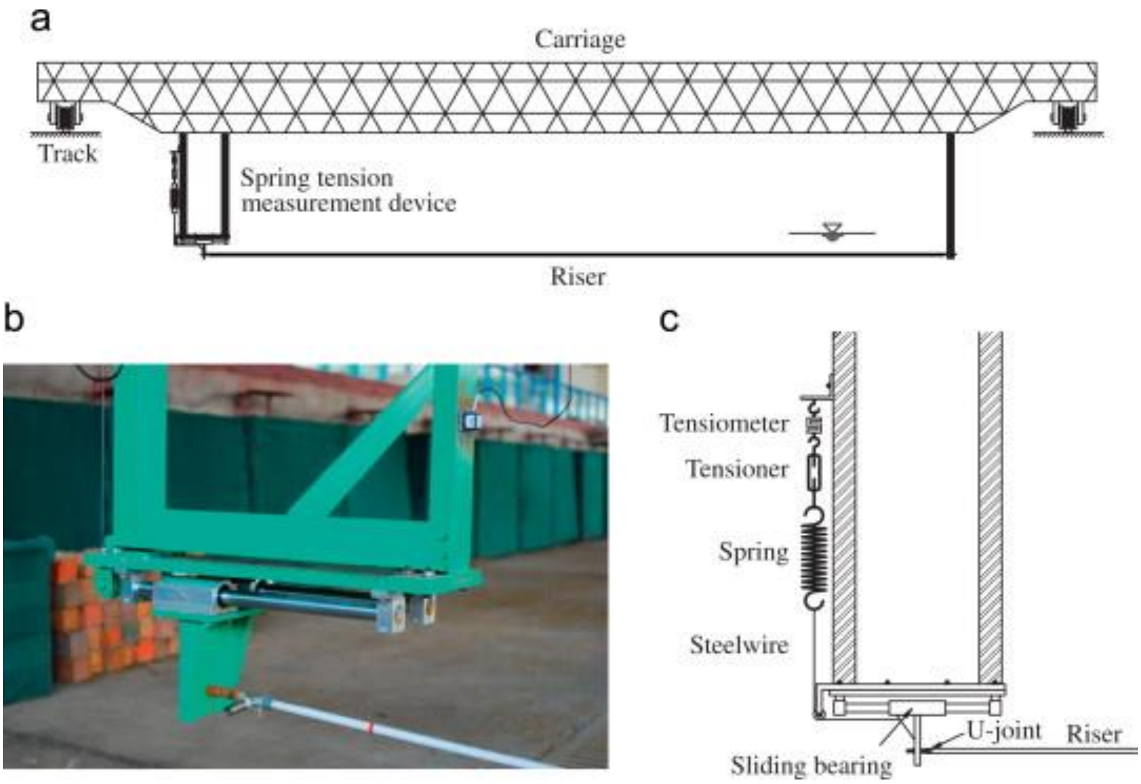


Fig.4-7 Sketch of the experiments (Song et al, 2011) [142].

A laboratory test conducted in a wave basin by Song et al. focusing on a long horizontal flexible pipe with a high aspect ratio (L/D ≈ 1752), is considered [142]. The sketch of the experimental setup is as shown in Fig. 4-7. The pipe was towed in still water at a spatially uniform flow within the range of 0.1–0.6 m/s and associated Reynolds number (Re) in terms of pipe diameter is between 3,000 to 10,000. Throughout the experiments, various pre-tensions were applied, maintaining spatial constancy along the pipe to achieve a neutrally buoyant condition with $m^* = 1$. Consequently, the influence of gravity on the static configuration was disregarded. Fiber optic strain gauges were used to measure the vortex-induced vibration responses.

A horizontal straight cylinder can be seen as a special form of a curved cylinder. Considering a horizontal straight cylinder with a longitudinal X-axis (unmovable in X-axis), and experiencing in-line and cross-flow VIV in the Z (towing) and Y (vertical) directions respectively (refer to Fig 2-1), it amounts to $x' = 1$, $y' = 0$ and $\beta' = 0$. Given that the flow in the Z direction is uniformly perpendicular to the horizontal span, the Equation (31) could reduce to

$$\begin{cases} \ddot{v} + \dfrac{2c + \rho D C_{DM} U_{rel}}{2(m+m_a)}\dot{v} + \dfrac{EI}{m+m_a}v'''' - \dfrac{T_A}{m+m_a}v'' = \dfrac{\rho D U_{rel} q_y C_{L0}(U_0 - \dot{w})}{4(m+m_a)}, \\ \ddot{w} + \dfrac{2c + \rho D C_{DM} U_{rel}}{2(m+m_a)}\dot{w} + \dfrac{EI}{m+m_a}w'''' - \dfrac{T_A}{m+m_a}w'' \\ \quad = \dfrac{\rho D C_{L0} U_{rel} q_y \dot{v}}{4(m+m_a)} + \dfrac{\rho D C_{DM} U_0 U_{rel}}{2(m+m_a)} + \dfrac{\rho D \varphi {C_{L0}}^2}{8(m+m_a)} {q_y}^2 (U_0 - \dot{w})|U_0 - \dot{w}|, \\ \ddot{q_y} + \varepsilon\omega_s(q_y^2 - 1)\dot{q_y} + \omega_s^2 q_y - \kappa\dfrac{\omega_s^4 D \ddot{w}}{\omega_s^4 D^2 + (\ddot{w})^2} q_y = \dfrac{A}{D}\ddot{v}, \\ U_{rel} = \sqrt{\dot{v}^2 + (U_0 - \dot{w})^2}. \end{cases} \tag{39}$$

The Equation (39) could be seen as a single wake oscillator equation for a straight cylinder. The numerical simulation is conducted with the same parameters in the experiment as shown in Table 4-1, and the results are as follows:

The comparison of nondimensional spatially cross-flow maximum amplitudes with varying flow velocity $U_0$ is illustrated in Fig. 4-8. It can be seen that the cross-flow dynamic responses of the numerical model align well with the experimental results, both qualitatively and quantitatively. A stepwise-increasing amplitude trend with increasing $U_0$ can be observed in the experimental and numerical results, which can be attributed to dominant mode switching. This agreement between the numerical and experimental results underscores the accuracy of the model in capturing the key dynamics of VIV under varying flow conditions.

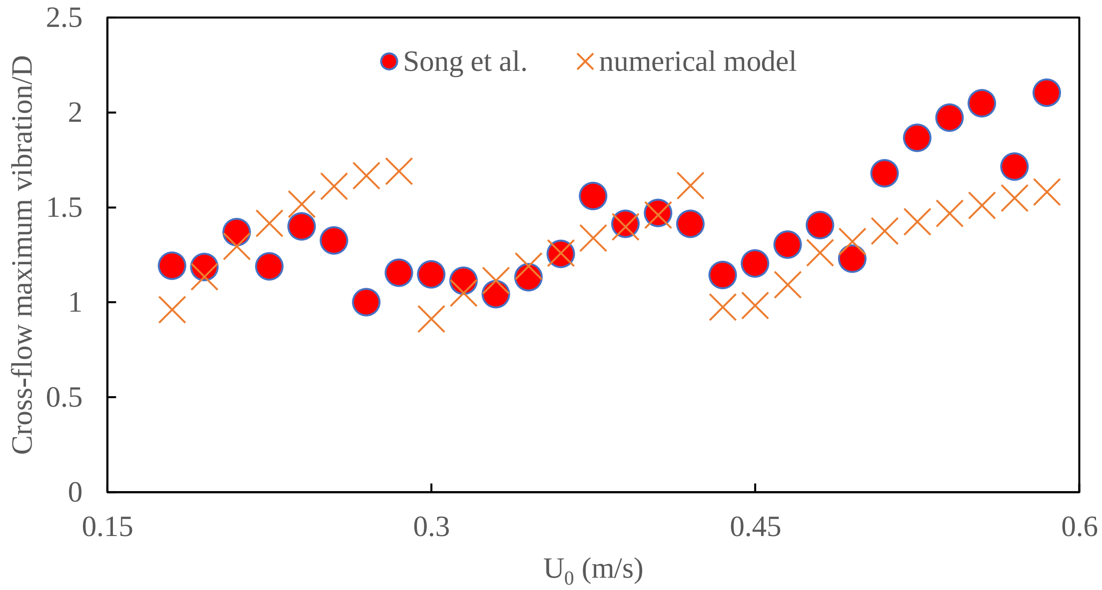


Fig.4-8 Comparison of numerical and experimental results with spatially maximum amplitudes for cross-flow VIV responses.

### 4.4.3 Comparison with a flexible curved cylinder

To validate the present model used for a flexible curved cylinder, a numerical study is conducted based on the catenary riser experiment by Moe et al. [49]. A sketch of the experimental setup is provided in Fig. 4-9. In the experiment, a Steel Catenary Riser model with a low mass ratio ($m^* = 2.26$) was fully submerged and towed at a uniform flow velocity ($U_0 = 0.26\ m/s$) at various incoming flow angles to study VIV behaviors.

Ten accelerometers were deployed to measure the total vibration displacements in the time domain, which correspond to $(u^2 + v^2 + w^2)^{\frac{1}{2}}$ in the present numerical model.

The case in which the incoming flow angle is perpendicular to the riser is selected to compare our numerical results, as shown in Fig. 4-10(c). The corresponding contours of spatial-temporal varying cross-flow n and in-line w responses are shown in Fig 4-10(a) and (b), respectively. It can be seen in the cross-flow direction (Fig 4-10(a)), the riser vibrates with a standing wave pattern, while in the in-line direction (Fig 4-10(b)) the riser vibrates including a standing wave pattern and a traveling wave pattern as reported by Moe et al. [49]. It is worth noting that due to the limited number of the accelerometers, the experimental results tend to exhibit six curvature peaks, with two mid-span peaks coalescing as shown in Fig. 4-10(c). Moe et al. reported the excited 5th mode in the cross-flow direction, and this corresponds to the in-plane modal shape with six curvatures for an inclined curved cylinder by Srinil et al. [143]. Six curvatures are captured in the numerical model which is similar to the results obtained by Ma and Srinil [74]. Through this quantitative comparison of the amplitudes, it can be obtained that the numerical model can capture the VIV feature in good form, which demonstrates the effectiveness of the proposed numerical model.

In summary, although there are still some quantitative differences, the qualitative features are reasonably captured by the proposed numerical model. The improvement of model could involve further accounting for the effects of geometric nonlinearities and empirical parameters analyses supported by new experimental tests focusing on realistic catenary structures.

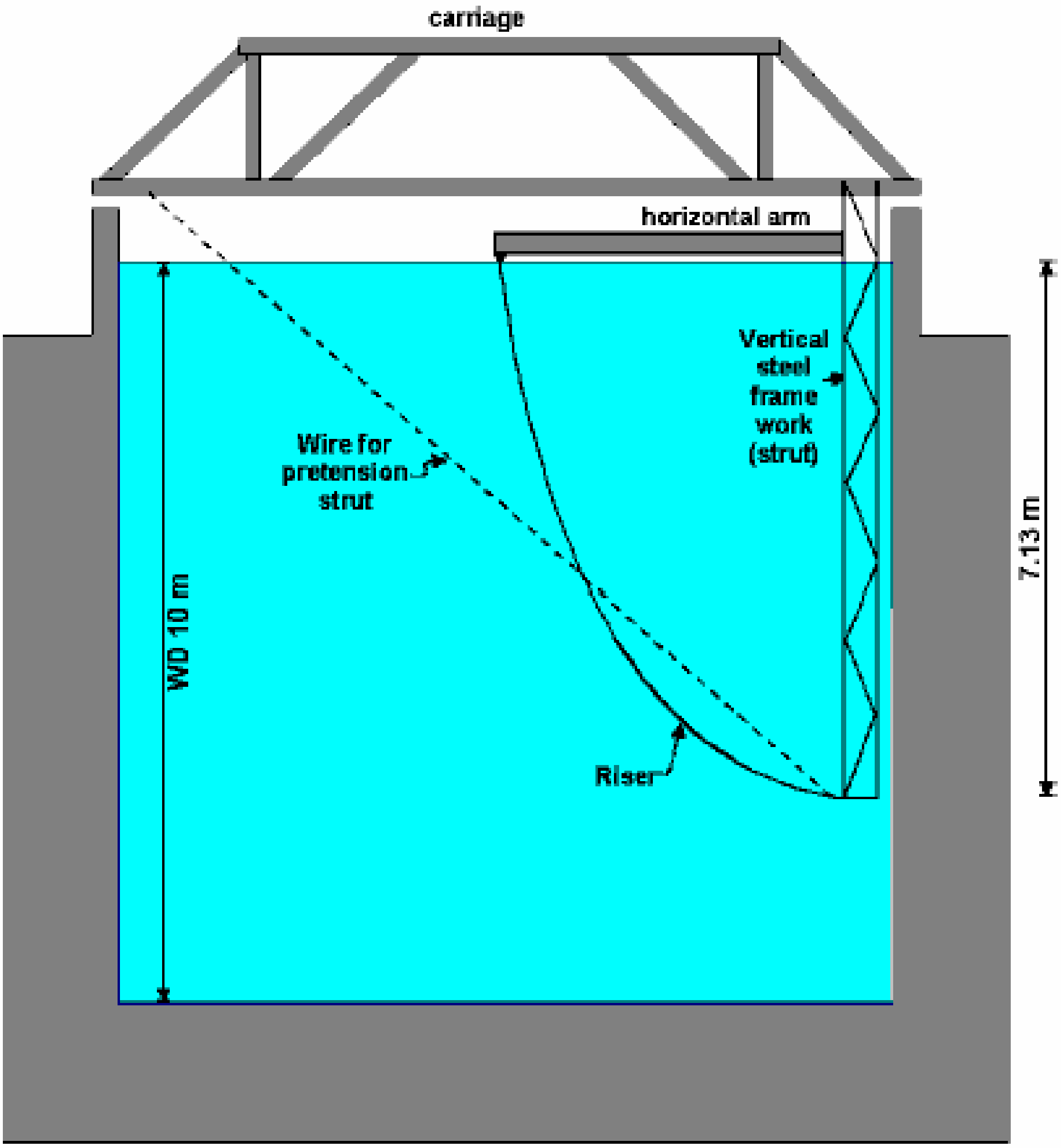


Fig.4-9 Sketch of the experiments (Moe et al, 2004) [49].

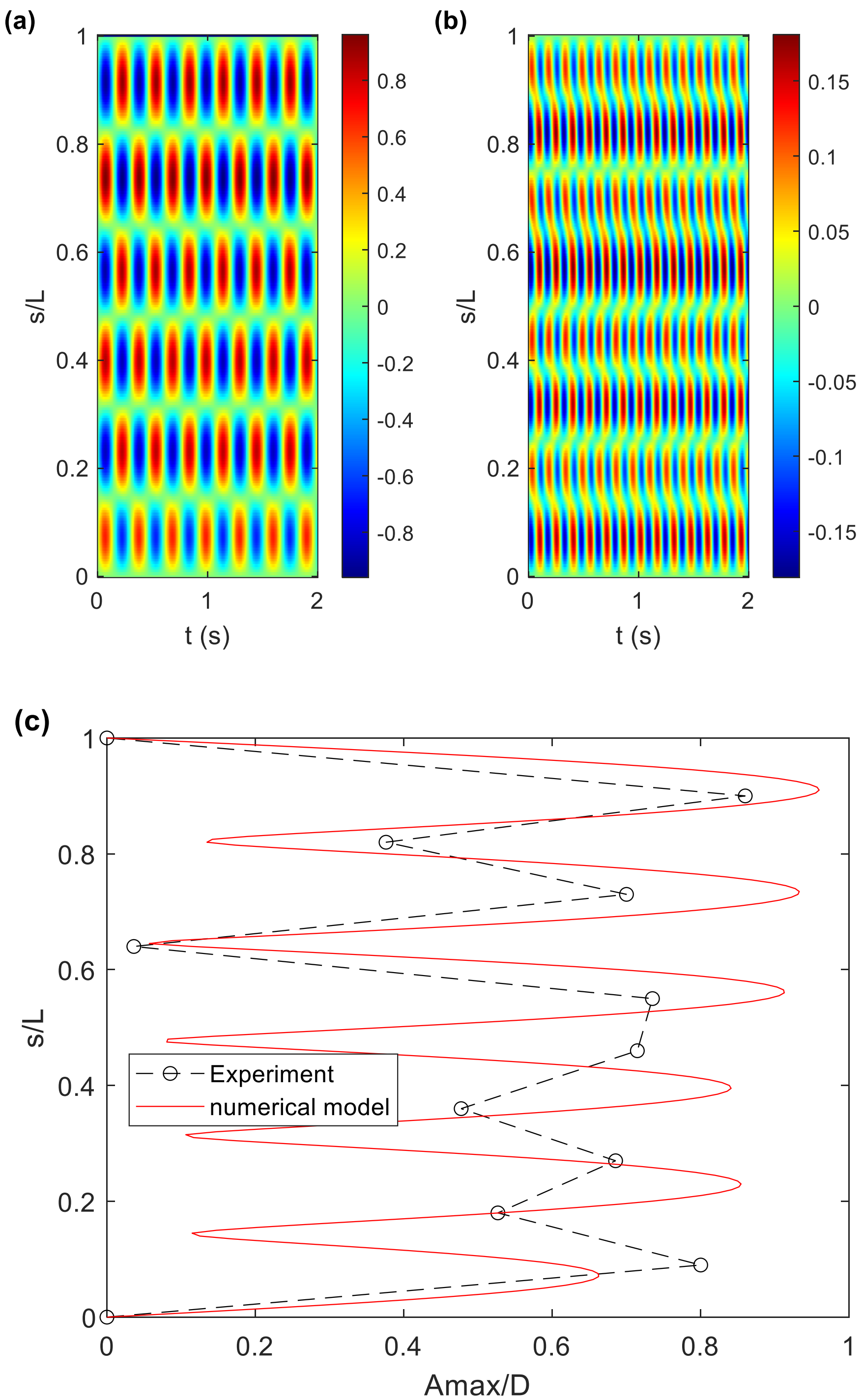


Fig.4-10 Contours of (a) cross-flow n and (b) in-line w responses in perpendicular flow based on experimental parameters of Moe et al. and (c) comparison of results by numerical model with experimental results (re-plot from Moe et al.).

## 4.5 Chapter conclusion

In this chapter, the focus is on refining the proposed numerical model introduced in Chapter 2.

First, a sensitivity analysis of the empirical parameters is conducted to assess their impact on the model's performance. To identify the optimal parameter values, an empirical parameters error equation is introduced, which quantifies the deviation between numerical predictions and experimental data. Next, the appropriate time step and spatial discretization segment are determined to ensure computational accuracy and efficiency. Finally, the numerical model is validated by comparing its predictions with experimental results reported in the literature, thereby assessing its reliability and effectiveness in capturing the desired phenomena.

# CHAPTER 5 Study and discussion for numerical and experimental results

## 5.1 Introduction

In this chapter, numerical prediction results and experimental results of the cable are compared. The initial static profile and local inclination angle of cable are discussed in Section 5.2. The response of vibrations of the cable is studied in Section 5.3, including the maximum vibration amplitudes, the maximum RMS vibration amplitudes, the spatial-temporal varying responses, the vibration frequencies and the motion trajectories of the cable. The response of tensions of the cable is studied in Section 5.4, including the time-history and amplitudes, the average, the maximum vibration amplitudes and the frequencies of tensions of the cable.

## 5.2 Initial static profile and local inclination angle of cable

The initial static profile at in-plane x-y coordinates and the associated local inclination angle variation along the arclength *s* of the flexible curved cable in experiment and numerical simulation are shown in Fig 4-1. In the initial state, the cable sags in the X-Y plane, and the cable profile is approximated by a classical hyperbolic function with a minimum bend radius a = 2.176m at $x = 0$ as shown in Fig 5-1(a). For the local inclination angle $\beta$ along the arclength *s*, the maximum $\beta = 32.4°$ is at the top end and the minimum $\beta = 0°$ is at the bottom end as shown in Fig 5-1(b). In addition, the spatially averaged chord inclination ($\beta = Y_H / X_H$) is about 17.1°. It can be seen that the initial static profile and the local inclination angle of cable in experiment and numerical simulation are nearly equal.

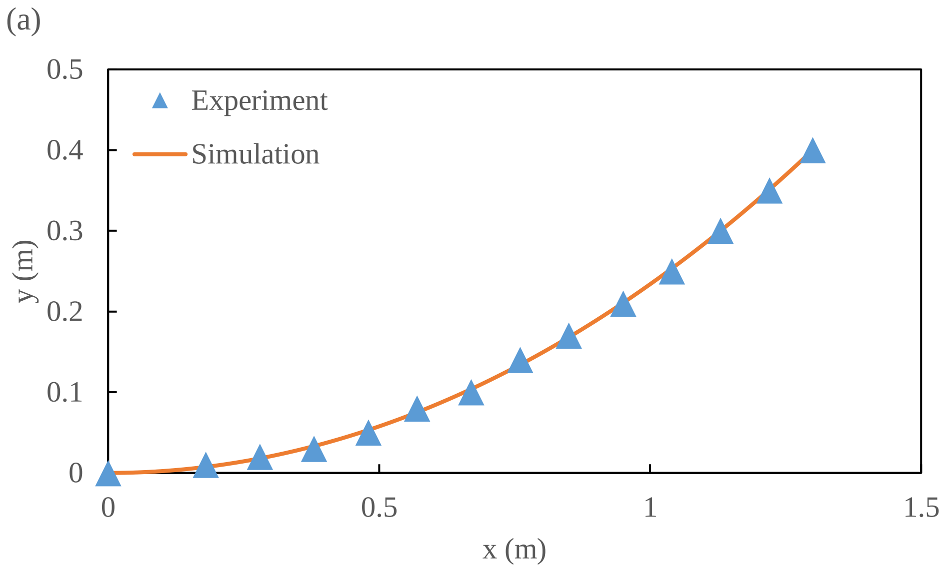


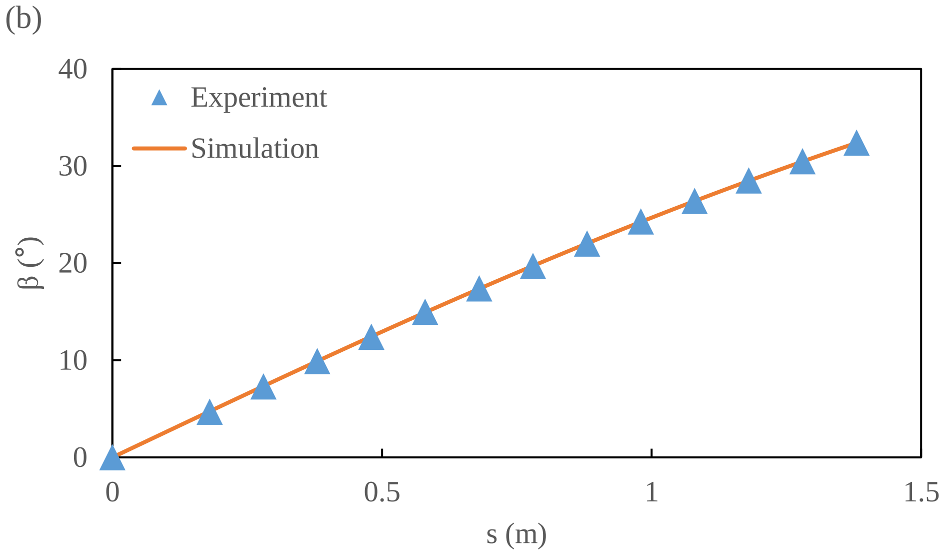


Fig.5-1 (a) Initial static profile at X - Y plane and (b) local inclination angle variation of the flexible curved cable along the arclength *s* in experiment and numerical simulation.

## 5.3 Response of vibrations of the cable

### 5.3.1 Maximum vibration amplitudes of the cable

The experimental displacements were obtained by extracting video data. The spatially maximum vibration amplitudes of the experimental and numerical results as a function of the flow velocity $U_0$ are compared in Fig 5-2 (Fig 5-2(a) shows the total vibration and Fig 5-2(b) (c) (d) show the discomposed vibration). For comparison, the mean offset of the cable from its initial position is removed during the data processing. It is worth noting that the vibration amplitude in w-direction at $U_0 = 0.6m/s$ cannot be properly extracted from the video data owing to the fact that the vibration frequencies are over the Nyquist sampling frequency.

As shown in Fig 5-2, the maximum vibration amplitudes as a function of the flow velocity $U_0$ record a very similar trend between experiment and simulation. At the first lock-in area ($U_0 < 0.36m/s$), the maximum vibration amplitude increases as the flow velocity $U_0$ increases and then decreases. It would be caused by the low mass ratio (m* = 2.0253) of the model. A similar result has been reported in [141]. At the second lock-in area ($0.36\mathrm{m/s} \leq U_0 < 0.6m/s$) the maximum vibration amplitude increases as the flow velocity $U_0$ increases, and the cross-flow (both u and v) vibration are greater than the in-line vibration. At $U_0 = 0.6m/s$, the vibration is out of the lock-in area, and cross-flow (both u and v) maximum vibration amplitude decreases dramatically. It can be seen that the maximum vibration in Y direction are always greater than the maximum vibration in X and Z direction under all the flow velocities. In addition, a saw-tooth pattern could be observed as the flow velocity $U_0$ increases. A similar phenomenon has been reported in the experiment using a flexible cylinder in [142]. Therefore, it can be obtained that the numerical model can properly capture the lock-in regimes, which is essential for VIV study.

From Fig 5-2, it can be found that the numerical results are greater than experimental results in most of the cases. One reason would be the limitation of the mark numbers in experiment so that the marks are not located at the maximum displacement. In addition, the empirical parameters can still be optimized.

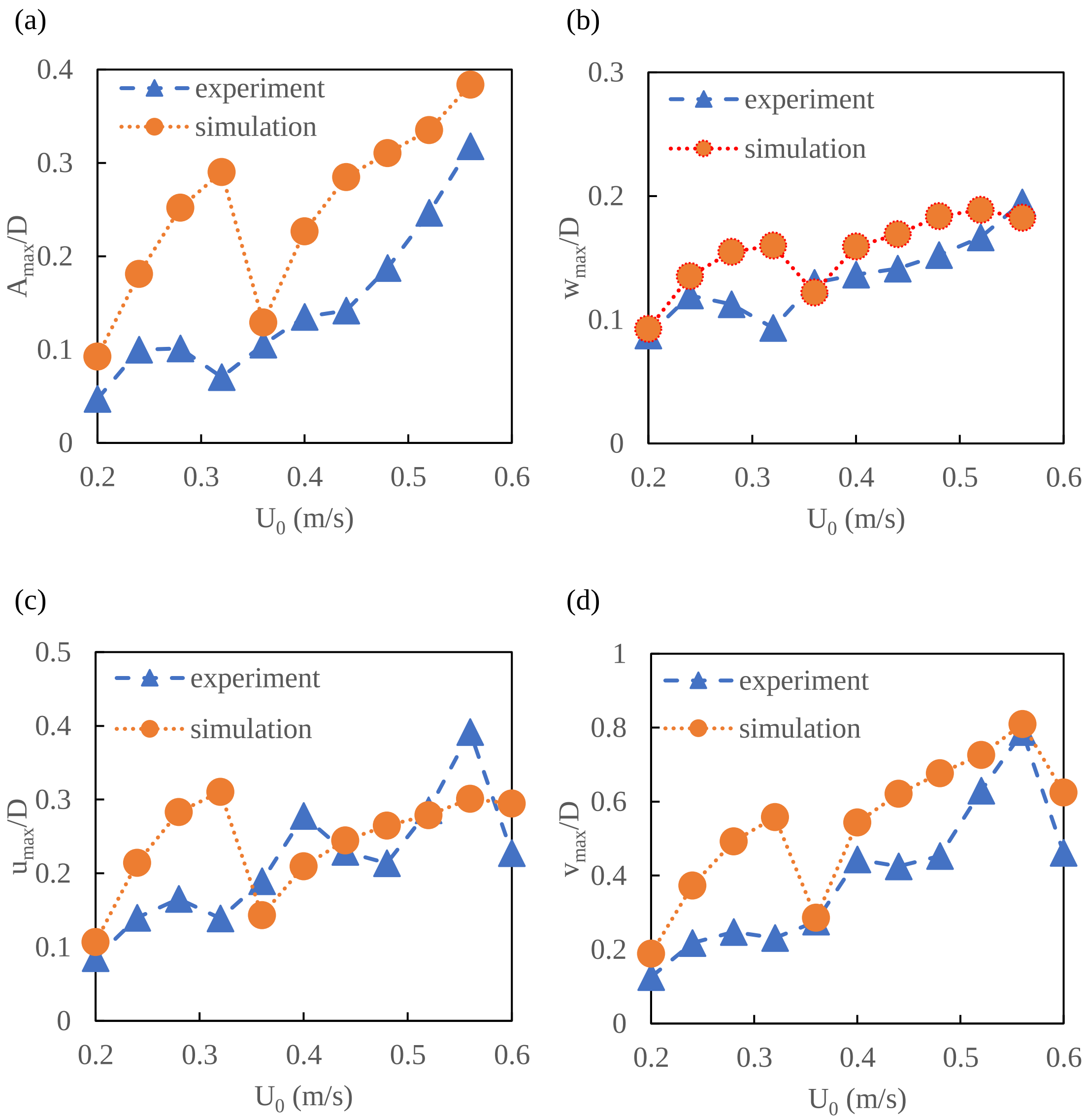


Fig.5-2 Comparison of the spatially maximum vibration amplitudes for experimental and numerical results with the flow velocity $\boldsymbol{U_0}$ (a) total vibration amplitudes; (b) in-line w vibration amplitudes; (c) cross-flow u vibration amplitudes; (d) cross-flow v vibration amplitudes.

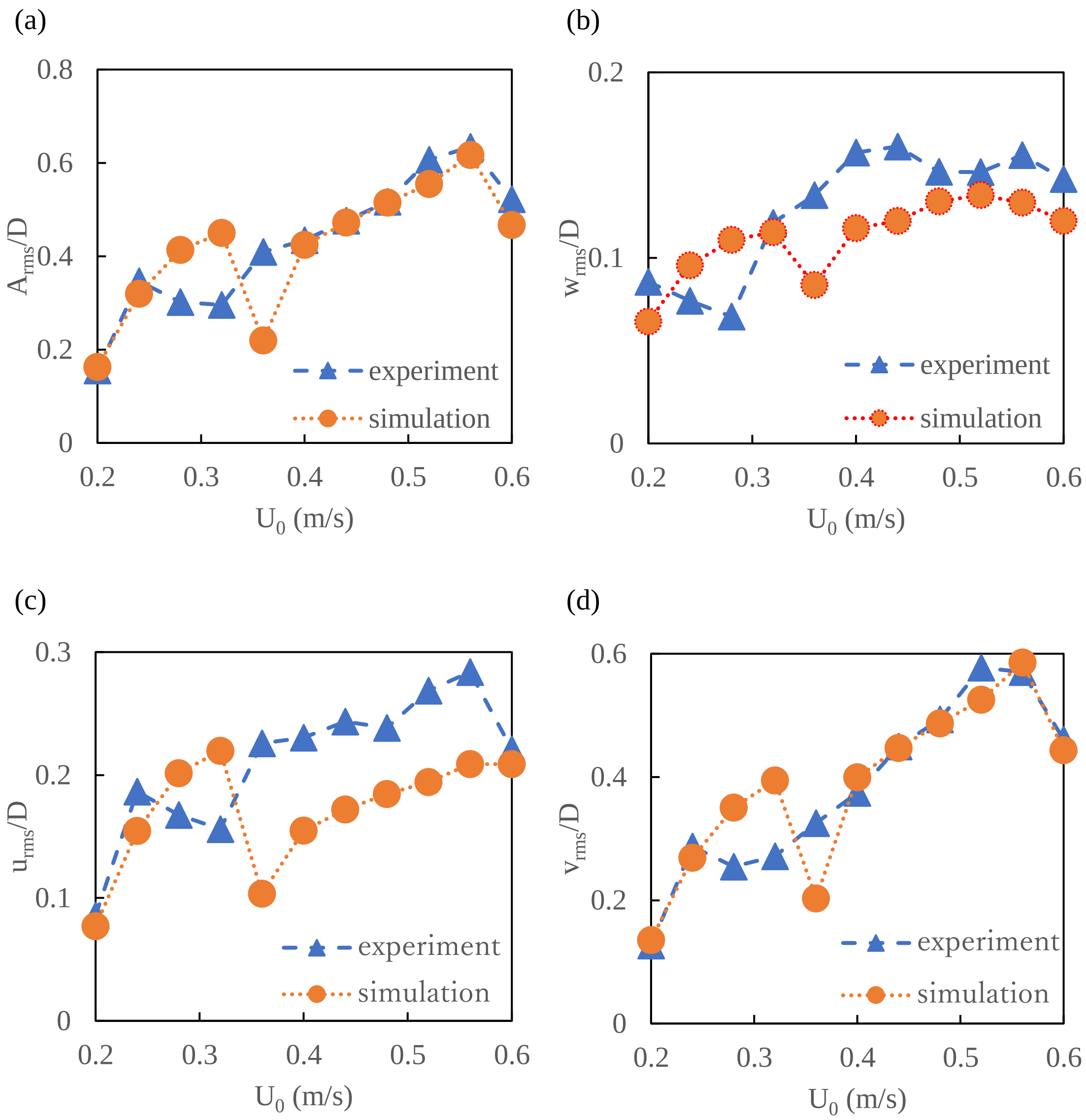


Fig.5-3 Comparison of the spatially maximum RMS vibration amplitudes for experimental and numerical results with the flow velocity $U_0$ (a) total RMS vibration amplitudes; (b) in-line w RMS vibration amplitudes; (c) cross-flow u RMS vibration amplitudes; (d) cross-flow v RMS vibration amplitudes.

### 5.3.2 Maximum RMS vibration amplitudes of the cable

The spatially maximum root-mean-squared (RMS) vibration amplitudes of the experimental and numerical results as a function of the flow velocity $U_0$ are compared in Fig 5-3 (Fig. 5-3(a) shows the total RMS vibration and Fig. 5-3(b) (c) (d) show the discomposed RMS vibration). It is found that as the flow velocity $U_0$ increases, the maximum and RMS vibration amplitudes vary similarly between experiment and simulation as the flow velocity increases as shown in Fig. 5-2 and Fig. 5-3. The maximum RMS values in Y direction are always greater than the values in X direction under all the flow velocities. The maximum RMS vibration amplitude varies as a V-shape with the increase of flow velocity. Overall, the numerical results could capture the maximum and maximum RMS vibration amplitude in good form.

### 5.3.3 Spatial-temporal varying responses of the cable

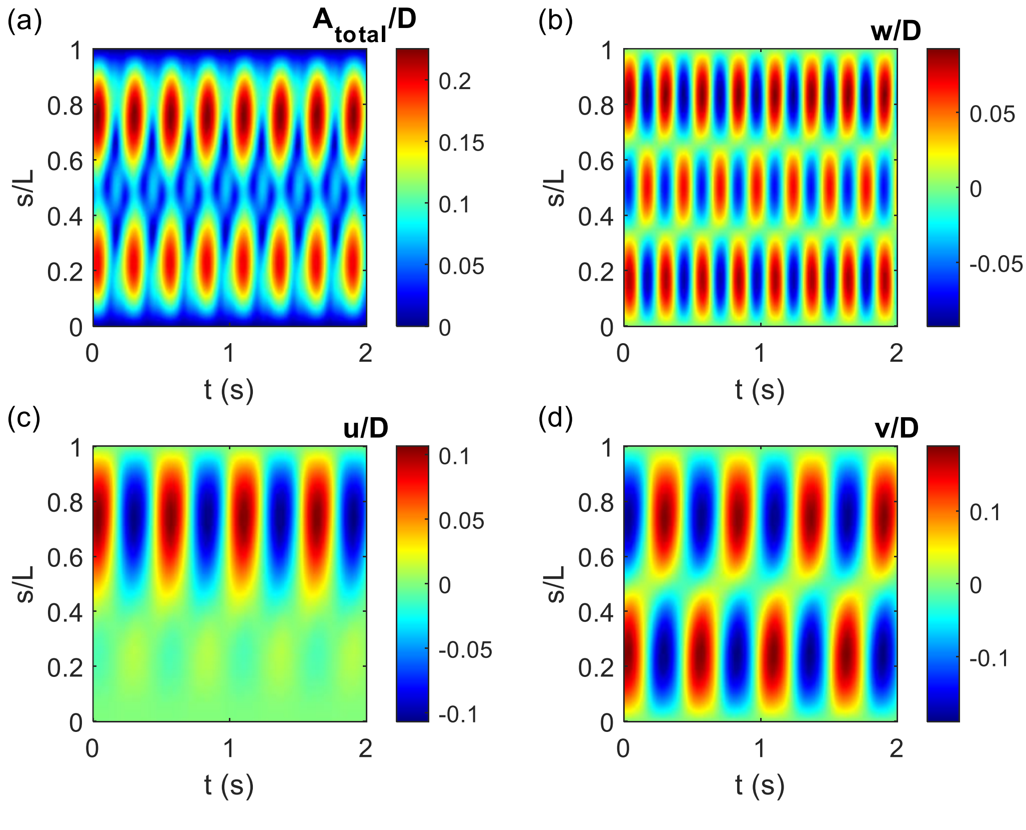


Fig.5-4 Spatial-temporal varying responses under $U_0 = 0.20\ \mathrm{m/s}$ in the (a) total direction; (b) in-line w direction; (c) cross-flow u direction; (d) cross-flow v direction.

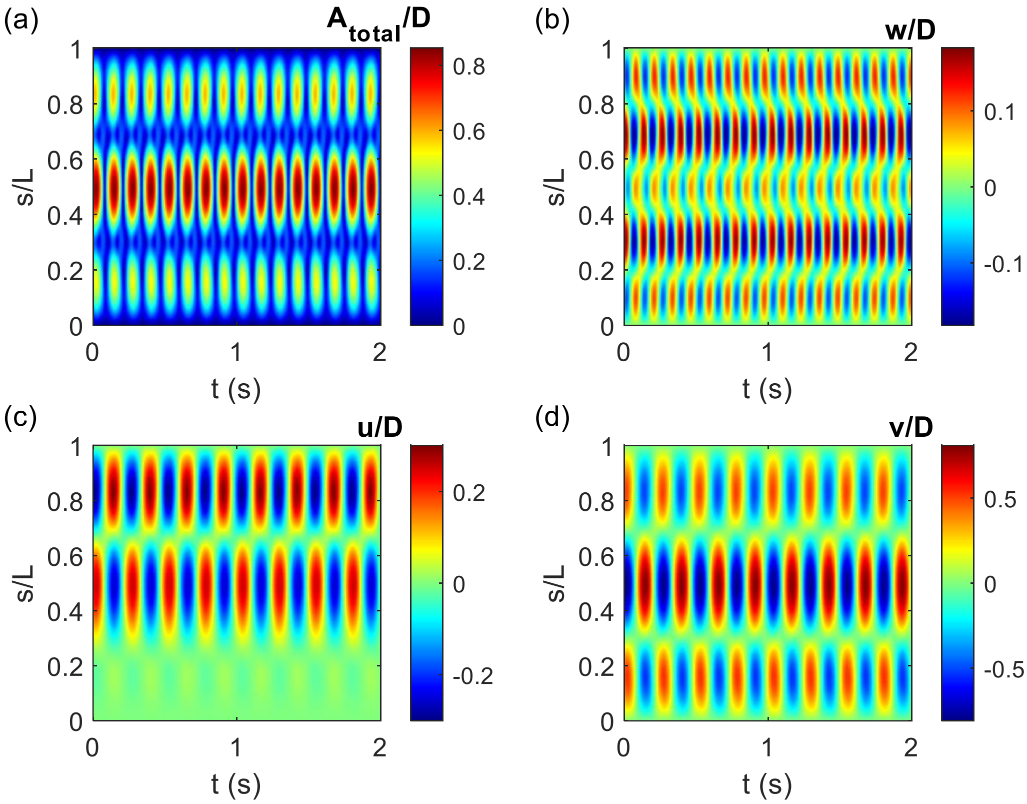


Fig.5-5 Spatial-temporal varying responses under $U_0 = 0.56 \text{ m/s}$ in the (a) total direction; (b) in-line w direction; (c) cross-flow u direction; (d) cross-flow v direction.

The spatial-temporal varying responses of the numerical prediction results of the cable at $U_0 = 0.20 \text{ m/s}$ and $U_0 = 0.56 \text{ m/s}$ are plotted in Fig 5-4 and Fig 5-5. It is found that at $U_0 = 0.20 \text{ m/s}$ the cable vibrates with a standing wave pattern in the all directions (Fig 5-4). At $U_0 = 0.56 \text{ m/s}$, the cable vibrates with a standing wave pattern in the cross-flow direction (Fig 5-5(c) (d)) and a traveling wave pattern in the in-line direction (Fig 5-5(b)). For the total vibration Amax/D, it always appears as a standing wave.

As the flow velocity $U_0$ increases, in the cross-flow direction (u and v) the cable constantly vibrates with a standing wave pattern, as a contrast in the in-line direction (w) the cable gradually vibrates from a standing wave pattern to a traveling wave pattern. The cable undergoes a transition from standing to traveling waves as the flow velocity $U_0$ increases in the in-line direction. In the cross-flow direction, the maximum response is greater than that in the in-line direction. The spatially maximum response is in the vertical v direction ($v_{max}/D = 0.625$) in Fig 5-5(d), despite w response shows a greater number of modal curvatures associated with a high-order excited mode.

### 5.3.4 Vibration frequencies of the cable

The cable vibration frequencies, which are calculated by Fast Fourier Transform (FFT) method, are also compared as shown in Fig 5-6. Both the cross-flow and the in-line vibration frequencies increase as the flow velocity $U_0$ increases, and the in-line vibration frequencies are approximate twice as large as the cross-flow vibration frequencies. Under the condition of $U_0 = 0.36\, m/s$, the cross-flow vibration frequency ratio (which is the ratio of vibration frequency *f* to natural frequency $f_n$ of the cable) is close to 1, the cable goes into lock-in range. In addition, it is observed that the cross-flow vibration frequencies in X direction and in Y direction are always equal under all the flow velocities both experimental and numerical results.

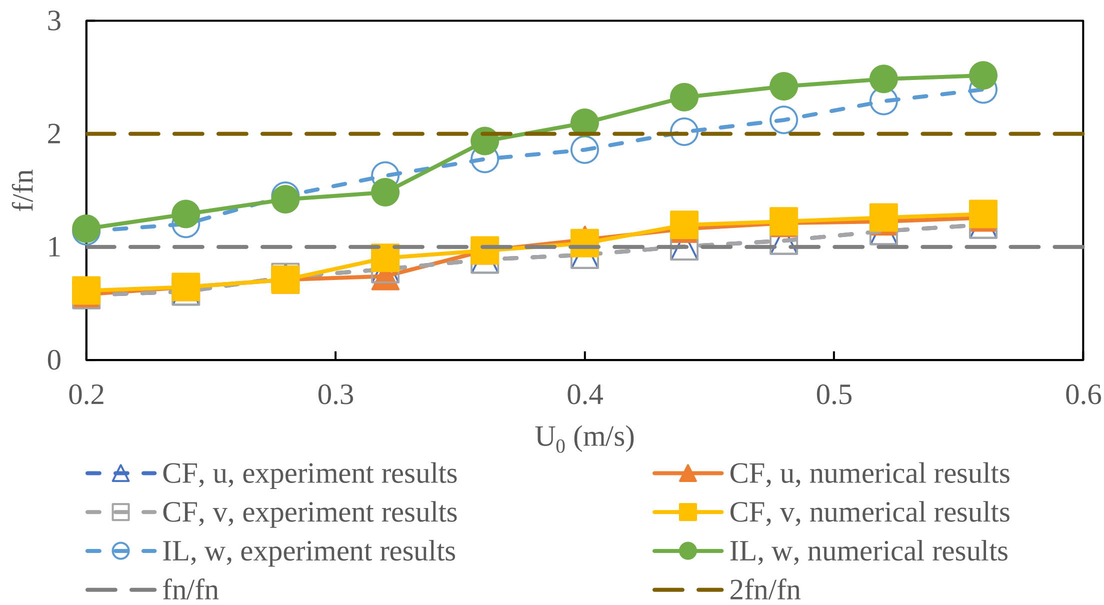


Fig.5-6 Comparison of the frequency ratio of cable as a function of the flow velocity $U_0$ in the experimental and numerical results.

In association with the spatial-temporal varying VIV responses depicted in Fig 5-4 and Fig 5-5, the vibration patterns of the cable under $U_0 = 0.20\ \mathrm{m/s}$ and $U_0 = 0.56\ \mathrm{m/s}$ by simulation are shown in Fig 5-7 and Fig 5-8, respectively. For all the u, v, and w components, the spatial single-frequency responses are identical to Fig 5-6. The amplitudes of the cross-flow vertical responses v are greater than those in X and Z directions. In addition, the resonance with 2:1 ratio of in-line (7.8 Hz in Fig 5-8(b)) to cross-flow (3.9 Hz in Fig 5-8(c) and (d)) is shown in Fig 5-8. Overall, the numerical results could capture the vibration frequencies in good form.

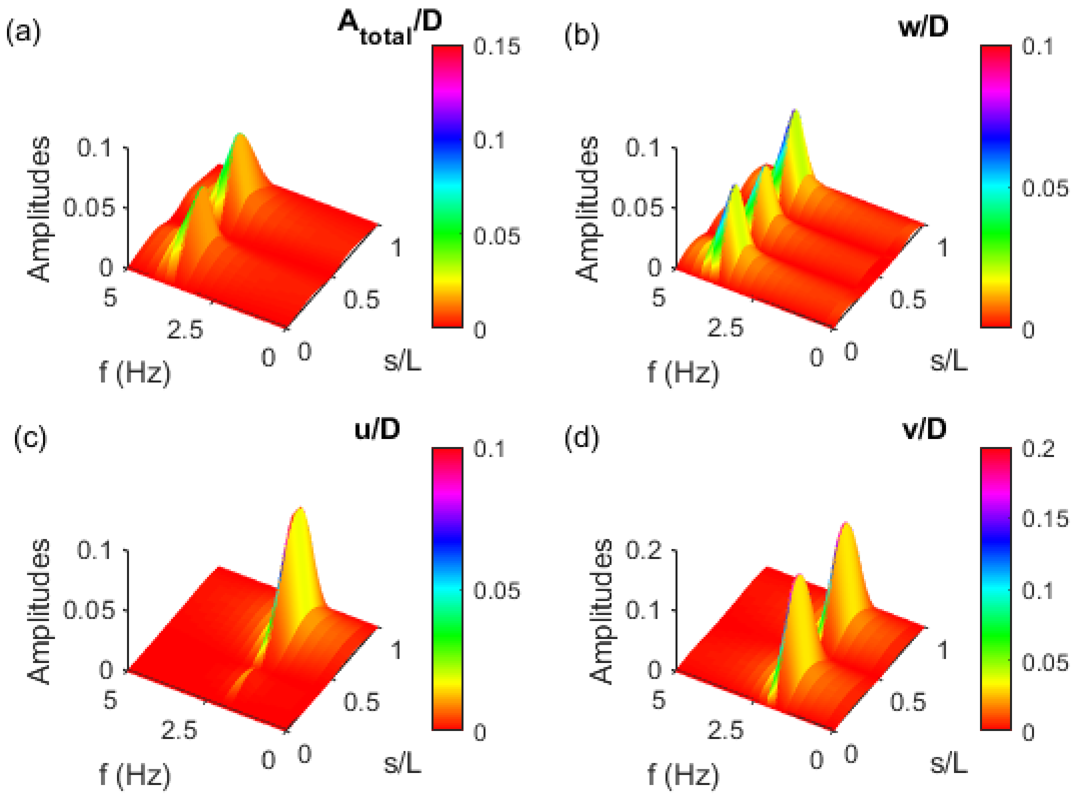


Fig.5-7 Three-dimensional vibration pattern of cable under $U_0 = 0.20\, m/s$ by numerical prediction in the (a) total direction; (b) in-line w direction; (c) cross-flow u direction; (d) cross-flow v direction.

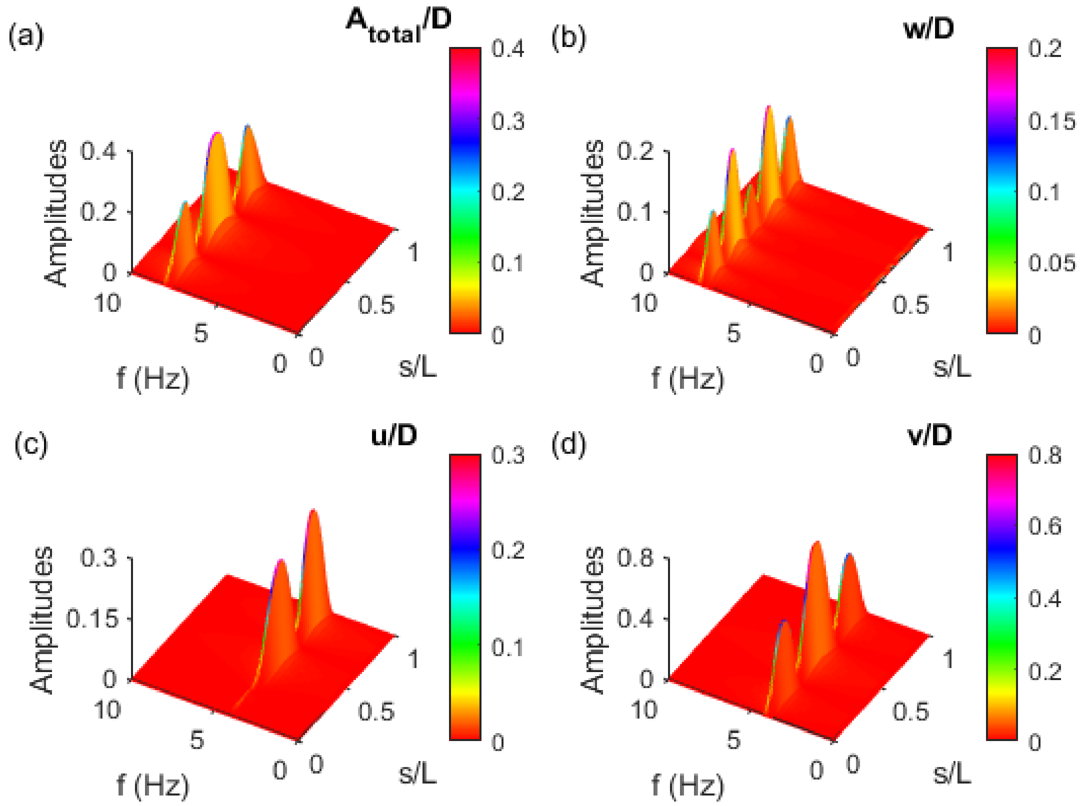


Fig.5-8 Three-dimensional vibration pattern of cable under $U_0 = 0.56\,m/s$ by numerical prediction in the (a) total direction; (b) in-line w direction; (c) cross-flow u direction; (d) cross-flow v direction.

### 5.3.5 Motion trajectories of the cable

The accuracy of the experimental data is insufficient to plot the in-line and cross-flow motion trajectories accurately. Consequently, these aspects are discussed and analyzed through numerical results.

Motion trajectories t selected spanwise locations (s/L = 0.1–0.9 with an increment of 0.1) are illustrated in Fig 5-9 for flow velocities $U_0 = 0.20\ \mathrm{m/s}$ and $U_0 = 0.56\ \mathrm{m/s}$, respectively. The in-line and cross-flow motion trajectories are plotted based on the oscillatory components and scaled up for visibility. To determine the phase differences that characterize trajectory shapes, considering that the vibration results in three directions are close to periodic sinusoids, the synchronized in-line (w) and cross-flow (u, v) oscillations with a dual 2:1 resonance can be expressed as follows:

$$\omega = \omega_0 \sin(2\omega_0 t + \theta_\omega)\,, u = u_0 \sin(\omega_0 t + \theta_u)\,, v = v_0 \sin(\omega_0 t + \theta_v)\,, \tag{40}$$

where $u_0$, $v_0$, and $w_0$ are the amplitudes, $\omega_0$ is the dominant frequency ($\omega_0 = 2\pi f_0$), and $\theta_u$, $\theta_v$, and $\theta_\omega$ are the associated phases. According to the global axes, the in-line and cross-flow phase differences are defined as:

$$\theta_{zx} = \theta_\omega - 2\theta_u, \qquad \theta_{zy} = \theta_\omega - 2\theta_v. \tag{41}$$

In accordance with Jauvtis and Williamson [144], the counter-clockwise (clockwise) motion corresponds to phase differences in the range of 270° – 90° (90° – 270°), with the sectional cross-flow response moving upstream (downstream) when reaching its maxima [145]. It is worth mentioning that the phase differences versus the flow direction, determined according to Equation (41), are identified only for repeatable trajectories that satisfy Equation (40).

At low flow velocity $U_0 = 0.20\ \mathrm{m/s}$ and high flow velocity $U_0 = 0.56\ \mathrm{m/s}$, it can be seen that most in-line and cross-flow motion trajectories at each location exhibit repeatable figure-of-eight shapes due to the 2:1 resonance discussed in Section 5.3.4. Additionally, most trajectories show counter-clockwise trajectories, which favor large-amplitude VIV [146]. The counter-clockwise trajectories tend to result in larger amplitude oscillations, exhibiting the significant impact of phase differences on the vibration characteristics of the cable.

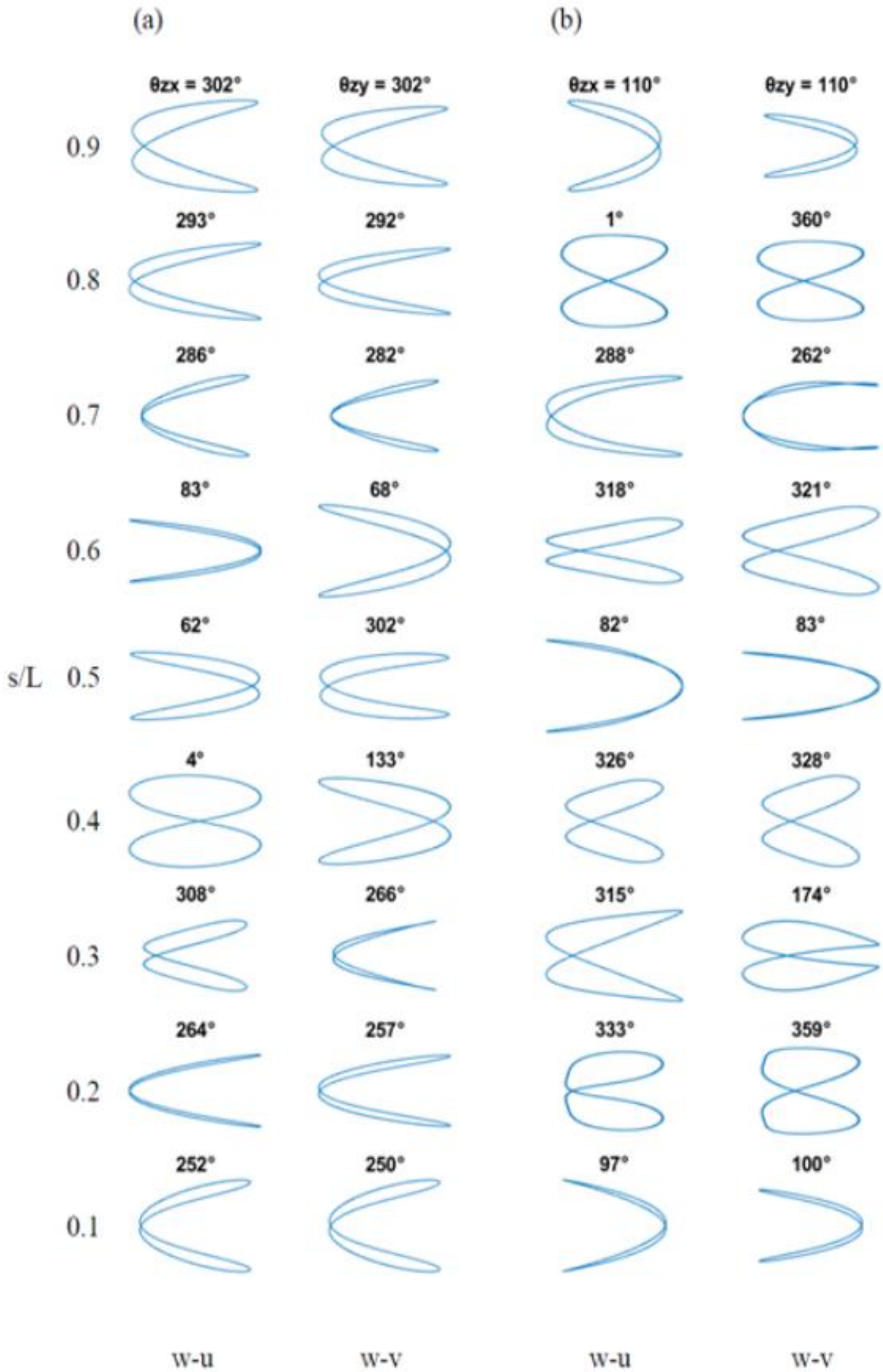


Fig.5-9 Spatial variations of trajectories of cable under (a) $U_0 = 0.20\,m/s$ and (b) $U_0 = 0.56\,m/s$.

## 5.4 Response of tensions of the cable

### 5.4.1 Time-history and amplitudes of tensions of the cable

The tension at the two ends of the cable in the experiment under $U_0 = 0.56\,m/s$ and the associated frequency-domain analysis results are shown in Fig.5-10. Since the tension measured by the load cells is reset at the beginning of each experiment to reduce the sensor drift during long-term measurement, the initial tension is subtracted from the numerical results for ease of comparison. From Fig.5-10, it is observed that the tension at the two ends almost vibrates synchronously, and the vibration frequency is almost equal. The tension at the top end are slightly greater than the tension at the bottom.

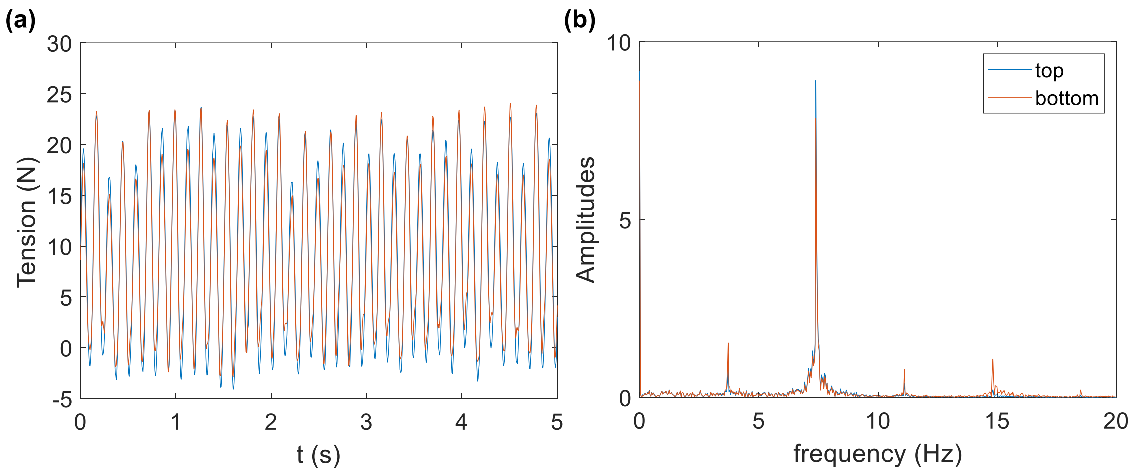


Fig.5-10 Comparison of time-history and amplitudes of tension at both ends of the cable in the experimental results under $U_0 = 0.56\,m/s$.

The comparison of time-history and amplitudes of tension at both ends of the cable in the experimental and numerical results under $U_0 = 0.56\,m/s$ is shown in Fig 5-11. It is noteworthy that, in numerical results the tensions calculated by Equations (9-11) are always positive. For ease of comparison, the minimum tension value is subtracted from the results, so the tension is always greater than or equal to 0. It could be observed that the time-history of tension in numerical results is smoother than that in the experimental results, and the tension frequency can be well captured.

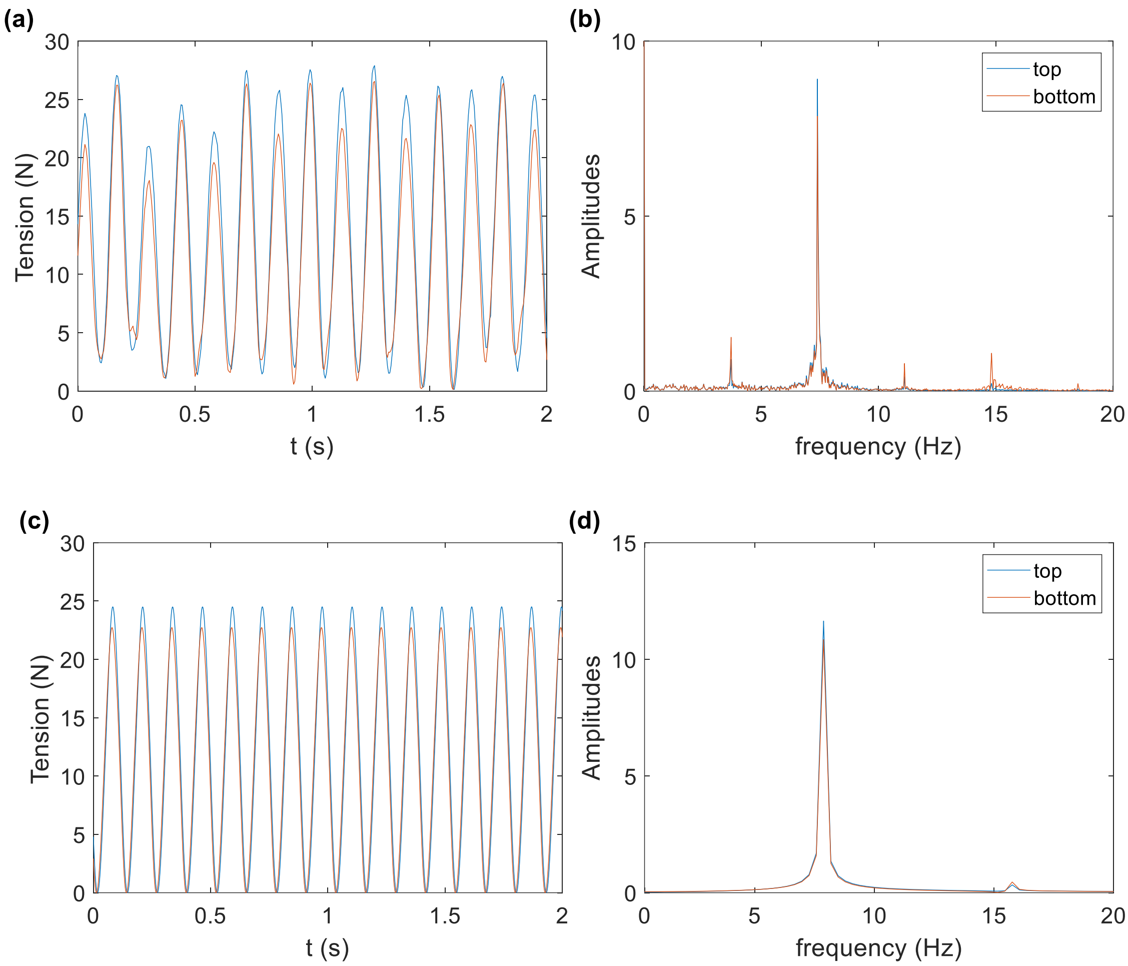


Fig.5-11 Comparison of time-history and amplitudes of tension at both ends of the cable in the experimental (a, b) and numerical results (c, d) under $U_0 = 0.56\,m/s$.

### 5.4.2 Average of tensions of the cable

As shown in Fig 5-12, the time-averaged tension as a function of the flow velocity $U_0$ is compared. It could be observed that as the flow velocity increases, the average tension increases at both the top and bottom ends of the cable. At the flow velocity $U_0 =$

$0.2\,m/s$, the time-averaged tension at the top end in the experiment is approximately 0 N. The tension increases to 13.4 N at $U_0 = 0.56\,m/s$, which is about 1.6 times more than the initial tension. For calculating exact tension or considering fatigue analysis about tension, the great change of average of tension of cable has to be considered in numerical simulation. On the other hand, from the tendency of average value of tension, as the flow velocity increases continuously, the effect of spatial-temporal axially varying tensions on dynamic response of the geometrically nonlinear structures should be considered.

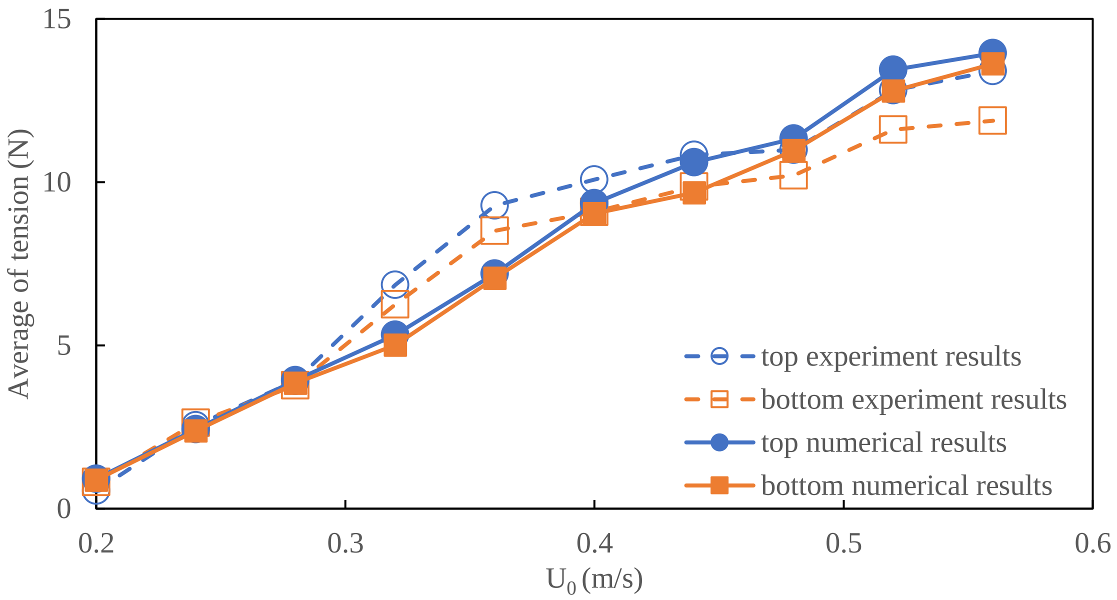


Fig.5- 12 Comparison of the time-average values of tension at both ends of the cable.

### 5.4.3 Maximum vibration amplitudes of tensions of the cable

As shown in Fig 5-13, the maximum vibration amplitudes of the tension at the two ends of the cable are compared. It is found that as the flow velocity $U_0$ increases, the maximum vibration amplitudes and the time-average values of the tension record a very similar behavior. In numerical results, the tensions calculated by Equation (9-11) are sine wave signals. The vibrations of the tension are approximately equal to the average values of tension as shown in the Fig 5-12 and Fig 5-13. As a contrast, in experiment results, the values of tensions are not perfect as shown in the Fig 5-11(a), and the maximum vibration amplitudes of the tension by FFT in experiment results are less than the average values of tension.

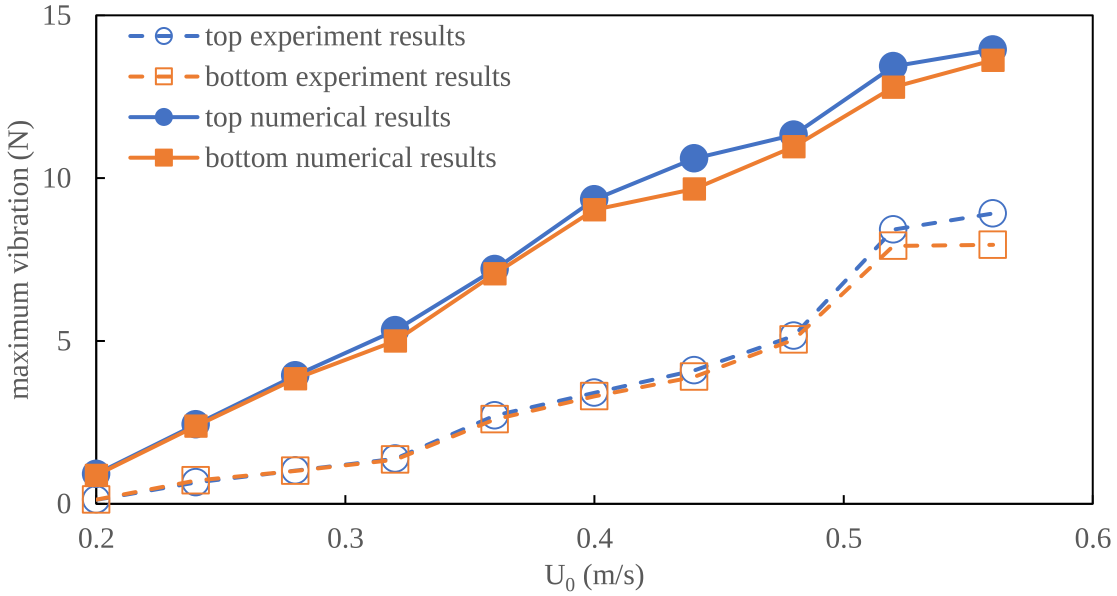


Fig.5-13 Comparison of the maximum vibration amplitudes of tension at both ends of the cable.

### 5.4.4 Frequency of tensions of the cable

The frequencies of the tension at the two ends of the cable are compared with each other in Fig 5-14. It could be observed that the frequency of tension increases gradually as the flow velocity $U_0$ increases. Compared to the cable vibration frequencies shown in Fig 5-6, the tension frequencies are roughly equal to the in-line vibration frequencies. The top end tension frequencies and the bottom end tension frequencies are always equal under all the flow velocities. Therefore, the numerical model could capture the tension characteristic from the comparison.

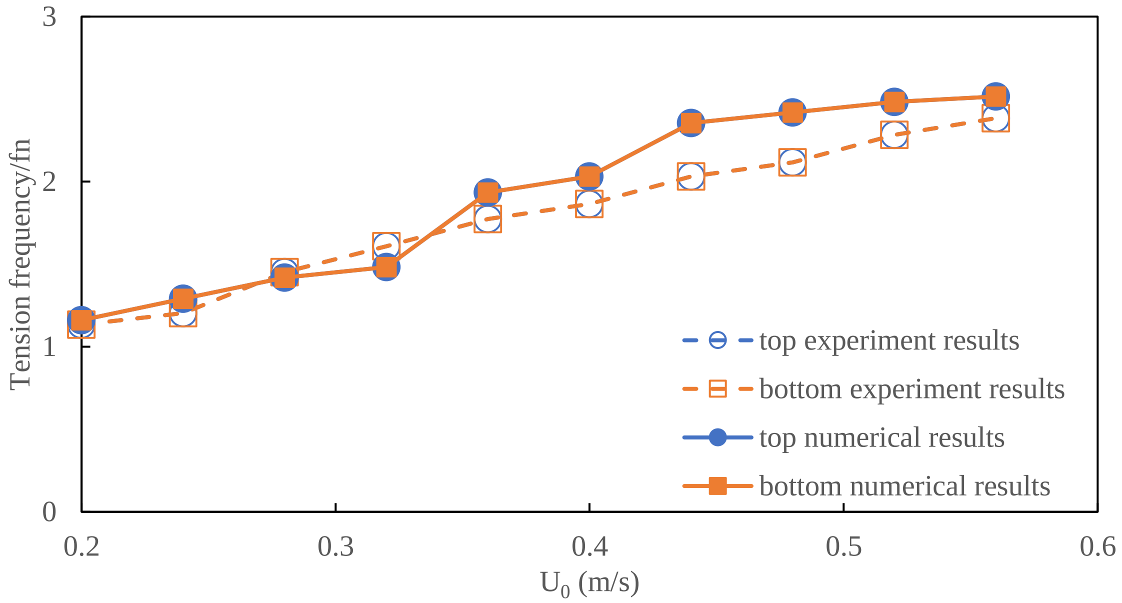


Fig.5-14 Comparison of the tension frequency at both ends of the cable.

## 5.5 Chapter conclusion

In this chapter, the single van der Pol wake oscillator model, which uses only one wake oscillator to simulate coupled in-line and cross-flow vibration and considers the cable catenary profile, has been applied to prediction of the response of vibrations and axial tensions of a long catenary cable in a perpendicular flow. An experiment on a submarine cable model has been carried out for validation of the proposed numerical model. Numerical results and experimental measurements are compared in perpendicular flow, including the initial static profile and local inclination angle, the maximum vibration amplitudes, the maximum RMS vibration amplitudes, the spatial-temporal varying responses, the vibration frequencies and the motion trajectories of the cable, the time-history and amplitudes, the average, the maximum vibration amplitudes and the frequencies of tensions of the cable. Numerical simulations by the proposed numerical model with properly selected parameters have demonstrated that the vibration frequency and the axial tension can be well predicted, and the variation of the vibration amplitudes can also be properly captured.

The main conclusions obtained from this study are as follows.

(1) The initial static profile and the local inclination angle of cable in experiment and numerical simulation are nearly equal.

(2) The lock-in phenomenon found in the experiment can be reproduced by the proposed numerical model. Two lock-in area can be found as the flow velocity $U_0$ increases. The spatially maximum vibration amplitudes and maximum RMS vibration amplitudes exhibit similar trends in three directions with the increase of the velocity $U_0$. The variation of maximum amplitude varies as a V-shape.

(3) As the flow velocity $U_0$ increases, in the cross-flow direction (u and v) the cable constantly vibrates with a standing wave pattern, as a contrast in the in-line direction (w) the cable gradually vibrates from a standing wave pattern to a traveling wave pattern.

(4) The cross-flow vibration frequencies in the X and Y direction are the same for all the flow velocities. Moreover, the cross-flow and in-line vibration frequency increase with the flow velocity $U_0$, while the in-line vibration frequency is nearly twice as the cross-flow vibration frequency.

(5) At low flow velocity $U_0 = 0.20\, m/s$ and high flow velocity $U_0 = 0.56\, m/s$, most motion trajectories show repeatable 8 shapes and counter-clockwise trajectories which favor large-amplitude VIV.

(6) The phase and frequency of the axial tension at both the top and bottom ends of the cable are almost same. As the flow velocity $U_0$ increases, both the average tension and the vibration frequency increase. The frequency of tension variation is roughly in line with the in-line cable vibration frequency. At $U_0 = 0.56\, m/s$, the top average tension can be more than 1.6 times of the initial tension.

# CHAPTER 6 VIV suppression effectiveness of vibration dampers

## 6.1 Introduction

As described in chapter 1, compared to a vertical riser, there is limited research on passive suppression devices for curved flexible cables, and further exploration is needed to understand the effectiveness and mechanisms of these suppression devices on the cable. In this chapter, the VIV suppression effectiveness of the vibration dampers installed on the cable is investigated and studied.

The experiment setup on a submarine cable model with vibration dampers is described in Section 6.2. For two experiments of the cable with vibration dampers and the cable without vibration dampers, the response of vibrations is studied in Section 6.3, including the maximum vibration amplitudes, the maximum RMS vibration amplitudes, the time-averaged in-line displacements and the vibration frequencies. The response of tensions is studied in Section 6.4, including the time-history and amplitudes, the average, the maximum vibration amplitudes and the frequencies of tensions.

## 6.2 Experimental setup for the cable with vibration dampers

When an overhead transmission cable is subjected to the wind, the vortex shedding around the cable may be induced, which in turn affects the flow field around the cable and leads to oscillatory vibrations. The vibration manifests as a sinusoidal loop across the span, with a magnitude ranging from 20 to 50 mm and a high frequency from 50 to 100 Hz, which may result in the conductor breakdown from supports and clamps [147]. To mitigate these issues, vibration dampers are employed. The primary role of the vibration dampers is to absorb vibrational energy and prevent oscillations. A type of stock-bridge damper is used for averting vibrations as shown in Fig 6-1. In this design, a stranded cable, typically 0.3 to 0.50 m long, features two hollow weights attached at either end, clamped to the cable conductor. These weights, constructed from galvanized iron, are affixed to the conductor using a single bolt. The inclusion of stock-bridge dampers on the transmission cable effectively dampens cable vibrations [148-163].

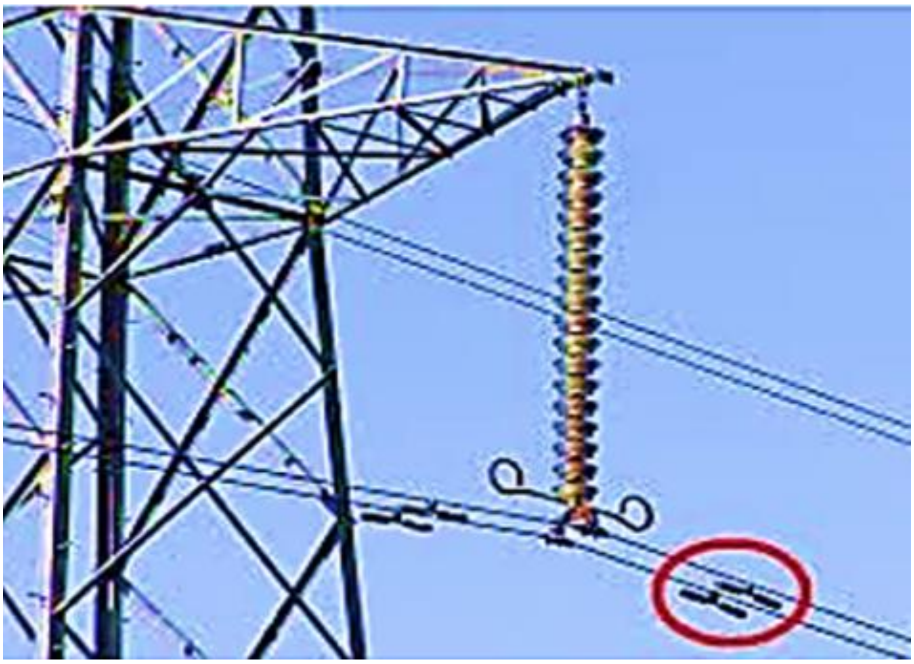

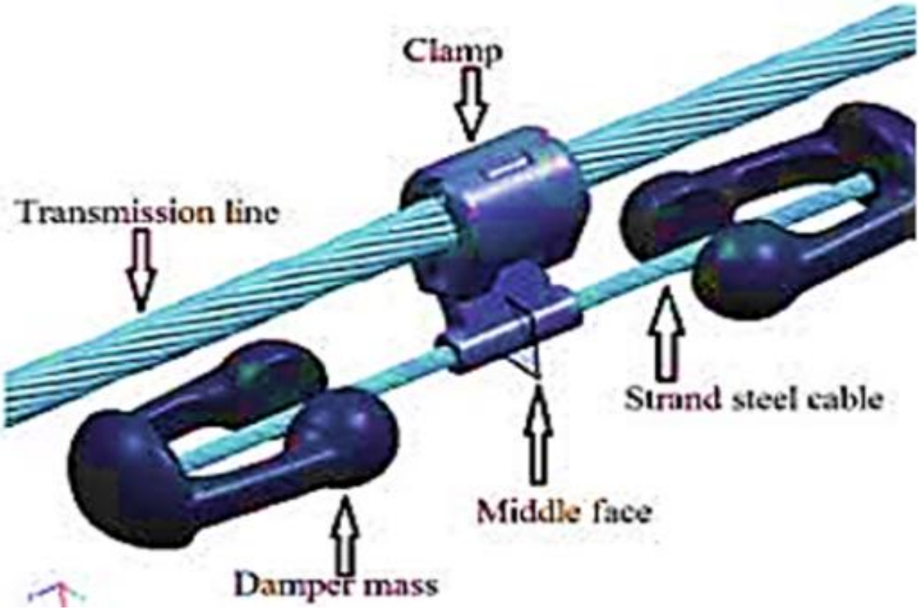


Fig.6-1 Vibration damper used in overhead transmission cables in the air [164].

The vibration dampers used in this study are analogous to the stock-bridge dampers employed in overhead transmission cables in the air. As shown in Fig 6-2, the vibration damper made by 3D Printing is made of plastic material with a very light weight (approximately 10 g). The vibration damper is total 0.07 m long with two hollow flat cylinders at either end, and is clamped to the cable using two bolts. Finally, four vibration dampers are installed on the cable. Considering the vibration damper used in an overhead transmission cable is installed near the end, in the experiment the arc length from the origin is respectively 0.22 m, 0.44 m, 0.95 m and 1.19 m, as shown in Fig 6-3 and Fig 6-4. The other settings of experiment are consistent with those without vibration dampers in Chapter 3. It is worth mentioning that since the vibration damper has a light weight (approximately 10 g), the initial static profile and local inclination angle of the cable with vibration dampers are almost constant compared to the cable without vibration dampers.

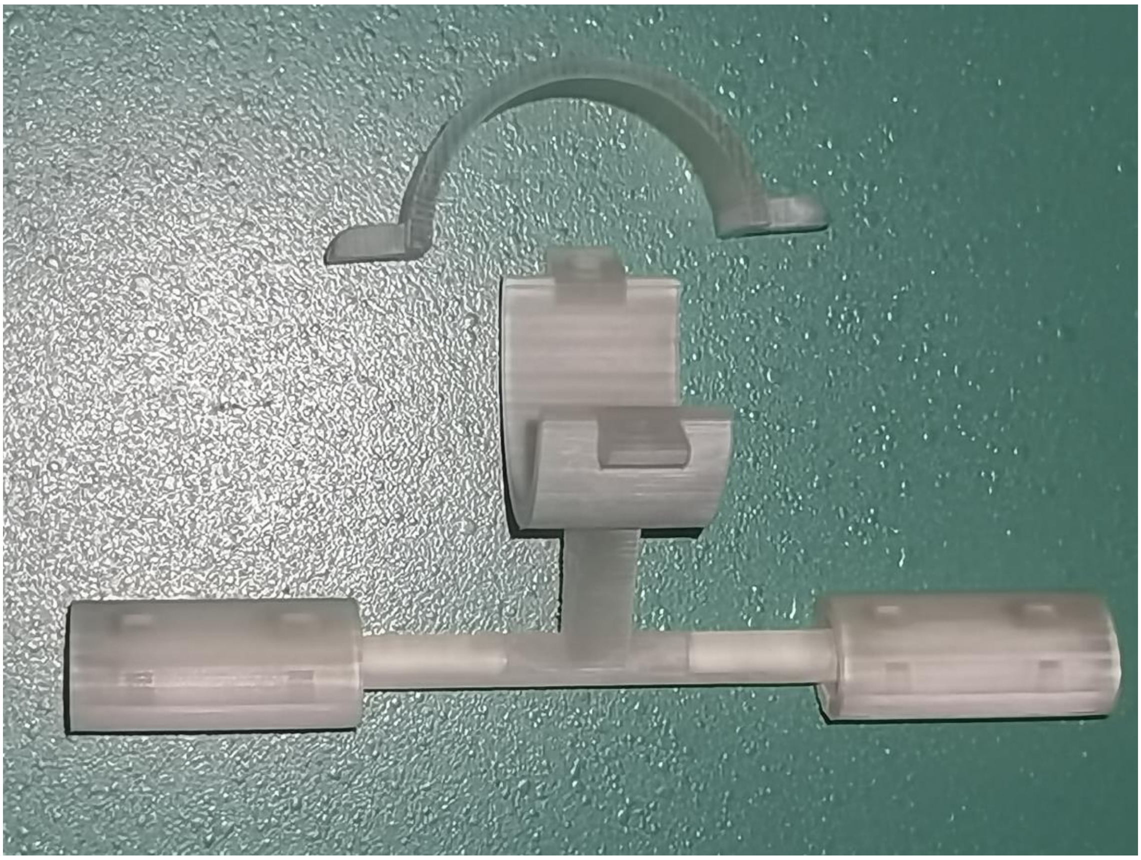

Fig.6-2 Vibration damper in this study.

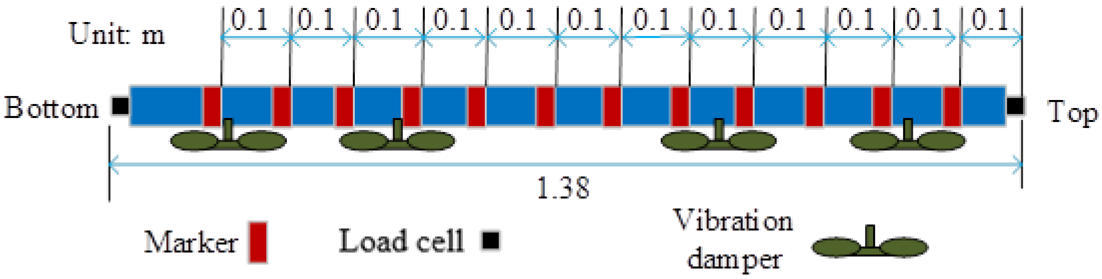


Fig.6-3 Schematic drawing of the cable model with the vibration dampers.

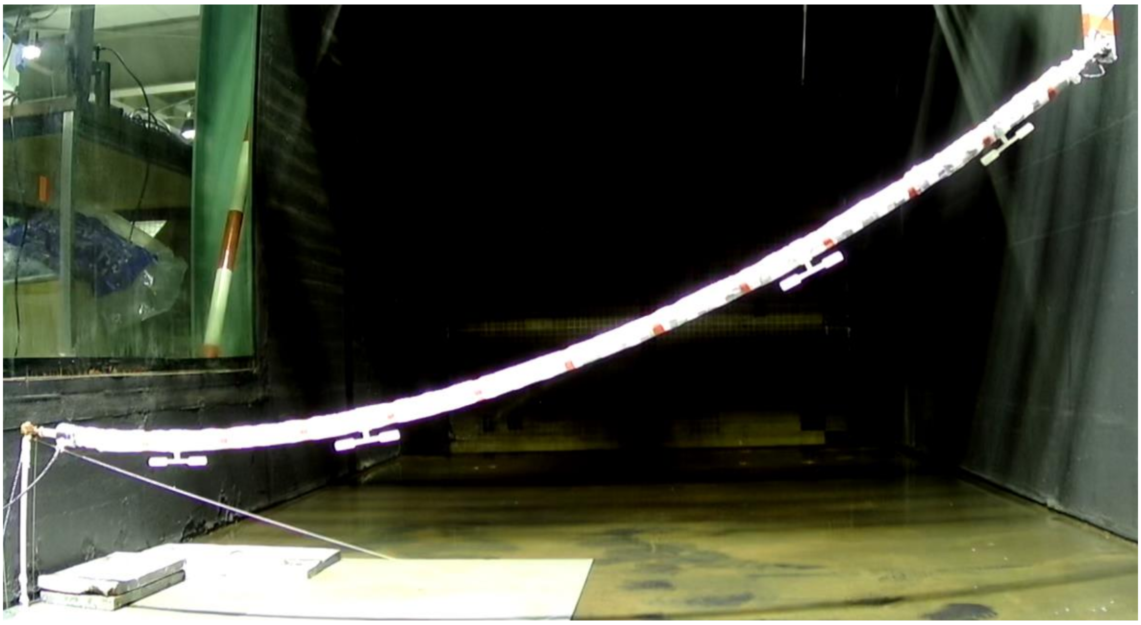

Fig.6-4 Cable model with the vibration dampers.

## 6.3 Response of vibrations

### 6.3.1 Maximum vibration amplitudes

The spatially maximum vibration amplitudes of the experimental results for both the cable with vibration dampers and the cable without vibration dampers as a function of the flow velocity $U_0$ are compared in Fig 6-5 (Fig 6-5(a) shows the total vibration and Fig

6-5(b) (c) (d) show the discomposed vibration). For comparison, the mean offset of the cable from its initial position is removed during the data processing. Since the total vibration amplitude of the cable with vibration dampers in Fig 6-5(a) at $U_0 > 0.44m/s$ cannot be properly extracted from the video data owing to the fact that the vibration frequencies are over the Nyquist sampling frequency. Based on the same reason, the vibration amplitude in w-direction at $U_0 = 0.6m/s$ cannot also be properly extracted from the video data.

As shown in Fig 6-5, the maximum vibration amplitudes as a function of the flow velocity $U_0$ recorded a different trend between the cable and the cable with vibration dampers. In the cross-flow u and v direction, at $U_0 \leq 0.36m/s$, the maximum vibration amplitudes of the cable with vibration dampers increase and then decrease as the flow velocity $U_0$ increases, and are larger than that of the cable. The vibration dampers actually increase the cross-flow vibration amplitude as shown in Fig 6-5(c) (d). At $0.36\mathrm{m}/s < U_0 \leq 0.6m/s$ the maximum vibration amplitudes of the cable with vibration dampers are smaller than that of the cable. At $U_0 = 0.56m/s$, the vibration amplitudes decrease by 75% (Fig 6-5(c)) and 60% (Fig 6-5(d)) in the cross-flow u and v direction, respectively.

In the in-line w direction, the maximum vibration amplitudes of the cable with vibration dampers are always smaller than that of the cable under all the flow velocities. At $U_0 = 0.2m/s$, the vibration amplitudes decrease by 87% (Fig 6-5(b)) in in-line w direction. It is worth mentioning that at $U_0 = 0.4m/s$, the maximum vibration amplitudes of the cable with vibration dampers rapidly decrease in all cases as shown in Fig 6-5. It can be seen that, the maximum responses v in Y direction are always greater than the maximum responses u in X direction and w in Z direction under all the flow velocities.

For the cable at the lock-in area $0.36\mathrm{m/s} \leq U_0 < 0.6m/s$, the maximum vibration amplitudes are greater than those outside the lock-in area. As a contrast, for the cable with vibration dampers in the cross-flow u and v direction, maximum vibration amplitudes are smaller than that outside the lock-in area. The vibration dampers effectively reduce the maximum vibration amplitude.

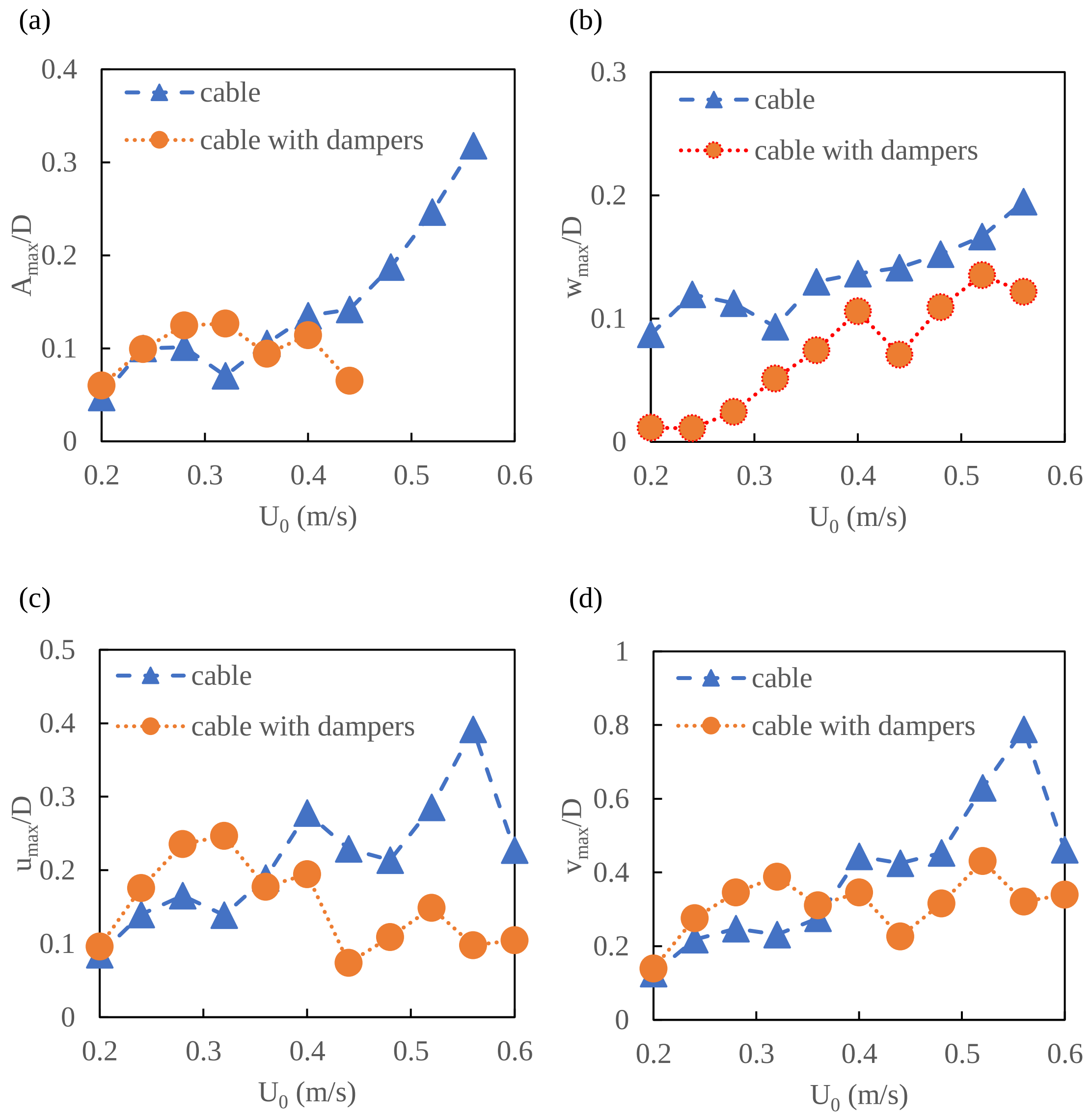


Fig.6-5 Comparison of the spatially maximum vibration amplitudes of experimental results for both the cable and the cable with vibration dampers as the flow velocity $U_0$ (a) total vibration amplitudes; (b) in-line w vibration amplitudes; (c) cross-flow u vibration amplitudes; (d) cross-flow v vibration amplitudes.

### 6.3.2 Maximum RMS vibration amplitudes

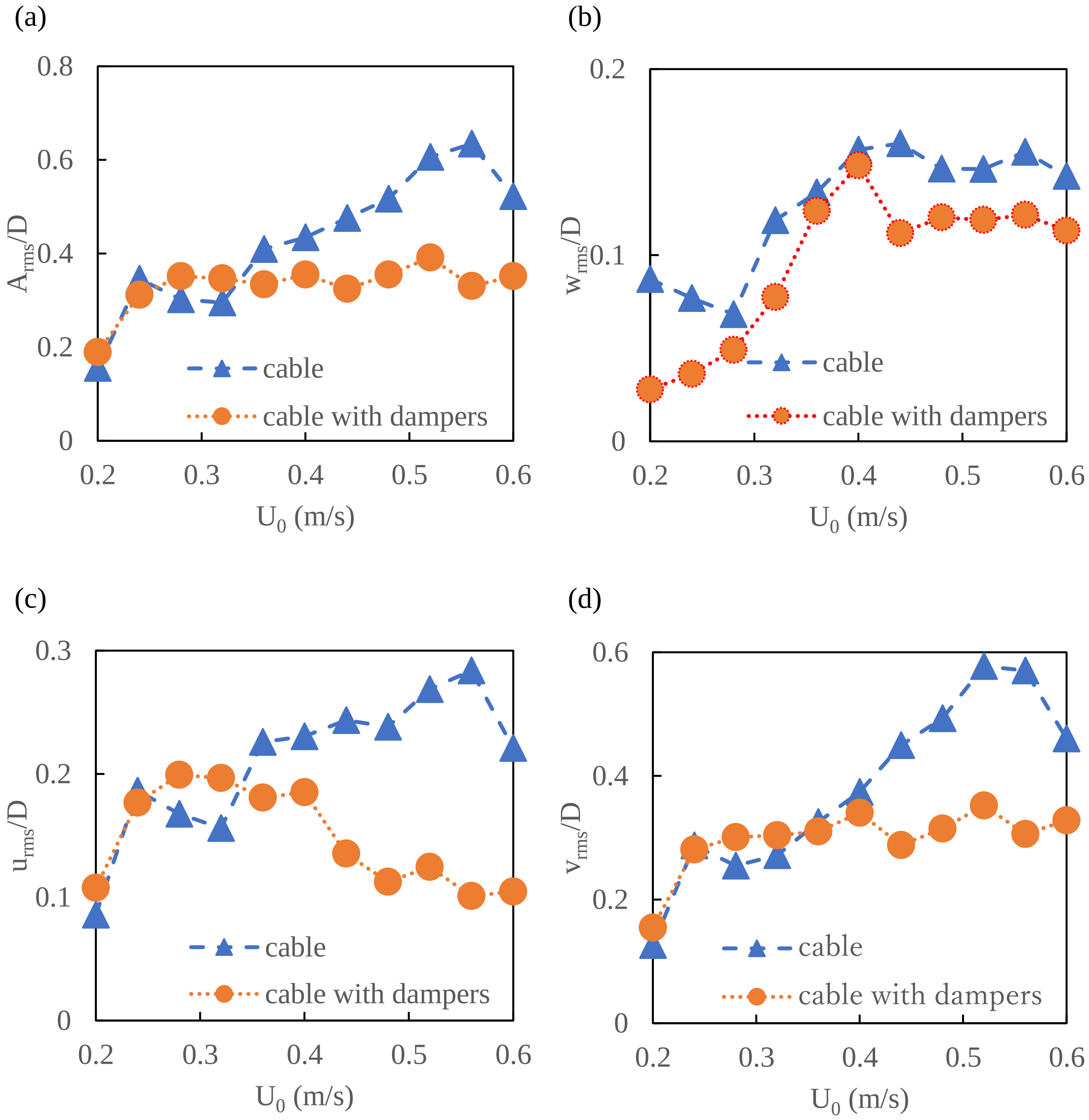


Fig.6-6 Comparison of the spatially maximum RMS vibration amplitudes of experimental results for both the cable and the cable with vibration dampers as the flow velocity $U_0$ (a) total RMS vibration amplitudes; (b) in-line w RMS vibration amplitudes; (c) cross-flow u RMS vibration amplitudes; (d) cross-flow v RMS vibration amplitudes.

The spatially maximum root-mean-squared (RMS) vibration amplitudes for experiment of both the cable and the cable with vibration dampers as the flow velocity $U_0$ are compared in Fig.6-6 (Fig.6-6(a) shows the total RMS vibration and Fig.6-6(b) (c) (d) show the discomposed RMS vibration). It can be found that as the flow velocity $U_0$ increases, the maximum and RMS vibration amplitudes recorded a very similar trend as shown in Fig.6-5 and Fig.6-6. The maximum RMS responses v in Y direction are always greatest under all the flow velocities. For the cable with vibration dampers, the total RMS vibration amplitude shows slight variation as the flow velocity $U_0$ increases in Fig.6-6(a). At $U_0 = 0.56m/s$, the RMS vibration amplitudes decrease by 64.4% (Fig.6-6(c)) and 46.4% (Fig.6-6(d)) in the cross-flow u and v direction, respectively. At $U_0 = 0.2m/s$, the RMS vibration amplitudes decrease by 68% (Fig.6-6(b)) in in-line w direction. The vibration dampers effectively reduce the RMS vibration amplitude.

### 6.3.3 Time-averaged in-line displacements

The time-averaged in-line displacements of experimental results for both the cable and the cable with vibration dampers as the flow velocity $U_0$ are shown in Fig.6-7. It can be seen that as the flow velocity $U_0$ increases, the time-averaged equilibrium profiles progressively deviate from the initial position (Y-axis). At low flow velocities $U_0 \leq 0.24\,m/s$, the results of the cable with vibration dampers are larger than those in the cable as shown in Fig.6-7. As the flow velocity $U_0$ increases, the results of the cable with vibration dampers are smaller than those in the cable. It is worth mentioning that in the experiment of cable, at the flow velocities $U_0 \geq 0.56\,m/s$, the time-averaged equilibrium profiles are almost constant, the in-line displacements reach the maximum.

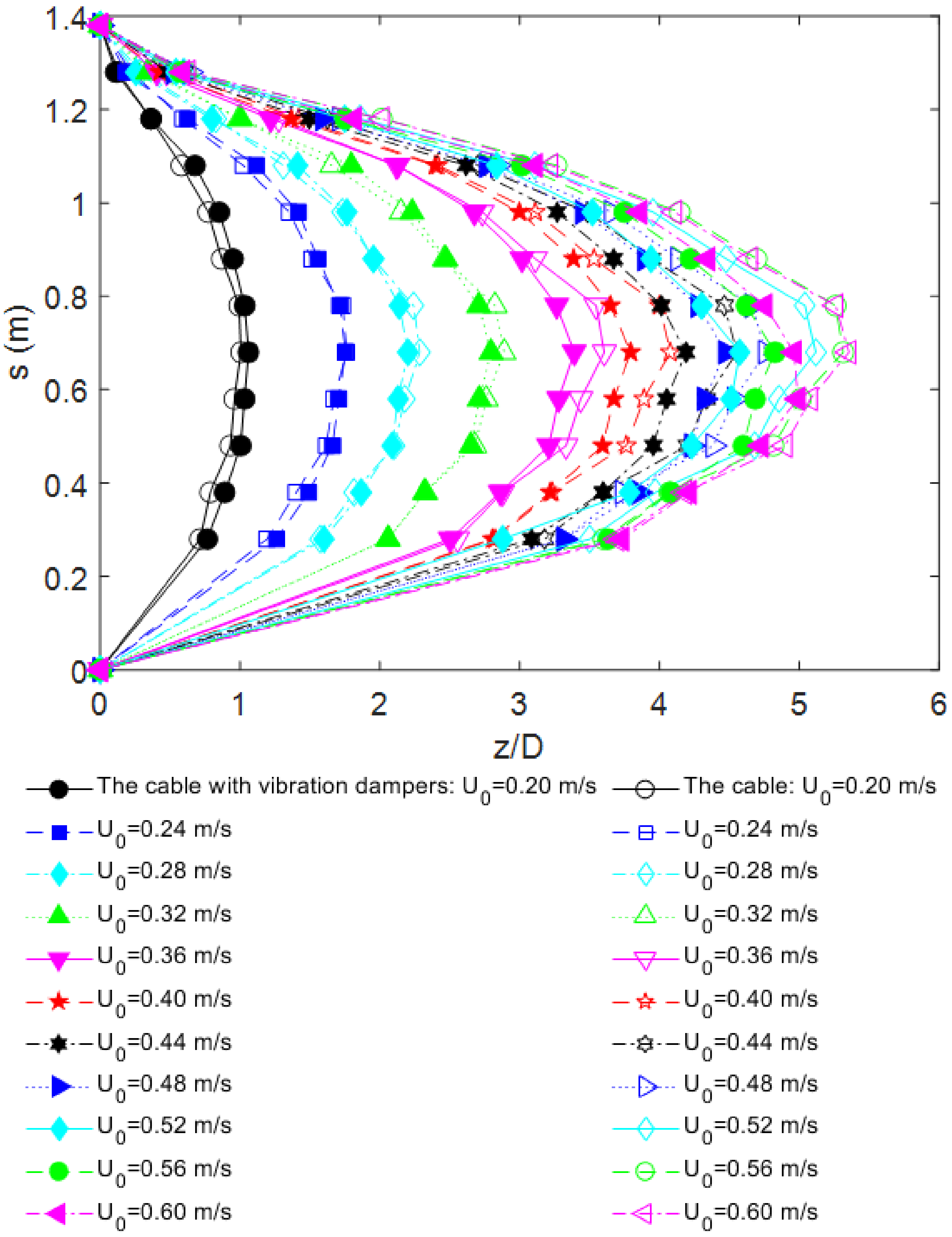


Fig.6-7 Comparison of the time-averaged in-line displacements of experimental results for both the cable and the cable with vibration dampers as the flow velocity $U_0$. (Solid marks represent the cable with vibration dampers and hollow mark represent the cable).

### 6.3.4 Vibration frequencies

The cable vibration frequencies calculated by Fast Fourier Transform (FFT) method, are also compared as shown in Fig.6-8 and Fig.6-9. It is observed that the cross-flow vibration frequencies in X direction and in Y direction are always equal under all the flow velocities as shown in Fig.6-8. Under the condition of $U_0 = 0.36\, m/s$, the cross-flow vibration frequency ratio (which is the ratio of vibration frequency $f$ to natural frequency $f_n$ of the cable) is close to 1, the cable goes into lock-in range. At low flow velocities $U_0 \leq 0.40\, m/s$, as shown in Fig.6-8, the cross-flow vibration frequencies of both the cable and the cable with vibration dampers are almost equal, and as the flow velocity $U_0$ increases, the cross-flow vibration frequencies of the cable with vibration dampers increase rapidly and are greater than those of the cable.

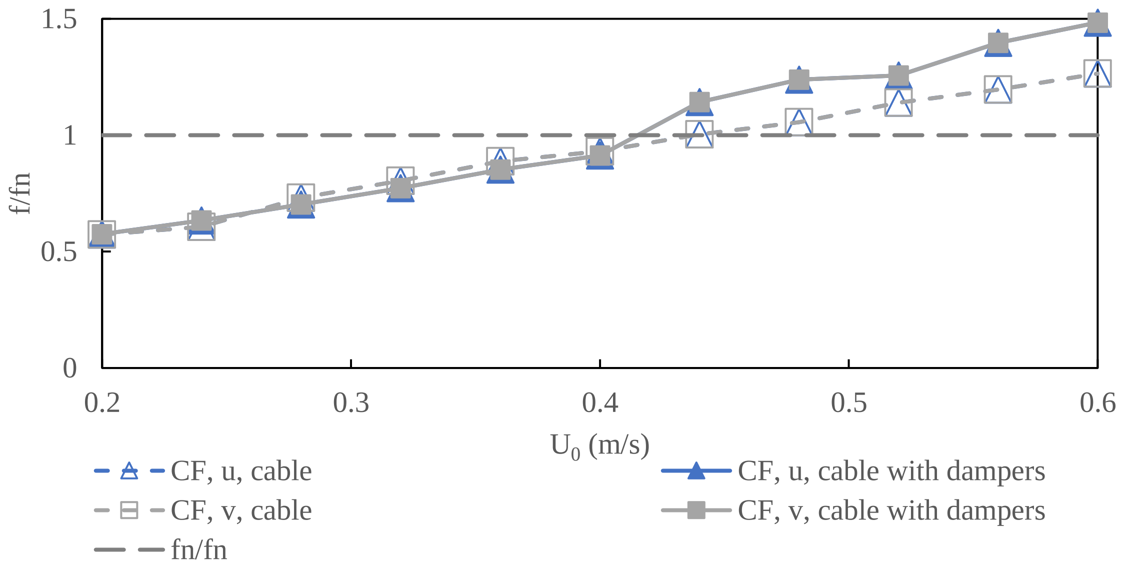


Fig.6-8 Comparison of the frequency ratio in the cross-flow u and v direction of experimental results for both the cable and the cable with vibration dampers as the flow velocity $U_0$.

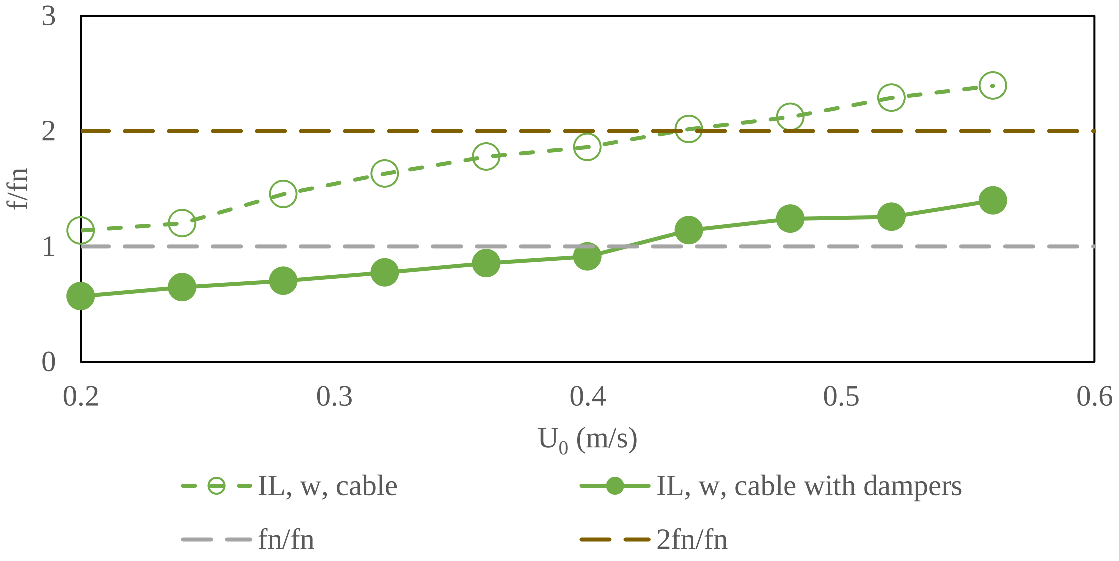


Fig.6-9 Comparison of the frequency ratio in the in-line w direction of experimental results for both the cable and the cable with vibration dampers as the flow velocity $U_0$.

As shown in Fig.6-9, the in-line vibration frequencies in Z direction are approximate twice as large as the cross-flow vibration frequencies for the cable, as a contrast, for the cable with vibration dampers, the in-line vibration frequencies are approximately the same as the cross-flow vibration frequencies. The vibration dampers effectively change the 2:1 ratio resonance of in-line to cross-flow vibration frequencies.

## 6.4 Response of tensions

### 6.4.1 Time-history and amplitudes of tensions

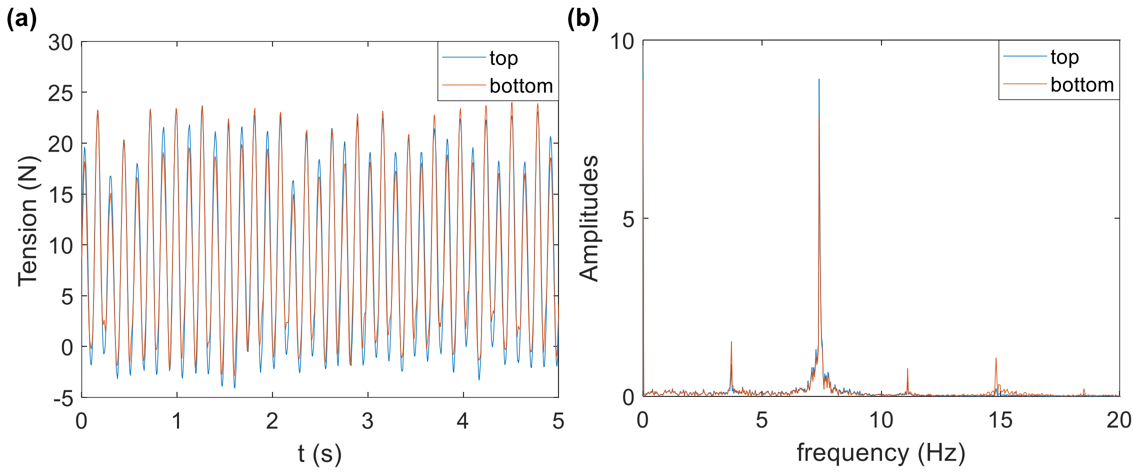


Fig.6-10 Time-history and amplitudes of tensions at both ends of the cable in the experiment under $U_0 = 0.56\,m/s$.

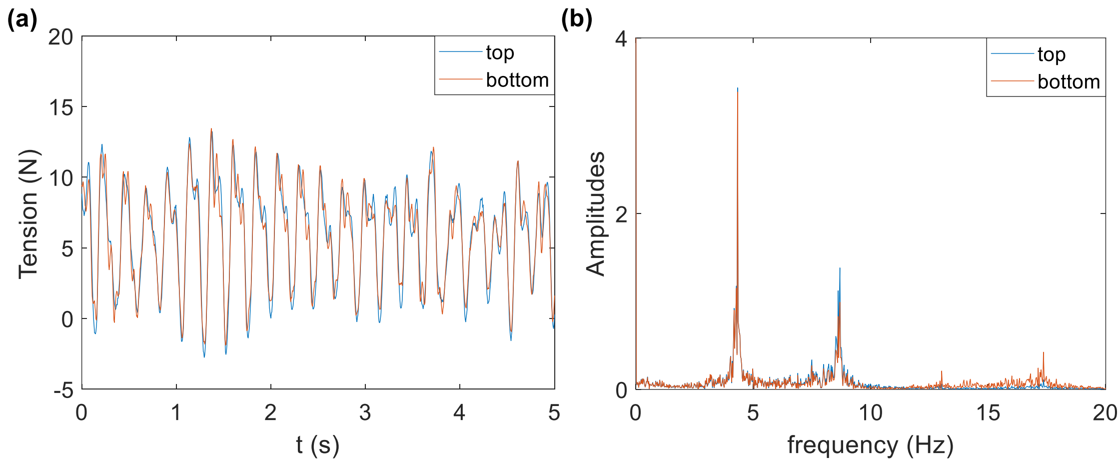


Fig.6-11 Time-history and amplitudes of tensions at both ends of the cable with vibration dampers in the experiment under $U_0 = 0.56\,m/s$.

The tension at the two ends of the cable in the experiment under $U_0 = 0.56\,m/s$ and the associated frequency-domain analysis results are shown in Fig 6-10 (the cable) and Fig 6-11 (the cable with vibration dampers). Since the tension measured by the load cells is reset at the beginning of each experiment to reduce the sensor drift during long-term measurement, the initial tension is subtracted from the experimental results for ease of comparison. From Fig 6-10 and Fig 6-11, it is observed that the tension at the two ends almost vibrates synchronously, and the vibration frequency is almost equal. The tension at the top end are slightly greater than the tension at the bottom. It is obvious that the time-history tensions in the cable are much larger than those in the cable with vibration dampers. For both ends of the cable, the second frequency of tension is the dominant frequency are shown in Fig 6-10, and as a contrast, for both ends of the cable with vibration dampers, the first frequency of tension is the dominant frequency are shown in Fig 6-11. This is consistent with the Fig 6-9. In summary, the vibration dampers effectively reduce the time-history tensions and change the tension frequencies.

### 6.4.2 Average of tensions

As shown in Fig 6-12, the time-averaged tension at both ends of the cable and the cable with vibration dampers as a function of the flow velocity $U_0$ is compared. It could be observed that as the flow velocity $U_0$ increases, the average tension increases at both the top and bottom ends of the cable and the cable with vibration dampers. The time-average tension at both ends of the cable and the cable with vibration dampers are almost equal under all the flow velocities other than at the flow velocity $U_0 = 0.52m/s$ as shown in Fig 6-12. Just like the vibration displacement response in Fig 6-5 and Fig 6-6, when the flow velocity is low ($U_0 \leq 0.36m/s$), the time-average tension of the cable with vibration dampers is larger than those of the cable. As the flow velocity increases, the time-average tension of the cable increases rapidly and is larger than those of the cable with vibration dampers. At the flow velocity $U_0 = 0.56\,m/s$, compared to the cable, the top average of tension of the cable with vibration dampers decreases by 34%. The vibration dampers effectively reduce the time-average values of the tension.

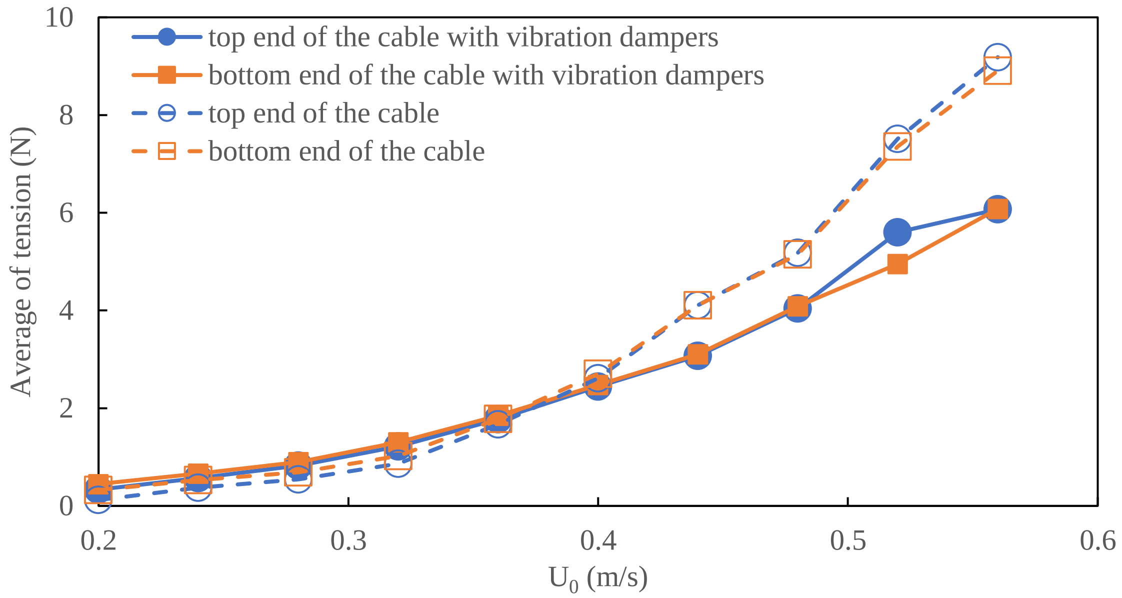


Fig.6-12 Comparison of the time-average values of tensions at both ends of the cable and the cable with vibration dampers.

### 6.4.3 Maximum vibration amplitudes of tensions

As shown in Fig 6-13, the maximum vibration amplitudes of the tensions at the two ends of the cable and the cable with vibration dampers are compared. It is found that as the flow velocity $U_0$ increases, the maximum vibration amplitudes of the tensions of cable are much larger than those of cable with vibration dampers. For the cable with vibration dampers, at the flow velocity $U_0 \geq 0.40m/s$, the maximum vibration amplitudes of the tensions show slight variation as the flow velocity $U_0$ increases in Fig 6-13. At $U_0 = 0.56\ m/s$, the maximum vibration amplitude of the tension at the top end decreases by 61.5%. The vibration dampers effectively reduce the maximum vibration amplitude of the tension.

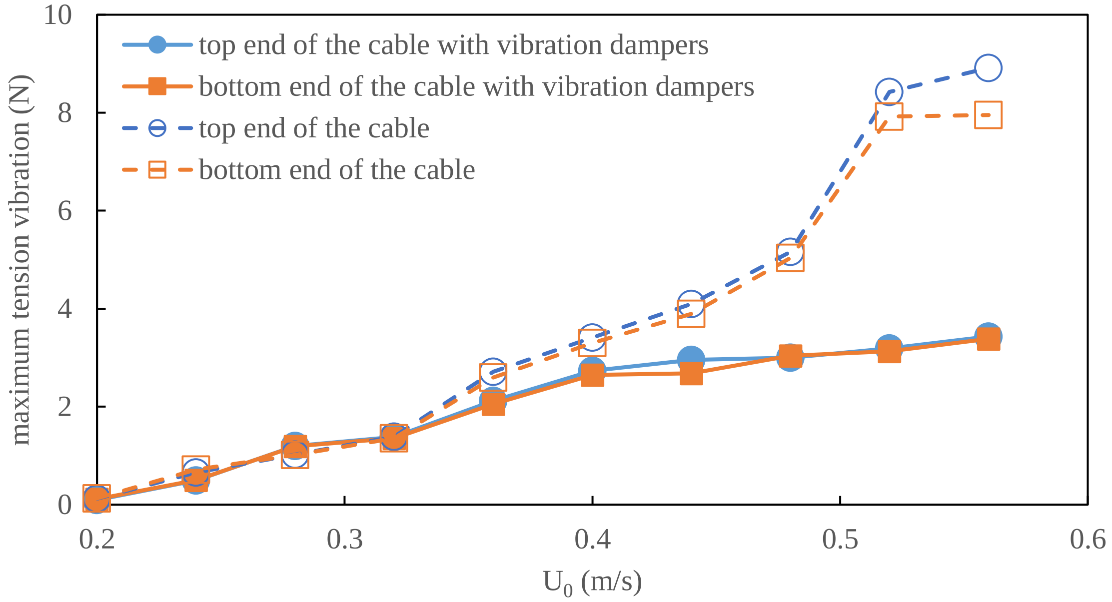


Fig.6-13 Comparison of the maximum vibration amplitudes of tensions at both ends of the cable and the cable with vibration dampers.

### 6.4.4 Frequency of tensions

The frequencies of the tension at the two ends of the cable and the cable with vibration dampers are compared with each other as shown in Fig 6-14. It could be observed that the frequency of tension increases gradually as the flow velocity $U_0$ increases. Compared to the cable vibration frequencies shown in Fig 6-9, the tension frequencies are roughly equal to the in-line vibration frequencies. The top end tension frequencies and the bottom end tension frequencies are always equal under all the flow velocities. Overall, the vibration dampers effectively reduce the response of tensions.

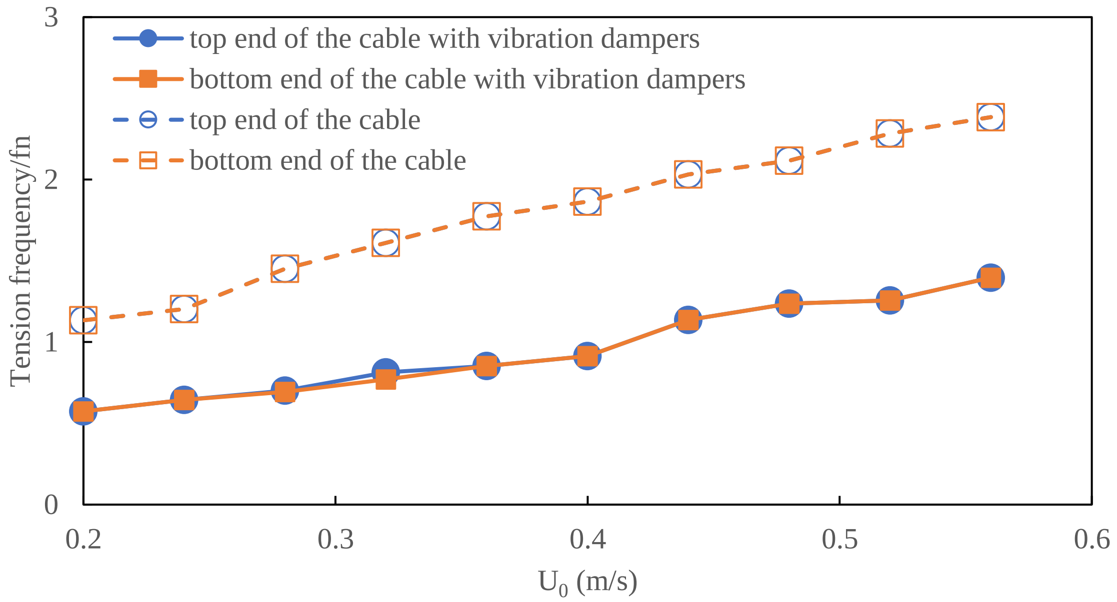


Fig.6-14 Comparison of the tension frequency at both ends of the cable and the cable with vibration dampers.

## 5.5 Chapter conclusion

In this chapter, an experiment on a submarine cable model has been carried out to study the VIV suppression effectiveness of vibration dampers. The experimental results of both the cable and the cable with vibration dampers are compared in perpendicular flow on the VIV responses, including the maximum vibration amplitudes, the maximum RMS vibration amplitudes, the time-averaged in-line displacements, the vibration frequencies; the time-history and amplitudes, the average, the maximum vibration amplitudes and the frequencies of tensions. The experimental results have demonstrated that the vibration dampers could effectively reduce the responses of VIV.

The main conclusions can be summarized as follows:

(1) For the cable with vibration dampers, in the cross-flow u and v direction, at $U_0 \leq 0.36m/s$, the maximum vibration amplitudes are larger than those of the cable. The vibration dampers actually increase the cross-flow vibration amplitude. At $0.36\mathrm{m/s} < U_0 \leq 0.6m/s$ the maximum vibration amplitudes are smaller than those

of the cable. At $U_0 = 0.56m/s$, the vibration amplitudes decrease by 75% and 60% in the cross-flow u and v direction, respectively. In the in-line w direction, the maximum vibration amplitudes are always smaller than those of the cable under all the flow velocities. At $U_0 = 0.2m/s$, the vibration amplitudes decrease by 87% in in-line w direction. The vibration dampers effectively reduce the vibration amplitude. For two cases, the maximum responses v in Y direction are always greater than the maximum responses u in X direction and w in Z direction under all the flow velocities and a saw-tooth pattern could be observed as the flow velocity $U_0$ increases.

(2) For two cases, the spatially maximum vibration amplitudes and maximum RMS vibration amplitudes are similar trend at three directions as the flow velocity $U_0$ increases. For the cable with vibration dampers, the total RMS vibration amplitudes show slight variation as the flow velocity $U_0$ increases. At $U_0 = 0.56m/s$, the RMS vibration amplitudes decrease by 64.4% and 46.4% in the cross-flow u and v direction, respectively. At $U_0 = 0.2m/s$, the RMS vibration amplitudes decrease by 68% in in-line w direction.

(3) For two cases, as the flow velocity $U_0$ increases, the time-averaged equilibrium profiles progressively deviate from the initial position (Y-axis). At low flow velocities $U_0 \leq 0.24\, m/s$, the results of the cable with vibration dampers are larger than those in the cable. As the flow velocity $U_0$ increases, the results of the cable with vibration dampers are smaller than those in the cable. For the cable, at the flow velocities $U_0 \geq 0.56\, m/s$, the time-averaged equilibrium profiles are almost constant, the in-line displacements reach the maximum.

(4) The cross-flow vibration frequencies in X direction and in Y direction are always equal under all the flow velocities for each experiment in both experimental results. When the frequency ratio $f/f_n < 1$, the vibration frequencies of both experimental results are almost equal, and as the flow velocity $U_0$ increases, the vibration frequencies of the cable with vibration dampers increase rapidly and are greater than those of the cable.

(5) For the in-line vibration frequencies in Z direction, for the cable the nearly 2:1 resonance could be found where the in-line vibration frequency is twice as large as the cross-flow vibration frequency. As a contrast, for the cable with vibration dampers, the in-line vibration frequencies are approximately the same as the cross-flow vibration frequencies.

(6) The phase and frequency of tension at both the top and bottom ends of the cable for each experiment are always almost equal, and the top tensions are slightly greater than the bottom tensions in each experiment. The time-history tensions in the cable are much larger than those in the cable with vibration dampers. For both ends of the cable with vibration dampers, the first frequency of tension is the dominant frequency, when the second frequency is the dominant frequency for both ends of the cable.

(7) As the flow velocity $U_0$ increases, the average tension increases at both the top and bottom ends of both experimental results, and in each experimental result, the tension average values of the top end and bottom end are always equal under all the flow velocities other than at the flow velocity $U_0 = 0.52m/s$. Just like the vibration displacement response, for the cable with vibration dampers, the average tensions are larger than those of the cable at $U_0 \leq 0.36m/s$, and smaller as the flow velocity $U_0$ increases. At the flow velocity $U_0 = 0.56\,m/s$, the top average of tension of the cable with vibration dampers decreases by 34%.

(8) As the flow velocity $U_0$ increases, the maximum vibration amplitudes of the tensions of cable are much larger than those of cable with vibration dampers. For the cable with vibration dampers, at the flow velocity $U_0 \geq 0.40m/s$, the maximum vibration amplitudes of the tensions show slight variation as the flow velocity $U_0$ increases. At $U_0 = 0.56\,m/s$, the maximum vibration amplitude of the tension at the top end decreases by 61.5%.

(9) As the flow velocity $U_0$ increases, for both experimental results, the frequency of tension increases. The frequencies at both top end and bottom end in each experimental result are always equal, and the frequency values of tension are roughly equal to the corresponding in-line vibration frequency. Therefore, the tension

frequencies of the cable with vibration dampers are always smaller than those of the cable.

# CHAPTER 7 Conclusion and future work

## 7.1 Summary

The bottom-mounted offshore wind power holds immense potential in the foreseeable future, with submarine cables serving as crucial components in the transmission of electric energy for these turbines. Despite constituting less than 10% of the total capital costs of a wind farm, offshore cable failures have accounted for up to 80% of total financial losses and insurance claims in the past decade. Considering the substantial investment in an offshore wind farm, even minor improvements in submarine cable performance could lead to significant cost savings. In this research, many aspects related to submarine cables, have been investigated and studied.

(1) A numerical model based on Euler-Bernoulli beam theory and a single van der Pol wake oscillator model is proposed to study the VIV of a long flexible catenary cable with a low mass ratio. The wake model uses only one oscillator to describe the in-line and cross-flow vibration with consideration of their nonlinear coupling.

(2) Experimental studies on vortex-induced vibrations of a long flexible catenary cable are carried out.

(3) Experiment are carried out to study the VIV suppression effectiveness of vibration dampers for a long flexible catenary cable.

Experimental and numerical investigations have been carried out. The numerical model has been validated through a comparison with experimental results of long flexible cylinders in the literature, and the qualitative features of experimental results are reasonably captured by the numerical model. On the other hand, an experiment about the submarine cable has been carried out to further validate the proposed numerical model. Moreover, for studying the VIV suppression of the cable, another experiment about the submarine cable with vibration dampers has been carried out. The main conclusions can be summarized in this thesis as follows:

For the numerical prediction results and experimental results of the cable:

(1) In the validation, the numerical model can capture the VIV feature of experiments in the literature in good form.

(2) The lock-in phenomenon found in the experiment can be reproduced by the proposed numerical model. Two lock-in area can be found as the flow velocity $U_0$ increases. The spatially maximum vibration amplitudes and maximum RMS vibration amplitudes are similar trend at three directions as the flow velocity $U_0$ increases.

(3) As the flow velocity $U_0$ increases, in the cross-flow direction (u and v) the cable constantly vibrates with a standing wave pattern, as a contrast in the in-line direction (w) the cable gradually vibrates from a standing wave pattern to a traveling wave pattern.

(4) The cross-flow vibration frequencies in the X and Y direction are the same for all the flow velocities. Moreover, the cross-flow and in-line vibration frequency increase with the flow velocity $U_0$, while the in-line vibration frequency is nearly twice as the cross-flow vibration frequency.

(5) The phase and frequency of the axial tension at both the top and bottom ends of the cable are almost same. As the flow velocity $U_0$ increases, both the average tension and the vibration frequency increase. The frequency of tension variation is roughly in line with the in-line cable vibration frequency. At $U_0 = 0.56\, m/s$ the top average tension can be more than 1.6 times of the initial tension.

For the experimental results of both the cable with vibration dampers and the cable without vibration dampers:

(1) For two cases, the spatially maximum vibration amplitudes and maximum RMS vibration amplitudes are similar trend at three directions as the flow velocity $U_0$ increases.

(2) Due to the vibration dampers, the maximum vibration amplitudes can be reduced by up to 75%, 60% and 87% in the X, Y and Z direction, respectively. The maximum RMS vibration amplitudes can be reduced by up to 64.4%, 46.4% and 68% in the X, Y and Z direction, respectively.

(3) At low flow velocities $U_0 \leq 0.24\,m/s$, the time-averaged equilibrium profiles of the cable with vibration dampers are larger than those in the cable. As the flow velocity $U_0$ increases, the results of the cable with vibration dampers are smaller than those in the cable.

(4) The cross-flow vibration frequencies in X direction and in Y direction are always equal under all the flow velocities. When the frequency ratio $f/f_n < 1$, the vibration frequencies of both experimental results are almost equal, and as the flow velocity $U_0$ increases, the vibration frequencies of the cable with vibration dampers increase rapidly and are greater than those of the cable.

(5) For the cable with vibration dampers, the in-line vibration frequencies are approximately the same as the cross-flow vibration frequencies. As a contrast, for the cable, the nearly 2:1 resonance where the in-line vibration frequency is twice as large as the cross-flow vibration frequency, could be found.

(6) For two cases, the phase and frequency of tension at both the top and bottom ends of the cable are always almost equal. The time-history tensions of the cable are much larger than those in the cable with vibration dampers. As the flow velocity $U_0$ increases, the average tension increases at both the top and bottom ends. The average of tension of the cable with vibration dampers can be reduced by up to 34%.

(7) As the flow velocity $U_0$ increases, the maximum vibration amplitudes of the tensions of cable are much larger than those of cable with vibration dampers. For the cable with vibration dampers, at the flow velocity $U_0 \geq 0.40m/s$, the maximum vibration amplitudes of the tensions show slight variation as the flow velocity $U_0$ increases. At $U_0 = 0.56\,m/s$, the maximum vibration amplitude of the tension at the top end decreases by 61.5%

(8) The frequency of tension increases as the flow velocity $U_0$ increases. The frequencies at both top end and bottom end are always equal, and the frequency values of tension are roughly equal to the corresponding in-line vibration frequency. The tension frequencies of the cable with vibration dampers are always smaller than those of the cable.

## 6.2 Future work

The present research aims to propose a mathematical model for predicting the dynamic response of vortex-induced vibrations (VIV) in submarine cable and to experimentally study the VIV suppression effectiveness of vibration dampers. There are still many challenges to overcome in order to achieve this goal.

1. The time variation of the cable local inclination angles $\beta$ is not considered. In this study, the influence of $\beta$ is neglected. The primary reason is that when $\beta$ is considered and an iterative solution approach is employed, it has been found that the solution does not converge. A novel numerical approach considering β as a variable value will be studied in future work.

2. One notable limitation in this study is the omission of submarine cable-seabed interaction within the touchdown zone (TDZ). While the section of the cable resting on the seabed may not be subject to ocean current excitation, the energy generated by the periodic oscillation of the cable due to VIV propagates along the cable to the TDZ. As a result, the periodic cable oscillation induced by VIV at the TDZ introduces an additional dynamic boundary condition for cable-seabed interaction. In the subsequent phase of the study, it is imperative to develop a mathematical model that incorporates cable-seabed interaction to provide a more comprehensive understanding of the system.

3. Another problem pertains to the VIV suppression experiment conducted on the cable with vibration dampers. The results of this study indicate that the vibration dampers effectively mitigate the displacement and tension of the cable. Nevertheless, further investigation is warranted to optimize the number of dampers and their installation locations on the cable to achieve the most effective suppression.

# Reference

[1] "Renewable capacity statistics 2024." *International Renewable Energy Agency* (2024), ISBN: 978-92-9260-587-2.

[2] Pelc, Robin, and Rod M. Fujita. "Renewable energy from the ocean." *Marine Policy* 26.6 (2002): 471-479. DOI: 10.1016/S0308-597X(02)00045-3.

[3] Gunn, Kester, and Clym Stock-Williams. "Quantifying the global wave power resource." *Renewable energy* 44 (2012): 296-304. DOI: 10.1016/j.renene.2012.01.101.

[4] Sasaki, Wataru. "Predictability of global offshore wind and wave power." *International journal of marine energy* 17 (2017): 98-109. DOI: 10.1016/j.ijome.2017.01.003.

[5] Melikoglu, Mehmet. "Current status and future of ocean energy sources: A global review." *Ocean Engineering* 148 (2018): 563-573. DOI: 10.1016/j.oceaneng.2017.11.045.

[6] Nguyen, Phuoc Quy Phong. "Ocean Energy-A Clean Energy Source." *European Journal of Engineering and Technology Research* 4.1 (2019): 5-11. DOI: 10.24018/ejeng.2019.4.1.1062.

[7] Copping, Andrea E., et al. "Potential environmental effects of marine renewable energy development—the state of the science." *Journal of Marine Science and Engineering* 8.11 (2020): 879. DOI: 10.3390/jmse8110879.

[8] Faedo, Nicolás, et al. "SWELL: An open-access experimental dataset for arrays of wave energy conversion systems." *Renewable Energy* 212 (2023): 699-716. DOI: 10.1016/j.renene.2023.05.069.

[9] "Global offshore wind report 2023. " *World Forum Offshore Wind* (2004).

[10] "Enabling frameworks for offshore wind scale up: Innovations in permitting." *International Renewable Energy Agency* (2023), ISBN: 978-92-9260-549-0.

[11] "Getting fit for 55 and set for 2050." *European Technology & Innovation Platform on Wind Energy* (2021).

[12] "International Energy Agency. China Wind Energy Development Roadmap 2050." *OECD Publishing* (2012).

[13] Zhang, Shuangyi, and Xichen Li. "Future projections of offshore wind energy resources in China using CMIP6 simulations and a deep learning-based downscaling method." *Energy* 217 (2021): 119321. DOI: 10.1016/j.energy.2020.119321.

[14] Maris, Georgios, and Floros Flouros. "The green deal, national energy and climate plans in Europe: Member States' compliance and strategies." *Administrative Sciences* 11.3 (2021): 75. DOI: 10.3390/admsci11030075.

[15] Delagrammatikas, Georgios, and Spyridon Roukanas. "Offshore Wind Farm in the Southeast Aegean Sea and Energy Security." *Energies* 16.13 (2023): 5208. DOI: 10.3390/en16135208.

[16] Groeneveld, Berend, Sietse Gerssen, and Petra Hoogakker. "How American Based HVDC and OSS Offshore Wind Substations can Profit from the European Learning Curve." *Offshore Technology Conference*. OTC, 2023. DOI: 10.4043/32343-MS.

[17] "Offshore Wind Roadmap for Sri Lanka." *World Bank Group* (2023).

[18] Barai, Munim Kumar, and Bidyut Baran Saha. "Energy security and sustainability in japan." *Evergreen* 2.1 (2015): 49-56. DOI: 10.5109/1500427.

[19] Moroga, Kana, et al. "State of implementation of environmental and energy policies adopted by the regional governments in Japan." *Evergreen* 2.2 (2015): 14-23. DOI: 10.5109/1544076.

[20] Gima, Hiroki, and Tsuyoshi Yoshitake. "A comparative study of energy security in Okinawa prefecture and the state of Hawaii." *Evergreen* 3.2 (2016): 36-44. DOI: 10.5109/1800870.

[21]https://www.meti.go.jp/shingikai/energy_environment/yojo_furyoku/sagyo_bukai/pdf/003_s01_00.pdf. *New Energy and Industrial Technology Development Organization (NEDO)* (2021), Japan.

[22]https://www.enecho.meti.go.jp/category/saving_and_new/saiene/yojo_furyoku/dl/vision/vision_first.pdf. Offshore wind industry vision of Japan. *Ministry of Economic, Trade and Industry* (2020), Japan.

[23] Wu, Xiaoni, et al. "Foundations of offshore wind turbines: A review." *Renewable and Sustainable Energy Reviews* 104 (2019): 379-393. DOI: 10.1016/j.rser.2019.01.012.

[24] Firestone, Jeremy, Alison W. Bates, and Adam Prefer. "Power transmission: Where the offshore wind energy comes home." *Environmental Innovation and Societal Transitions* 29 (2018): 90-99. DOI: 10.1016/j.eist.2018.06.002.

[25] Itiki, Rodney, et al. "A comprehensive review and proposed architecture for offshore power system." International Journal of Electrical Power & Energy Systems 111 (2019): 79-92. DOI: 10.1016/j.ijepes.2019.04.008.

[26] Gulski, E., et al. "Discussion of electrical and thermal aspects of offshore wind farms' power cables reliability." *Renewable and Sustainable Energy Reviews* 151 (2021): 111580. DOI: 10.1016/j.rser.2021.111580.

[27] Tisheva, P. "Cable Failures Account for Most of Offshore Wind Losses, June 2016." https://renewablesnow.com/news/cable-failures-account-for-most-of-offshore-wind-losses-528959/

[28] Masoumi, Masoud. "Machine Learning Solutions for Offshore Wind Farms: A Review of Applications and Impacts." *Journal of Marine Science and Engineering* 11.10 (2023): 1855. DOI: 10.3390/jmse11101855.

[29] El Mountassir, O., and C. Strang-Moran. "Offshore Wind Subsea Power Cables. Installation, Operation and Market Trends." (2018).

[30] Hodge, N., and R. Maurer. "Power under the Sea, Allianz Global Risk Dialogue, Autumn 2014." (2014): 26-29.

[31] Li, Ruan, Mohamed Karma, and Changhong Hu. "Two-Dimensional VIV Simulation of a Cylinder Close to a Wall with High Reynolds Number by Overset Mesh." *Evergreen* (2023): 219-229. DOI: 10.5109/6781072.

[32] https://www.balmoraloffshore.com/solutions/offshore-wind/fixed-wind-turbine-solutions.

[33] Williamson, Charles HK, and R. Govardhan. "Vortex-induced vibrations." *Annu. Rev. Fluid Mech.* 36 (2004): 413-455. DOI: 10.1146/annurev.fluid.36.050802.122128

[34] Wang, Jungao, et al. "Fatigue damage induced by vortex-induced vibrations in oscillatory flow." *Marine Structures* 40 (2015): 73-91. DOI: 10.1016/j.marstruc.2014.10.011.

[35] Zhang, Mengmeng, et al. "A time domain prediction method for the vortex-induced vibrations of a flexible riser." *Marine Structures* 59 (2018): 458-481. DOI: 10.1016/j.marstruc.2018.02.010.

[36] Lu, Yan, et al. "Fatigue damage characteristics of a flexible cylinder under concomitant excitation of time-varying axial tension and VIV." *Ocean Engineering* 288 (2023): 116079. DOI: 10.1016/j.oceaneng.2023.116079.

[37] Ma, Bowen, and Narakorn Srinil. "Numerical Prediction of 3-D Vortex-Induced Vibration of Catenary Riser In Planar and Non-Planar Flows." *International Conference on Offshore Mechanics and Arctic Engineering*. Vol. 85185. American Society of Mechanical Engineers, 2021. DOI: 10.1115/OMAE2021-61830.

[38] Assi, Gustavo RS, et al. "Experimental investigation of the flow-induced vibration of a curved cylinder in convex and concave configurations." *Journal of Fluids and Structures* 44 (2014): 52-66. DOI: 10.1016/j.jfluidstructs.2013.10.011.

[39] Seyed-Aghazadeh, Banafsheh, Collin Budz, and Yahya Modarres-Sadeghi. "The influence of higher harmonic flow forces on the response of a curved circular cylinder undergoing vortex-induced vibration." *Journal of Sound and Vibration* 353 (2015): 395-406. DOI: 10.1016/j.jsv.2015.04.036.

[40] Srinil, Narakorn, Bowen Ma, and Licong Zhang. "Experimental investigation on in-plane/out-of-plane vortex-induced vibrations of curved cylinder in parallel and perpendicular flows." *Journal of Sound and Vibration* 421 (2018): 275-299. DOI: 10.1016/j.jsv.2018.02.021.

[41] Chaplin, J. R., and Roger King. "Laboratory measurements of the vortex-induced vibrations of an untensioned catenary riser with high curvature." *Journal of Fluids and Structures* 79 (2018): 26-38. DOI: 10.1016/j.jfluidstructs.2018.01.008.

[42] Seyed-Aghazadeh, Banafsheh, et al. "An experimental investigation of vortex-induced vibration of a curved flexible cylinder." *Journal of Fluid Mechanics* 927 (2021): A21. DOI: 10.1017/jfm.2021.725.

[43] Morooka, Celso K., and Raphael I. Tsukada. "Experiments with a steel catenary riser model in a towing tank." *Applied Ocean Research* 43 (2013): 244-255. DOI: 10.1016/j.apor.2013.10.010.

[44] Zhu, Hongjun, Pengzhi Lin, and Jie Yao. "An experimental investigation of vortex-induced vibration of a curved flexible pipe in shear flows." *Ocean Engineering* 121 (2016): 62-75. DOI: 10.1016/j.oceaneng.2016.05.025.

[45] Zhu, Hongjun, Pengzhi Lin, and Yue Gao. "Vortex-induced vibration and mode transition of a curved flexible free-hanging cylinder in exponential shear flows." *Journal of Fluids and Structures* 84 (2019): 56-76. DOI: 10.1016/j.jfluidstructs.2018.10.009.

[46] Zhu, Hongjun, et al. "Spatial–temporal mode transition in vortex-induced vibration of catenary flexible riser." *Journal of Fluids and Structures* 102 (2021): 103234. DOI: 10.1016/j.jfluidstructs.2021.103234.

[47] Zhu, Hongjun, et al. "An experimental investigation on the vortex-induced vibration mode transition and response interaction of a fixed–hinged catenary flexible riser." *Physics of Fluids* 35.1 (2023). DOI: 10.1063/5.0131257.

[48] Zhu, Hongjun, et al. "Experimental investigation on the vortex-induced vibration of an inclined flexible pipe and the evaluation of the independence principle." *Physics of Fluids* 35.3 (2023). DOI: 10.1063/5.0138364.

[49] Moe, Geir, et al. "Predictions and model tests of an SCR undergoing VIV in flow at oblique angles." *International Conference on Offshore Mechanics and Arctic Engineering*. Vol. 37432. 2004. DOI: 10.1115/OMAE2004-51563.

[50] Chen, D., Xu, R., Yuan, Z., Pan, G., & Marzocca, P. (2023). The effect of vortex induced vibrating cylinders on airfoil aerodynamics. *Applied Mathematical Modelling*, *115*, 868-885. DOI: 10.1016/j.apm.2022.12.001.

[51] Chen, D., Xu, R., Lin, Y., Gao, N., Pan, G., & Pier, M. (2023). Nonlinear energy sink-based study on vortex-induced vibration and control of foil-cylinder coupled structure. *Ocean Engineering*, *286*, 115623. DOI: 10.1016/j.oceaneng.2023.115623.

[52] Dalheim, J. (2000, May). Numerical prediction of vortex-induced vibration on steel catenary risers. In *ISOPE International Ocean and Polar Engineering Conference* (pp. ISOPE-I). ISOPE.

[53] Halse, K. H., Mo, K., & Lie, H. (1999, August). Vortex induced vibrations of a catenary riser. In *Third International Symposium on Cable Dynamics, Trondheim Norway*.

[54] Huang, K., Chen, H. C., & Chen, C. R. (2010, June). Flexible catenary riser VIV simulation in uniform current. In *ISOPE International Ocean and Polar Engineering Conference* (pp. ISOPE-I). ISOPE.

[55] Facchinetti, Matteo Luca, Emmanuel De Langre, and Francis Biolley. "Coupling of structure and wake oscillators in vortex-induced vibrations." *Journal of Fluids and structures* 19.2 (2004): 123-140. DOI: 10.1016/j.jfluidstructs.2003.12.004.

[56] Srinil, Narakorn, and Hossein Zanganeh. "Modelling of coupled cross-flow/in-line vortex-induced vibrations using double Duffing and van der Pol oscillators." *Ocean Engineering* 53 (2012): 83-97. DOI: 10.1016/j.oceaneng.2012.06.025.

[57] Zanganeh, Hossein, and Narakorn Srinil. "Three-dimensional VIV prediction model for a long flexible cylinder with axial dynamics and mean drag magnifications." *Journal of Fluids and Structures* 66 (2016): 127-146. DOI: 10.1016/j.jfluidstructs.2016.07.004.

[58] Gu, Jijun, et al. "Analytical solution of mean top tension of long flexible riser in modeling vortex-induced vibrations." *Applied Ocean Research* 41 (2013): 1-8. DOI: 10.1016/j.apor.2013.01.004.

[59] Gu, Jijun, et al. "Dynamic Response of a Fluid-Conveying Riser Subject to Vortex-Induced Vibration: Integral Transform Solution." *International Conference on Offshore Mechanics and Arctic Engineering*. Vol. 45479. American Society of Mechanical Engineers, 2014. DOI: 10.1115/OMAE2014-24639.

[60] Gao, Yun, et al. "Time-domain prediction of the coupled cross-flow and in-line vortex-induced vibrations of a flexible cylinder using a wake oscillator model." *Ocean Engineering* 237 (2021): 109631. DOI: 10.1016/j.oceaneng.2021.109631.

[61] Gao, Yun, et al. "Three-dimensional vortex-induced vibrations of a circular cylinder predicted using a wake oscillator model." *Marine Structures* 80 (2021): 103078. DOI: 10.1016/j.marstruc.2021.103078.

[62] Gao, Yun, et al. "Numerical prediction of vortex-induced vibrations of a long flexible riser with an axially varying tension based on a wake oscillator model." *Marine Structures* 85 (2022): 103265. DOI: 10.1016/j.marstruc.2022.103265.

[63] Leclercq, Tristan, and Emmanuel de Langre. "Vortex-induced vibrations of cylinders bent by the flow." *Journal of Fluids and Structures* 80 (2018): 77-93. DOI: 10.1016/j.jfluidstructs.2018.03.008.

[64] Qu, Yang, and Andrei V. Metrikine. "Modelling of coupled cross-flow and in-line vortex-induced vibrations of flexible cylindrical structures. Part I: model description and validation." *Nonlinear Dynamics* 103 (2021): 3059-3082. DOI: 10.1007/s11071-020-06168-3.

[65] Qu, Yang, and Andrei V. Metrikine. "Modelling of coupled cross-flow and in-line vortex-induced vibrations of flexible cylindrical structures. Part II: on the importance of in-line coupling." *Nonlinear Dynamics* 103 (2021): 3083-3112. DOI: 10.1007/s11071-020-06027-1.

[66] Qu, Yang, and Andrei V. Metrikine. "A single van der pol wake oscillator model for coupled cross-flow and in-line vortex-induced vibrations." *Ocean Engineering* 196 (2020): 106732. DOI: 10.1016/j.oceaneng.2019.106732.

[67] Luo, Ruo, et al. "Numerical and experimental investigation of a floating overhead power transmission system." *Ocean Engineering* 284 (2023): 115085. DOI: 10.1016/j.oceaneng.2023.115085.

[68] Gao, Yun, et al. "Experimental investigation on the suppression device of VIV of a flexible riser." *International Conference on Offshore Mechanics and Arctic Engineering*. Vol. 45400. American Society of Mechanical Engineers, 2014. DOI: 10.1115/OMAE2014-23427.

[69] Lou, Min, Zhiwei Chen, and Peng Chen. "Experimental investigation of the suppression of vortex induced vibration of two interfering risers with splitter plates." *Journal of Natural Gas Science and Engineering* 35 (2016): 736-752. DOI: 10.1016/j.jngse.2016.09.012.

[70] Liu, Qingsong, et al. "Numerical simulation on the forced oscillation of rigid riser with helical strakes in different section shapes." *Ocean Engineering* 190 (2019): 106439. DOI: 10.1016/j.oceaneng.2019.106439.

[71] Liu, Xiuquan, et al. "An optimization method for the suppression device configuration of risers." *Ocean Engineering* 194 (2019): 106619. DOI: 10.1016/j.oceaneng.2019.106619.

[72] Song, Jixiang, et al. "Study on suppressing the vortex-induced vibration of flexible riser in frequency domain." *Applied Ocean Research* 116 (2021): 102882. DOI: 10.1016/j.apor.2021.102882.

[73] Jiang, Zhenxing, et al. "Experimental investigation on the VIV of two side-by-side risers fitted with triple helical strakes under coupled interference effect." *Journal of Fluids and Structures* 101 (2021): 103202. DOI: j.jfluidstructs.2020.103202.

[74] Guo, Li, et al. "Experimental investigation on vortex-induced vibration of marine towing cable with suppression device." *Ocean Engineering* 269 (2023): 113531. DOI: 10.1016/j.oceaneng.2022.113531.

[75] Zheng, Hanxu, and Jiasong Wang. "A numerical study on the vortex-induced vibration of flexible cylinders covered with differently placed buoyancy modules." *Journal of Fluids and Structures* 100 (2021): 103174. DOI: 10.1016/j.jfluidstructs.2020.103174.

[76] Yuan, Yuchao, et al. "Numerical investigation of vortex-induced vibration response for a full-scale riser with staggered buoyancy modules." Ocean Engineering 252 (2022): 111241. DOI: 10.1016/j.oceaneng.2022.111241.

[77] Youyi, S. U. N., C. H. E. N. Guoming, and C. H. A. N. G. Yuanjiang. "Riser buoyancy distribution optimization based on vortex-induced vibration suppression." *Journal of China University of Petroleum* 33.3 (2009): 123-127.

[78] Chang, Yuanjiang. "Design approach and its application for deepwater drilling risers." *Dongying: University of Petroleum (East China)* (2008).

[79] ZHOU Yun, et al. "Preparation and strength analysis of buoyancy materials for deep-sea drilling riser." *JOURNAL OF CHONGQING UNIVERSITY* 40.7 (2017): 19-24. DOI: 10.11835/j.issn.1000-582X.2017.07.003.

[80] Ma, Yexuan, et al. "The effect of time-varying axial tension on VIV suppression for a flexible cylinder attached with helical strakes." *Ocean Engineering* 241 (2021): 109981. DOI: 10.1016/j.oceaneng.2021.109981.

[81] Xu, Wanhai, et al. "The effect of yaw angle on VIV suppression for an inclined flexible cylinder fitted with helical strakes." *Applied Ocean Research* 67 (2017): 263-276. DOI: 10.1016/j.apor.2017.07.014.

[82] Xu, Wan-hai, et al. "Passive VIV reduction of an inclined flexible cylinder by means of helical strakes with round-section." *China Ocean Engineering* 32.4 (2018): 413-421. DOI: 10.1007/s13344-018-0043-8.

[83] Fang, Sam M., et al. "VIV response of a flexible cylinder with varied coverage by buoyancy elements and helical strakes." *Marine Structures* 39 (2014): 70-89. DOI: 10.1016/j.marstruc.2014.06.004.

[84] Wu, Jie, et al. "VIV responses of riser with buoyancy elements: forced motion test and numerical prediction." *International Conference on Offshore Mechanics and Arctic Engineering*. Vol. 57649. American Society of Mechanical Engineers, 2017. DOI: 10.1115/OMAE2017-61768.

[85] Li, Ang, Baiheng Wu, and Dixia Fan. "Vortex-induced vibration of risers with staggered buoyancy modules of small aspect ratio." *Applied Ocean Research* 120 (2022): 103014. DOI: 10.1016/j.apor.2021.103014.

[86] Wu, Jie, et al. "NDP riser VIV model test with staggered buoyancy elements." *International Conference on Offshore Mechanics and Arctic Engineering*. Vol. 49934. American Society of Mechanical Engineers, 2016. DOI: 10.1115/OMAE2016-54503.

[87] Wu, Jie, Malakonda Reddy Lekkala, and Muk Chen Ong. "Prediction of riser VIV with staggered buoyancy elements." *International Conference on Offshore Mechanics and Arctic Engineering*. Vol. 49934. American Society of Mechanical Engineers, 2016. DOI: 10.1115/OMAE2016-54502.

[88] Lekkala, M. R., et al. "A practical technique for hydrodynamic coefficients modification in SHEAR7 for fatigue assessment of riser buoyancy modules under vortex-induced vibration." *Ocean Engineering* 217 (2020): 107760. DOI: 10.1016/j.oceaneng.2020.107760.

[89] Cloutier, L., et al. "EPRI transmission line reference book: wind-induced conductor motion." (2006): 1-400.

[90] Chan, John, et al. "EPRI Transmission Line Reference Book: wind-induced Conductor Motion." *EPRI, N° 1018554* (2009).

[91] Wang, Yafei, et al. "Stagnation point-induced vibration on ultra-long stay cables and the vibration control by using a novel stockbridge damper." *Journal of Wind Engineering and Industrial Aerodynamics* 241 (2023): 105535. DOI: 10.1016/j.jweia.2023.105535.

[92] Berthellemy, Jacques, et al. "Stockbridge dampers for extending the fatigue life of a cable at St Nazaire cable stayed bridge." *Engineering Failure Analysis* 141 (2022): 106581. DOI: 10.1016/j.engfailanal.2022.106581.

[93] Nie, Xiaochun, et al. "Ultra-wideband piezoelectric energy harvester based on Stockbridge damper and its application in smart grid." *Applied energy* 267 (2020): 114898. DOI: 10.1016/j.apenergy.2020.114898.

[94] Sauter, D., and P. Hagedorn. "On the hysteresis of wire cables in Stockbridge dampers." *International journal of non-linear Mechanics* 37.8 (2002): 1453-1459. DOI: 10.1016/S0020-7462(02)00028-8.

[95] Vaja, N. K., O. R. Barry, and E. Y. Tanbour. "On the modeling and analysis of a vibration absorber for overhead powerlines with multiple resonant frequencies." *Engineering Structures* 175 (2018): 711-720. DOI: 10.1016/j.engstruct.2018.08.051.

[96] Kim, Sunjoong, Sejin Kim, and Ho-Kyung Kim. "High-mode vortex-induced vibration of stay cables: Monitoring, cause investigation, and mitigation." *Journal of Sound and Vibration* 524 (2022): 116758. DOI: 10.1016/j.jsv.2022.116758.

[97] Srinil, Narakorn. "Analysis and prediction of vortex-induced vibrations of variable-tension vertical risers in linearly sheared currents." *Applied Ocean Research* 33.1 (2011): 41-53. DOI: 10.1016/j.apor.2010.11.004.

[98] Feng, Yunli, et al. "Predictions for combined In-Line and Cross-Flow VIV responses with a novel model for estimation of tension." *Ocean Engineering* 191 (2019): 106531. DOI: 10.1016/j.oceaneng.2019.106531.

[99] Feng, Y. L., et al. "Vortex-induced vibrations of flexible cylinders predicted by wake oscillator model with random components of mean drag coefficient and lift coefficient." *Ocean Engineering* 251 (2022): 110960. DOI: 10.1016/j.oceaneng.2022.110960.

[100] Hisamatsu, Ryoya, and Tomoaki Utsunomiya. "A study on coupled behavior analysis and position keeping system for OTEC plantship and cold water pipe." *Journal of the Japan Society of Naval Architects and Ocean Engineers* 32 (2021). (in japanese). DOI: 10.2534/jjasnaoe.32.193.

[101] Chucheepsakul, Somchai, and Narakorn Srinil. "Free vibrations of three-dimensional extensible marine cables with specified top tension via a variational method." *Ocean Engineering* 29.9 (2002): 1067-1096. DOI: 10.1016/S0029-8018(01)00064-6.

[102] Chucheepsakul, Somchai, Narakorn Srinil, and Pisek Petchpeart. "A variational approach for three-dimensional model of extensible marine cables with specified top tension." *Applied Mathematical Modelling* 27.10 (2003): 781-803. DOI: 10.1016/S0307-904X(03)00089-1.

[103] Srinil, Narakorn, Giuseppe Rega, and Somchai Chucheepsakul. "Three-dimensional non-linear coupling and dynamic tension in the large-amplitude free vibrations of arbitrarily sagged cables." *Journal of Sound and Vibration* 269.3-5 (2004): 823-852. DOI: 10.1016/S0022-460X(03)00137-8.

[104] Nayfeh, Ali H., and P. Frank Pai. *Linear and nonlinear structural mechanics*. John Wiley & Sons, 2008.

[105] Rega, Giuseppe, N. Srinil, and S. Chucheepsakul. "Internally resonant nonlinear free vibrations of horizontal/inclined sagged cables." *International Design*

*Engineering Technical Conferences and Computers and Information in Engineering Conference*. Vol. 47438. 2005. DOI: 10.1115/DETC2005-84752.

[106] Rega, Giuseppe, and Narakorn Srinil. "Nonlinear hybrid-mode resonant forced oscillations of sagged inclined cables at avoidances." (2007): 324-336. DOI: 10.1115/1.2756064.

[107] Srinil, Narakorn, and Giuseppe Rega. "The effects of kinematic condensation on internally resonant forced vibrations of shallow horizontal cables." *International Journal of Non-Linear Mechanics* 42.1 (2007): 180-195. DOI: 10.1016/j.ijnonlinmec.2006.09.005.

[108] Srinil, Narakorn, Giuseppe Rega, and Somchai Chucheepsakul. "Two-to-one resonant multi-modal dynamics of horizontal/inclined cables. Part I: Theoretical formulation and model validation." *Nonlinear Dynamics* 48 (2007): 231-252. DOI: 10.1007/s11071-006-9086-0.

[109] Srinil, Narakorn, and Giuseppe Rega. "Two-to-one resonant multi-modal dynamics of horizontal/inclined cables. Part II: Internal resonance activation, reduced-order models and nonlinear normal modes." *Nonlinear Dynamics* 48 (2007): 253-274. DOI: 10.1007/s11071-006-9087-z.

[110] Rega, Giuseppe, Narakorn Srinil, and Rocco Alaggio. "Experimental and numerical studies of inclined cables: free and parametrically-forced vibrations." *Journal of Theoretical and Applied Mechanics* 46.3 (2008): 621-640. ISSN 1429-2955.

[111] Srinil, Narakorn. "Cabling to connect offshore wind turbines to onshore facilities." *Offshore wind farms*. Woodhead Publishing, 2016. 419-440. DOI: 10.1016/B978-0-08-100779-2.00013-1.

[112] Ricciardi, Giuseppe, and F. Saitta. "A continuous vibration analysis model for cables with sag and bending stiffness." *Engineering Structures* 30.5 (2008): 1459-1472. DOI: 10.1016/j.engstruct.2007.08.008.

[113] Srinil, Narakorn, et al. "New model for vortex-induced vibration of catenary riser." *ISOPE Pacific/Asia Offshore Mechanics Symposium*. ISOPE, 2008.

[114] Srinil, Narakorn, Marian Wiercigroch, and Patrick O'Brien. "Reduced-order modelling of vortex-induced vibration of catenary riser." *Ocean Engineering* 36.17-18 (2009): 1404-1414. DOI: 10.1016/j.oceaneng.2009.08.010.

[115] Srinil, Narakorn. "Multi-mode interactions in vortex-induced vibrations of flexible curved/straight structures with geometric nonlinearities." *Journal of Fluids and Structures* 26.7-8 (2010): 1098-1122. DOI: 10.1016/j.jfluidstructs.2010.08.005.

[116] Srinil, Narakorn, Patrick O'Brien, and Marian Wiercigroch. "Numerical and experimental comparisons of vortex-induced vibrations of marine risers in uniform/sheared currents." *International Conference on Offshore Mechanics and Arctic Engineering*. Vol. 49149. 2010. DOI: 10.1115/OMAE2010-20192.

[117] Zanganeh, Hossein, and Narakorn Srinil. "Coupled axial/lateral VIV of marine risers in sheared currents." *International Conference on Offshore Mechanics and Arctic Engineering*. Vol. 56482. American Society of Mechanical Engineers, 2015. DOI: 10.1115/OMAE2015-41606.

[118] Ma, Bowen, and Narakorn Srinil. "Dynamic characteristics of deep-water risers carrying multiphase flows." *International Conference on Offshore Mechanics and Arctic Engineering*. Vol. 51241. American Society of Mechanical Engineers, 2018. DOI: 10.1115/OMAE2018-77381.

[119] Bakis, Konstantinos N., and Narakorn Srinil. "Internal flow-induced instability analysis of catenary risers." *MARINE VIII: proceedings of the VIII International Conference on Computational Methods in Marine Engineering*. CIMNE, 2019. ISBN: 978-84-949194-3-5

[120] Ma, Bowen, and Narakorn Srinil. "Planar dynamics of inclined curved flexible riser carrying slug liquid–gas flows." *Journal of Fluids and Structures* 94 (2020): 102911. DOI: 10.1016/j.jfluidstructs.2020.102911.

[121] Soares, Bruno, and Narakorn Srinil. "Nonlinear Wake-Induced Vibration of Downstream Cylinder in Staggered Arrangements." *ASME International*

*Mechanical Engineering Congress and Exposition*. Vol. 85611. American Society of Mechanical Engineers, 2021. DOI: 10.1115/IMECE2021-67776.

[122] Kakanda, Kabutakapua, et al. "A power series method for static and dynamic analysis of offshore mooring lines." *Ocean Engineering* 266 (2022): 112589. DOI: 10.1016/j.oceaneng.2022.112589.

[123] Ma, Bowen, and Narakorn Srinil. "Influence of internal slug flow on vortex-induced vibration of flexible riser with variable curvature." *International Conference on Offshore Mechanics and Arctic Engineering*. Vol. 85925. American Society of Mechanical Engineers, 2022. DOI: 10.1115/OMAE2022-78236.

[124] Ma, Bowen, and Narakorn Srinil. "Prediction model for multidirectional vortex-induced vibrations of catenary riser in convex/concave and perpendicular flows." *Journal of Fluids and Structures* 117 (2023): 103826. DOI: 10.1016/j.jfluidstructs.2022.103826.

[125] Ruan, Li, Hongzhong Zhu, and Changhong Hu. "A study on vortex-induced vibration of a long flexible catenary cable in perpendicular flow." *Ocean Engineering* 305 (2024): 117937. DOI: 10.1016/j.oceaneng.2024.117937.

[126] Qu, Yang, et al. "Numerical study on the characteristics of vortex-induced vibrations of a small-scale subsea jumper using a wake oscillator model." *Ocean Engineering* 243 (2022): 110028. DOI: 10.1016/j.oceaneng.2021.110028.

[127] Qu, Yang, et al. "Application of a modified wake oscillator model to vortex-induced vibration of a free-hanging riser subjected to vessel motion." *Ocean Engineering* 253 (2022): 111165. DOI: 10.1016/j.oceaneng.2022.111165.

[128] Qu, Yang, et al. "Numerical study on vortex-induced vibrations of a flexible cylinder subjected to multi-directional flows." *Physics of Fluids* 35.3 (2023). DOI: 10.1063/5.0138063.

[129] Qu, Yang, et al. "Vortex-induced vibrations of a top tensioned riser subjected to flows with spanwise varying directions." *International Journal of Mechanical Sciences* 242 (2023): 107954. DOI: 10.1016/j.ijmecsci.2022.107954.

[130] Qu, Yang, et al. "Cross-flow vortex-induced vibrations of a top tensioned riser subjected to boundary disturbances with frequencies close to vortex shedding." *Applied Ocean Research* 138 (2023): 103659. DOI: 10.1016/j.apor.2023.103659.

[131] Ogink, R. H. M., and A. V. Metrikine. "A wake oscillator with frequency dependent coupling for the modeling of vortex-induced vibration." *Journal of sound and vibration* 329.26 (2010): 5452-5473. DOI: 10.1016/j.jsv.2010.07.008.

[132] Qin, Lihai. *Development of reduced-order models for lift and drag on oscillating cylinders with higher-order spectral moments*. Diss. Virginia Tech, 2004.

[133] Postnikov, Andrey, Ekaterina Pavlovskaia, and Marian Wiercigroch. "2DOF CFD calibrated wake oscillator model to investigate vortex-induced vibrations." *International Journal of Mechanical Sciences* 127 (2017): 176-190. DOI: 10.1016/j.ijmecsci.2016.05.019.

[134] Bourghet, R., G. E. Karniadakis, and M. S. Triantafillou. "On the validity of the independence principle applied to the vortex-induced vibrations of a flexible cylinder inclined at 60 degrees." *Journal of Fluids Structures* 53 (2015): 58-69. DOI: 10.1016/j.jfluidstructs.2014.09.005.

[135] Martinelli, Luca, et al. "Power umbilical for ocean renewable energy systems-feasibility and dynamic response analysis." *Proc. Int Conf Ocean Energy*. 2010.

[136] Thies, Philipp R., Lars Johanning, and George H. Smith. "Assessing mechanical loading regimes and fatigue life of marine power cables in marine energy applications." *Proceedings of the Institution of Mechanical Engineers, Part O: Journal of Risk and Reliability* 226.1 (2012): 18-32. DOI: 10.1177/1748006X1141353.

[137] Rentschler, Manuel UT, Frank Adam, and Paulo Chainho. "Design optimization of dynamic inter-array cable systems for floating offshore wind turbines." *Renewable and Sustainable Energy Reviews* 111 (2019): 622-635. DOI: 10.1016/j.rser.2019.05.024.

[138] Okpokparoro, Salem, and Srinivas Sriramula. "Reliability analysis of floating wind turbine dynamic cables under realistic environmental loads." *Ocean Engineering* 278 (2023): 114594. DOI: j.oceaneng.2023.114594.

[139] Zang, Zhipeng, et al. "Experimental study on dynamic responses of a tensioned flexible vertical cylinder under waves and combined current and waves." *Ocean Engineering* 266 (2022): 113159. DOI: 10.1016/j.oceaneng.2022.113159.

[140] Brown, D. "Video modeling: combining dynamic model simulations with traditional video analysis." In *American Association of Physics Teachers (AAPT) Summer Meeting* (2008).

[141] Fehér, Rafael, and Juan Pablo Julca Avila. "Parametric behavior of a vortex-induced vibration model of cylinders with two degrees-of-freedom using a wake oscillator." *Journal of Offshore Mechanics and Arctic Engineering* 144.2 (2022): 021905. DOI: 10.1115/1.4052483.

[142] Song, Ji-ning, et al. "Laboratory tests of vortex-induced vibrations of a long flexible riser pipe subjected to uniform flow." *Ocean engineering* 38.11-12 (2011): 1308-1322. DOI: 10.1016/j.oceaneng.2011.05.020.

[143] Srinil, Narakorn, Giuseppe Rega, and Somchai Chucheepsakul. "Large amplitude three-dimensional free vibrations of inclined sagged elastic cables." *Nonlinear Dynamics* 33.2 (2003): 129-154. DOI: 10.1023/A:1026019222997.

[144] Jauvtis, N. A., and C. H. K. Williamson. "The effect of two degrees of freedom on vortex-induced vibration at low mass and damping." *Journal of Fluid Mechanics* 509 (2004): 23-62. DOI: 10.1017/S0022112004008778.

[145] Dahl, J. M., et al. "Dual resonance in vortex-induced vibrations at subcritical and supercritical Reynolds numbers." *Journal of Fluid Mechanics* 643 (2010): 395-424. DOI: 10.1017/S0022112009992060.

[146] Dahl, Jason Jason Michael. *Vortex-induced vibration of a circular cylinder with combined in-line and cross-flow motion*. Diss. Massachusetts Institute of Technology, 2008. http://hdl.handle.net/1721.1/44747.

[147] Vibration and Vibration Dampers in Transmission Line. https://www.electricaldeck.com/2021/08/vibration-and-vibration-dampers-in-transmission-line.html.

[148] Zondi, Zakhele Mathews, Tiyamike Ngonda, and Modify AE Kaunda. "Modification of a Stockbridge Damper: A Review." *2023 14th International Conference on Mechanical and Intelligent Manufacturing Technologies (ICMIMT)*. IEEE, 2023. DOI: 10.1109/ICMIMT59138.2023.10199783.

[149] Larsen, Allan. "Vibration Excitation and Damping of Suspension Bridge Hanger Cables." *International Symposium on Dynamics and Aerodynamics of Cables*. Cham: Springer Nature Switzerland, 2023. DOI: 10.1007/978-3-031-47152-0_19.

[150] Yoon, Ranhee, Erdi Gulbahce, and Oumar Barry. "Free Vibration Modeling of Power Line Conductors." *IFAC-PapersOnLine* 56.3 (2023): 409-414. DOI: 10.1016/j.ifacol.2023.12.058.

[151] Ali, Nihad Mohamed, and A. S. Sajith. "Vibration Control of Bridge Suspenders Using TMD and RTLD—A Comparative Study." *Proceedings of SECON'21: Structural Engineering and Construction Management*. Springer International Publishing, 2022. DOI: 10.1007/978-3-030-80312-4_83.

[152] Wang, Zhisong, Hong-Nan Li, and Gangbing Song. "Aeolian vibration control of power transmission line using Stockbridge type dampers—A review." *International Journal of Structural Stability and Dynamics* 21.01 (2021): 2130001. DOI: 10.1142/S0219455421300019.

[153] Stockbridge, George H. "Vibration damper." U.S. Patent No. 1,675,391. 3 Jul. 1928.

[154] Claren, Rodolfo, and Giorgio Diana. "Mathematical analysis of transmission line vibration." *IEEE Transactions on power apparatus and systems* 12 (1969): 1741-1771.

[155] Wagner, H., et al. "Dynamics of Stockbridge dampers." *Journal of Sound and vibration* 30.2 (1973): 207-IN2. DOI: 10.1016/S0022-460X(73)80114-2.

[156] Leblond, A., and C. Hardy. "On the estimation of a 2× 2 complex stiffness matrix of symmetric Stockbridge-type dampers." *Proceedings of the 3rd International Symposium on Cable Dynamics, Trondheim, Norway*. Vol. 10. 1999.

[157] Luo, Xiaoyu, Liang Wang, and Yisheng Zhang. "Nonlinear numerical model with contact for Stockbridge vibration damper and experimental validation." *Journal of Vibration and Control* 22.5 (2016): 1217-1227. DOI: 10.1177/1077546314535647.

[158] Vaja, Nitish Kumar, Oumar Barry, and Brian DeJong. "Finite element modeling of Stockbridge damper and vibration analysis: Equivalent cable stiffness." *International Design Engineering Technical Conferences and Computers and Information in Engineering Conference*. Vol. 58226. American Society of Mechanical Engineers, 2017. DOI: 10.1115/DETC2017-68130.

[159] Vecchiarelli, J., I. G. Currie, and D. G. Havard. "Computational analysis of aeolian conductor vibration with a stockbridge-type damper." *Journal of Fluids and Structures* 14.4 (2000): 489-509. DOI: 10.1006/jfls.1999.0279.

[160] Foti, Francesco, et al. "A stochastic and continuous model of aeolian vibrations of conductors equipped with stockbridge dampers." *EURODYN 2020*. 2020. https://hdl.handle.net/2268/250033.

[161] Malla, Arun L., Sunit K. Gupta, and Oumar Barry. "Nonlinear Modeling and Analysis of Power Lines With Stockbridge Dampers Under Vortex-Induced Vibrations." *Dynamic Systems and Control Conference*. Vol. 84287. American Society of Mechanical Engineers, 2020. DOI: 10.1115/DSCC2020-3154.

[162] Di, Fangdian, et al. "Full-scale experimental study on vibration control of bridge suspenders using the Stockbridge damper." *Journal of Bridge Engineering* 25.8 (2020): 04020047. DOI: 10.1061/(ASCE)BE.1943-5592.0001591.

[163] Zondi, Zakhele, Modify Kaunda, and Tiyamike Ngonda. "Characteristics of the asymmetric Stockbridge damper." (2021). DOI: 10.1051/matecconf/202134700005.

[164] https://www.electricaldesks.com/2023/04/vibration-and-vibration-dampers-in-transmission-line.html.

# Acknowledgement

Thanks to the advice given by the defense committee, this doctoral thesis has become more substantial and well-rounded.

Heartfelt appreciation is extended to Professor Changhong Hu, the supervisor of this research, for his unwavering encouragement and support throughout the course of this study. His invaluable guidance in shaping the doctoral research, providing critical feedback on publications, organizing the thesis defense committee, and assisting in the acclimation to life in Fukuoka has been instrumental in the progression and completion of this work.

Special appreciation is also expressed to the Associate Professor Hongzhong Zhu, his numerous pieces of advice regarding experimental manipulation, revising publications, and improving English writing have been invaluable. I also express my special appreciation to the staffs of Marine Environment and Energy Engineering laboratory, especially Mr. Joshiro Noda, his some advice regarding experimental manipulation much-valued help me. I would like to express my appreciation to many lab mates, for their collaborative efforts and assistance during the research.

Lastly, deep gratitude is extended to my family and friends for their continuous support throughout the years in Japan. The encouragement and understanding from loved ones have been a constant source of strength. This thesis is dedicated to parents, siblings, and all the individuals who provided encouragement and support throughout the overseas career.